



EVALUATION AND VERIFICATION OF FIVE DIFFERENT IMAGE RECONSTRUCTION ALGORITHMS FOR ELECTRICAL RESISTANCE TOMOGRAPHY APPLICATIONS

By

CHARLIE NINDJOU DEBA

Supervisor: Dr. Reinhardt Kotzé

Co-supervisor: Mr. Andrew Sutherland

**A dissertation submitted in fulfilment of the requirements for the
MTech Degree in Electrical Engineering to the Faculty of Engineering at the**

CAPE PENINSULA UNIVERSITY OF TECHNOLOGY

Cape Town

October 2016

DECLARATION

I declare that this research dissertation is my own unaided work. It is being submitted for the MTech Degree at Cape Peninsula University of Technology, Cape Town. It has not been submitted before for any degree or examination in any other University.

(Signature)

Signed in Cape Town this _____ day of _____ 2017

EVALUATION AND VERIFICATION OF FIVE DIFFERENT IMAGE RECONSTRUCTION ALGORITHMS FOR ELECTRICAL RESISTANCE TOMOGRAPHY APPLICATIONS

Charlie Nindjou Deba

ABSTRACT

Tomography is the ability to internally visualise an opaque medium or a body, using different imaging techniques. Electrical Resistance Tomography (ERT) technique is a method commonly used in process tomography. It uses a non-intrusive resistance measurement between a set of electrodes attached on the circumference of a fixed cross-section with a given conductivity and permittivity distribution. ERT appears to be simple, low cost, safe and non-invasive. Despite the advantages of ERT, the reconstruction of the internal conductivity of the pipe still face a crucial challenges such as noise, a relatively low spatial resolution, as well as ill-posedness of the inverse problem when doing the image reconstruction using reconstruction algorithms. Although previous work showed the potential of various algorithms for the reconstruction of ERT tomograms, no full characterisation and comparison of different algorithms could be found for real flow situations.

The ERT system was tested in the identification of different objects and fluid beds in a real time situation. The data collected from the measurements were then used for the image reconstruction using an algorithm developed by Time Long (One-step algorithm) and four EIDORS-based algorithms namely: Gauss-Newton algorithm with Laplace Prior (LP) and Gaussian prior (Automatic Hyper Parameter Selection (AHSP)), the Total Variation (TV) algorithm and the Conjugate Gradient (CG) algorithm. The performance of each algorithm was tested in different scenarios. The results obtained were then compared based on the quality and the accuracy of the images as well as the computational time of each algorithm. Firstly, reconstructed images were obtained using objects placed inside the ERT pipe test. Secondly, the algorithm performances were put to test in a level bed setup experiment and finally, the algorithm reconstructions were applied to the real flow situation, where different flow rates were applied. The results obtained were then analysed and compared.

The TV algorithm produced better reconstructed images with respect to more defined shape of objects and sharper reconstructed images with an average percentage difference error of 19.8% and an average quality score and computational time of 2.7 and 12.22s respectively. With respect to the size of the area of low conductivity, the LP algorithm was the best EIDORS based algorithm with an average percentage error of 18.5%. The CG algorithm also yielded good reconstructed images with an average percentage error of 21.0%. Both algorithms produced an average quality score of 2.6 each with the fastest computational time of 6.45s and 7.24s. In terms of accuracy and the quality of the reconstructed images, the AHPS algorithm was the least performing algorithm with an average percentage error of 35.7%, an average image quality score of 1.8 out of 3 and an average computational time of 70.13s. Although the One-step was not the fastest reconstruction algorithm, it was the overall best performer in terms of accuracy and image quality with an average value of 13.5% and 2.7 respectively.

For industrial applications where characterisation of fluid flow inside the pipes is of most importance in order to prevent pipe blockages, the best algorithms selected could be usefully. For easy performance and comparative studies, a software (GUI) was developed for the selected EIDORS reconstruction algorithms. More tests could be done in real fluid suspensions like sand and oil in order to further investigate industrial applicability.

DEDICATION

To my Lord and Saviour Jesus Christ, *“Those who live in the shelter of the Most High will find rest in the shadow of the Almighty”* Psalms 91:1.

To my father, Francois Deba, who has always believed in me and has always supported me.

To my mother, Leontine Kangmogne Deba, my rock and my source of comfort in time of trouble.

To my step-mother, Delphine Kiela Deba, for her moral support all these years.

To my husband, Celestin Tsafack Dongmo for his love and support.

To my daughters: Eva Francine and Melissa for their unconditional love and the joy they bring into my life.

To my eldest sisters and my youngest siblings for being able to make me smile and laugh at times I needed it the most.

ACKNOWLEDGEMENTS

I wish to express thanks to:

- **My supervisors: Dr. Reinhardt Kotzé and Mr. Andrew Sutherland for their guidance through the entire research with much encouragement, wisdom and enthusiasm;**
- **The FPRC laboratory manager, Richard du Toit for his assistance with all the laboratory equipment and setup needed for this research;**
- **The Flow Process Research Centre (FPRC) at the Cape Peninsula University of Technology (CPUT) where I was given the opportunity to conduct the research;**
- **My parents for their continuous support during all these years. Their love and belief in me helped me not to give up during the difficult moments.**
- **John Shamu for his technical assistance every time I needed it.**
- **My colleagues and everybody who somehow contributed to this work.**

TABLE OF CONTENTS

		Page
Chapter 1	INTRODUCTION	1
1.1	Research Problem.....	2
1.2	Research Question.....	3
1.3	Objectives	3
1.4	Delineation	3
1.5	Significance of the Research.....	4
1.6	Organisation of the Dissertation	4
Chapter 2	LITERATURE REVIEW AND THEORY.....	6
2.1	Introduction.....	6
2.2	Overview of Imaging Techniques	6
2.3	ERT System and Data Collection Strategies.....	9
2.3.1	ERT sensors.....	9
2.3.2	ERT data acquisition system (DAQ).....	10
2.3.3	ERT data collection strategies	11
2.4	ERT Image Reconstruction.....	15
2.4.1	Forward modelling	15
2.4.2	Solving the inverse problem.....	18
2.4.3	Computation of the Jacobian matrix.....	19
2.5	Applications of ERT	20
2.5.1	Applications of ERT for industrial purpose.....	20
2.5.2	Applications of ERT for flow regime identification	22
2.6	Published Work Relevant to the Current Research.....	24
2.7	Summary.....	25
Chapter 3	RESEARCH EQUIPMENT AND METHODOLOGY.....	26
3.1	Equipment and Instrumentation	26
3.1.1	Experimental flow loop	26
3.1.2	Off-line static pipe setup	27
3.1.3	The Eagle Data Acquisition System (DAQ)	28
3.2	ERT Calibration Procedure.....	32

3.3	Experimental Procedures and Investigation	34
3.3.1	Material tested	34
3.3.2	The static experimental procedure	35
3.4	EIDORS Software.....	38
3.4.1	Solving the forward problem	41
3.4.2	Solving the inverse problem using EIDORS	44
3.4.3	Step-wise approached into solving the forward problem using EIDORS.....	47
3.4.4	Step-wise approach into solving the inverse problem using EIDORS	49
3.5	Image Reconstruction Algorithms used in this work.....	52
3.5.1	Overview of some selected reconstruction algorithms	52
3.5.2	Algorithm Characteristics	53
3.6	Algorithm Performance Criteria	55
3.6.1	Running time	55
3.6.2	Image quality and distinguishability.....	55
3.6.3	Accuracy	57
3.7	Development of a User-friendly GUI for ERT Post-data Analysis.....	58
3.8	Summary.....	61
Chapter 4	RESULTS AND DISCUSSION	63
4.1	Shape Test Experiment.....	64
4.1.1	Image reconstruction of Configuration A.....	64
4.1.2	Image reconstruction of Configuration B.....	66
4.1.3	Image reconstruction of Configuration C.....	67
4.1.4	Image reconstruction of Configuration D	69
4.1.5	Image reconstruction of Configuration E	70
4.1.6	Image reconstruction of Configuration F	72
4.1.7	Summary of experimental shape results	73
4.2	Level Bed Analysis.....	77
4.2.1	Image Reconstruction of Configuration L1	78
4.2.2	Image Reconstruction of Configuration L2	79
4.2.3	Image Reconstruction of Configuration L3	81
4.2.4	Summary of experimental level bed results	82
4.3	Flow Loop Test Analysis.....	85

4.3.1	Image Reconstruction of flow loop experiment A (0.68l/s).....	86
4.3.2	Image Reconstruction of the flow loop experiment B (1.3 l/s).....	87
4.3.3	Image Reconstruction of the flow loop experiment C (2.82l/s)	89
4.3.4	Image Reconstruction of the flow loop experiment D (4.5l/s)	90
4.3.5	Summary of experimental flow loop results.....	92
4.4	Final Summary	94
Chapter 5	SUMMARY, CONCLUSIONS, CONTRIBUTIONS, LIMITATIONS AND RECOMMENDATIONS.....	97
5.1	Summary.....	97
5.2	Conclusion	99
5.3	Contributions	100
5.4	Limitations	101
5.5	Recommendations.....	102

LIST OF FIGURES

Body

Figure 2.1	An overview of an ERT system.....	9
Figure 2.2	An arrangement of a typical 16 - electrode sensor ring (Dong, Xu, Hua & Wang, 2003).	10
Figure 2.3	Adjacent measurement strategy (Dickin and wang, 1996).	12
Figure 2.4	Opposite measurement strategy (Dickin and Wang, 1996).	13
Figure 2.5	Conducting boundary measurement strategy (Dickin <i>et al.</i> , 1996).	14
Figure 2.6	Diagonal measurement strategy (Dickin and Wang, 1996).	15
Figure 2.7	Electrodes attached to the boundary of a volume in space (Grootveld, Segal & Scarlett, 1998).	16
Figure 2.8	Conductivity maps for gas-liquid dispersion from a central sparger located at the bottom of the mixer for Rushton turbine (at 100 rpm) showing the effect of sparge rate (Williams et al., 1998).	21
Figure 2.9	Illustration of particle distributions profile in a pipe for different slurry flow regime (Crowe, 2006).	23
Figure 2.10	Comparison between ERT and MRI concentration profiles (a) photograph of sliding bed of sand particles in CMC taken during concentration data acquisition, (b) concentration map obtained with MRI, (c) real time concentration map obtained using ERT and (d) concentration map using ERT data and post-processing software (Stanley and Bolton, 2008).	23
Figure 3.1	Experimental setup at the FPRC.	27
Figure 3.2	Static pipe setup fitted with two electrode rings	28
Figure 3.3	The Eagle DAQ (left), and the internal view of the DAQ system (right).	28
Figure 3.4	Picture of a tomogram showing the measurement using the adjacent measurement sequence with no object in the tank.	29
Figure 3.5	Basic current-pulse ERT systems for single ring of 16 electrodes (Wilkinson <i>et al.</i> , 2006).	30
Figure 3.6	Single-layer multiplexer allows single plane measurements to be made on any one of eight rings (Randall <i>et al.</i> , 2002).	31

Figure 3.7	Data capture with no current applied and data capture with current applied.	33
Figure 3.8	Different materials used in the experiment. a) 3.3cm blue pipe, 2x2cm rectangle wood, b) white and black beads (3mm).	35
Figure 3.9	Shape test set up using a PVC pipe with 4.26cm in diameter: A) 2x2cm square wood position in the centre of the pipe, B) PVC pipe with 3.3cm diameter place at the centre of the pipe and C) Rod wood with 1.3cm diameter position in the centre of the pipe.	36
Figure 3.10	Shape test set up using a PVC pipe with 4.26cm in diameter: D) Rod wood with 1.3cm diameter place on the side close to the edge of the pipe, E) Two rod woods with 1.3cm and 0.8cm of diameter position both in the pipe close to the edge and F) Two rod woods with 1.3cm and 0.8cm of diameter position both in the pipe, the 1.3cm in the centre and the 0.8cm close to the edge.	36
Figure 3.11	Static tests set up using a PVC pipe with 4.26cm in diameter, with different level bed formed by beads submerged in saline water.	37
Figure 3.12	Experimental static test setup 2: Photographs of different level of bed formed by sand submerge into water.	37
Figure 3.13	Flow chart of the reconstruction procedure (Ahn S., 2011).	40
Figure 3.14	Geometry, loads and finite element meshes (Fish et al., 2007).	42
Figure 3.15	Structure of the EIDORS fwd_model objects (Adler et al., 2006).	44
Figure 3.16	Structure of the EIDORS inv_model object (Adler <i>et al.</i> , 2006).	46
Figure 3.17	Line of code used to solve the forward problem.	47
Figure 3.18	Line of code used to solve the inverse problem.	49
Figure 3.19	A- Initial configuration (3.3 cm PVC pipe), B to D - reconstructed images using Laplace prior with hyperparameter value of: 1e-4, 1e-3 and 30e-3.	51
Figure 3.20	On the left: the real shape and level bed used in the experiment, on the right: Image of a poor representation of the real shape and the level bed.	56
Figure 3.21	On the left: the real shape and level bed used in the experiment, on the right: Image of an average representation of the real shape and level bed.	56
Figure 3.22	On the left: the real shape and level bed used in the experiment, on the right: Image of a good representation of the real shape and level bed.	56
Figure 3.23	Resistivity map of the solid object based on the colour bar scale.	57
Figure 3.24	An example of the calculation of the area of low conductivity.	58

Figure 3.25	Image of the GUI created using MATLAB software.....	59
Figure 3.26	Example of image comparison using the GUI.	60
Figure 3.27	Results of reconstructed images from the GUI.	61
Figure 4.1	Configuration of different objects used in the shape experiment.	64
Figure 4.2	Reconstructed image comparison for measurement configuration A - 3.3cm PVC pipe.	64
Figure 4.3	Reconstructed image comparison for measurement configuration B - 2x2cm square wood piece.....	66
Figure 4.4	Reconstructed image comparison for measurement configuration C – 1.3 cm rod wood place at the centre of the experimental pipe.	67
Figure 4.5	Reconstructed image comparison for measurement configuration D – 1.3 cm rod wood place on the side of the experimental pipe.....	69
Figure 4.6	Reconstructed image comparison for measurement configuration E – 1.3cm and 0.9cm rod woods placed close to the side of the experimental pipe.	70
Figure 4.7	Plot of the reconstructed image of the inverse problem for the 1.3cm and 0.9cm rod woods placed at the centre and closed to the edge of the pipe.	72
Figure 4.8	Summary of image reconstruction comparison for measurement configuration A-F	74
Figure 4.9	Configuration of different level bed heights used in the static level bed experiment	77
Figure 4.10	Image reconstruction comparison for measurement configuration L1 (static level bed test).....	78
Figure 4.11	Image reconstruction comparison for measurement configuration L2 (static level bed test).....	80
Figure 4.12	Image reconstruction comparison for measurement configuration L3 (static level bed test).	81
Figure 4.13	Summary of image reconstruction comparison for measurement configurations L1 – L3.	83
Figure 4.14	Configuration of different flow rates and level bed heights used in the flow loop experiment.....	85
Figure 4.15	Image reconstruction comparisons for flow loop experiment A (0.86l/s).	86
Figure 4.16	Image reconstruction comparisons for flow loop experiment B (1.3 l/s).	87

Figure 4.17	Image reconstruction comparisons for flow loop experiment C (2.82l/s).	89
Figure 4.18	Image reconstruction comparisons for flow loop experiment C (4.5l/s).	90
Figure 4.19	Summary of image reconstruction comparison for flow loop experiments A-D ..	92

Appendices

Figure A.1	<i>The initial start screen</i>	109
Figure A.2	<i>The mesh and precomputed file loaded correctly</i>	110
Figure A.3:	<i>Downloading measurement sequence</i>	110
Figure A.4	<i>An expanded error message box</i>	111
Figure A.5	<i>The 'Start Capture' button</i>	111
Figure A.6:	<i>Data capture with no current applied</i>	Figure A.7: <i>Data capture with current applied</i>
	
Figure A.8:	<i>The 'Calibrate' button</i>	112
Figure A.9:	<i>The colour map drop down menu</i>	113
Figure A.10:	<i>The tomography program reconstructing conductivity images</i>	113
Figure A.11:	<i>The record button</i>	114
Figure A.12:	<i>The 'Start Wizard' button</i>	114

LIST OF TABLES

Body

Table 3.1	Detail specifications of the 'c2d0c' model available from mk_common_model ..47
Table 3.2	Personal Computation specifications used for the image reconstructions.....55
Table 4.1	Algorithm performance comparisons for measurement configuration A - 3.3 PVC pipe65
Table 4.2	Algorithm performance comparison for measurement configuration B - 2x2cm square wood piece.....67
Table 4.3	Algorithm performance comparison for measurement configuration C – 1.3cm rod wood placed at the centre of the experimental pipe.....68
Table 4.4	Algorithm performance comparison for measurement configuration D – 1.3cm rod wood placed on the side of the experimental pipe.....70
Table 4.5	Algorithm performance comparison for measurement configuration E – 1.3cm rod wood placed at the centre and 0.9cm placed close to the edge of the experimental pipe71
Table 4.6	Algorithm performance comparison for measurement configuration F – 1.3cm and 0.9cm rod wood placed close to the edges of the experimental pipe73
Table 4.7	Summary of Hyperparameter values for the shape test experiments (A – F).....75
Table 4.8	Average percentage difference error for each algorithm for the shape test experiments (A – F)75
Table 4.9	Average computational time (in seconds) of each algorithm for the shape test experiments (A – F)76
Table 4.10	Image Quality of each configuration (A – F)76
Table 4.11	Algorithm performance comparison for measurement configuration L1 – level bed 1.5 cm.....79
Table 4.12	Algorithm performance comparison for measurement configuration L1 – level bed 2.2 cm.....80
Table 4.13	Algorithm performance comparison for measurement configuration L1 – level bed 3.4cm.....82
Table 4.14	Average accuracy for each algorithm for the level bed experiments (L1 – L3).....83

Table 4.15	Average computational time (in second) of each algorithm for the level bed experiments (L1 – L3).....	84
Table 4.16	Average of the image quality (IQ) scores of each algorithm for the level bed (L1 – L3).....	84
Table 4.17	Algorithm performance comparison for flow loop experiment A (0.86l/s)	87
Table 4.18	Algorithm performance comparison for flow loop experiment B (1.3l/s)	88
Table 4.19	Algorithm performance comparison for flow loop experiment C (2.82l/s)	90
Table 4.20	Algorithm performance comparison for flow loop experiment D (4.5l/s)	91
Table 4.21	Average accuracy for each algorithm for the flow loop experiments	93
Table 4.22	Average computational time (in second) of each algorithm for the flow loop experiments	93
Table 4.23	Average of the image quality scores of each algorithm for the flow loop experiments	94
Table 4.24	Average values of the percentage difference error (PE) of each experiment.....	94
Table 4.25	Average values of the computational time (CT) for each experiment	95
Table 4.26	Average values of the image quality (IQ) for each experiment.....	95

NOMENCLATURE

Constants

B	Number of simplices
C	Boundary condition
C	n-dimensional vector
C	Current patterns
C_n	Number of ideally conducting electrode
D	Model dimension
E	Electrodes vector
F	Voltage vector
F'	Jacobian matrix
i	Injection current
I_{in}	Input current
I_{out}	Output current
i_k	Sum of injected current
J	Current density
M	Number of independent measurement
n	Outward-pointing normal vector
n	Discrete points
N	Number of electrode
N	Number of unknown conductivities
S	Surface of the electrode
U	Electrical potential
U	n-dimensional vector
v	Voltage vector
V	Volume in space
V	Electrical potential (volts)
V	Number of vertices
V_0	Measured voltage vector
X	Vector of image measurement
Y	Symmetric positive (Siemens)

Greek letters

σ	Electrical conductivity
Φ	object function
Φ''	Hessian matrix
ξ	Stable solution
∂	Differentiator
Δ	Integrator
$\Delta\sigma^k$	Modified Newton-Raphson method

TERMS AND CONCEPTS

2D and 3D	2- dimension and 3-dimension
AHPS	Automatic Hyperparameter Selection
CG	Conjugate Gradient
CT	Computer Tomography
DAQ	Data Acquisition System
ECT	Electrical Capacitance Tomography
EIDORS	Electrical Impedance and Diffuse Optical Reconstruction Software
EIT	Electrical Impedance Tomography
EMT	Electrical Magnetic Tomography
ERT	Electrical Resistance Tomography
FEM	Finite Element Method
FPRC	Flow Process Research Centre
GIA	The Generalised Iterative Algorithm
IP	Induced Polarization
LP	Laplace Prior
LBP	Linear Back-Projection
MRI	Magnetic Resonance Imaging
PE	Percentage Error
PC	Personal Computer
PET	Position Emission Tomography
PVC	Polyvinyl chloride
UCT	University of Cape Town
VSD	Variable Speed Drive
TV	Total Variation

Chapter 1 INTRODUCTION

The need to understand the behaviour of internal flows in process equipment has extensively increased over the past years. Process tomography is a technique used in industry for imaging fluid beds and particles distribution and to determine the concentration distribution of mixtures within pipe lines. Tomographic imaging enables study of the internal structures of flows without the need to invade the flow (York, 2004).

In the medical field, imaging techniques such as X-ray or Computer Tomography (CT) scanners have been used extensively for medical diagnostics. In the process industry, imaging techniques such as Electrical Capacitance Tomography (ECT), Electrical Resistance Tomography (ERT) and Electromagnetic Tomography (EMT) have been derived from the Electrical Impedance Tomography (EIT) technique applied in the medical field.

An appropriate imaging technique must be used in order to visualise the internal distribution of particles flowing inside the pipe. Furthermore, the determination of the slurry concentration profile in the pipeline transport is of great importance in order to calculate the friction losses and the pressure drop. These two characteristics are needed to proportion pumps and pipes and to control the operating conditions (Queiroz, 2012; Adetunji, 2011; Giguère, Fradette, Mignon & Tangy, 2008a).

One technique that can be used to visualise settling slurry flow is called Electrical Resistance Tomography. ERT aims at reconstructing the electrical conductivity distribution within a pipe (Dyakowski, Jeanmeure & Jaworski, 2000; Tamburrino and Rubinacci, 2002). ERT uses an array of sensing elements (called electrodes) placed around the circumference of a pipe or vessel. Different current patterns are applied to the electrodes (one pair at the time) and the resulting voltage changes are then measured on the other electrodes. The current-voltage relationship allows the reconstruction of conductivity (in a form of a tomogram) within the measured region using the electrical measurements made at the surface (Zhang, Wang, Xu & Wang, 2011). The advantages of ERT are its relatively low cost and simple electrodes design (Granot & Rubinsky, 2007).

The most accurate model for ERT is referred to as a complete electrode model, which consists of the Poisson equation, obtained by the Maxwell relations and simplifications applied to the

electrical conductivity and electrical potential (Karhunen, Seppänen, Lehtikoinen, Monteiro & Kaipio, 2010; Giguère et al., 2008b; Borges, De Oliveira, Velez, Tavares, Linhares & Peyton, 1999; Cheng, 2001). Tomography images are determined by two steps: the solution of the forward problem which is the problem solved by finding the electrical potential between the electrode pairs for a given current injection and the inverse problem which requires the reconstruction of the internal conductivity distribution and the contact impedances given the boundary voltage measurements (Giguère *et al.*, 2008b & Karhunen *et al.*, 2010).

Cross-correlation techniques or singular value decomposition are statical methods that could be used to analysed tomographic data. These methods are mostly based on two or three dimensions. In 2D tomography, the measurements are obtained only for one or some cross sections. Any inhomogeneity or object can exist outside the investigation zone and can affect the measurement values, resulting in that object not been reconstructed. In the 3D approach, the measurements are obtained between electrodes from different layers, therefore an inhomogeneity will affect the measurement values and will be distinguished in the final image. Image reconstructions are obtained based on a series of measurements obtained from sensors that are placed on a cross-section plane. The data obtained from the measurement can then be applied to various image reconstruction techniques in order to obtain the distribution of dielectric permittivity on these cross-section planes (Wajman *et al.* 2006).

However, there is still a need for information regarding the effectiveness of various image reconstruction techniques/algorithms because ERT has challenges such as noise, a relatively low spatial resolution, as well as ill-posedness of the inverse problem (Zhang et al. 2011 & Barber, 2005). This research work aims at investigating and comparing five different reconstruction algorithms using ERT system when applied to the detection of objects and real flow situation.

1.1 Research Problem

The main problem is that there is uncertainty about the performance (e.g. accuracy and speed) of available ERT image reconstruction algorithms with regards to measurements in different experimental conditions and applications.

1.2 Research Question

Which of the five reconstruction algorithms evaluated has the best performance in terms of quantitative accuracy, images quality and computational time?

1.3 Objectives

The objectives of this research were to:

- ❖ Evaluate five image reconstruction algorithms in three different experimental setups:
 - Static tests in pipe using different objects
 - Static tests in pipe using stationary bed simulated with water and plastic beads
 - Dynamic tests in a flow loop using water and plastic beads at different flow rates (flow regimes)

- ❖ Compare the performance of the algorithms based on the:
 - accuracy
 - computational time, and
 - quality of image/tomogram

1.4 Delineation

Only the ERT system developed by UCT (describe in Chapter 3, Section 3.1.1) was used during the work. No other hardware systems or variations will be considered.

One symmetrical electrode configuration (one ring of 16 electrodes) and pipe diameter (4.26 cm) will be used. Water and beads (3mm) was used for the level bed and the flow loop experiments. Only five image reconstruction algorithms (Gauss-Newton algorithm with Laplace prior, the Automatic Hyperparameter Selection algorithm, the Total Variation algorithm, the Conjugate Gradient algorithm and the One-step algorithm) were investigated and EIDORS

(Electrical Impedance and Diffuse Optical Reconstruction Software) functions were used to generate the images or tomograms. Only 2D reconstructions were considered.

1.5 Significance of the Research

Detailed information using various image reconstruction algorithms will enable more efficient and accurate flow process monitoring by selecting the appropriate algorithm with the highest performance for particular applications. The study and application of ERT reconstruction algorithms can help to find a new approach for more accurate image reconstruction techniques. That can be used to improve monitoring of flow properties for example.

Using an appropriate reconstruction algorithm in combination with the ERT hardware could be used for in depth investigation into the accuracy of theoretical models and simulation of complex multiphase and coarse particle flows. In addition, detailed and accurate measurements may lead to new and improved complex flow predictions using for example Computational Fluid Dynamics.

1.6 Organisation of the Dissertation

The overall approach to this research is discussed below.

- **Literature review (Chapter 2)**

In order to better understand the concept behind the ERT system and image reconstruction, the literature review is subdivided into six parts namely: overview of imaging techniques, the ERT system, ERT image reconstruction in terms of description of operation, the different application and finally published work relevant to this research.

- **Research methodology (Chapter 3)**

The ERT system was used in order to collect data from three different experimental setups namely: static shape test, static level bed test and the flow loop test. One electrode ring fitted

with 16 electrodes was used for measurements during the experiments. A pipe section of one meter long was used for the static level bed and the static shape test, while the flow loop test was conducted on a rig with an electrode ring (with 16 electrodes) fitted on one section of the pipe. An overview of selected reconstruction algorithms as well as the algorithm comparison criteria is presented. The development of a user friendly GUI is also shown.

- **Results and discussion (Chapter 4)**

The results obtained from the three experimental setups are presented in Chapter 4. Measured data collected during the experiment were used to reconstruct images using five 2D reconstruction algorithms. The results obtained from each algorithm were compared based on three criteria: the accuracy of the reconstructed images, the quality of the reconstructed images and the computational time taken by each algorithm. The results of the comparison were presented in form of tables and graphs.

- **Summary, conclusions and recommendations (Chapter 5)**

Chapter 5 summarises this research as well as final conclusions drawn from the research work. Limitations of software algorithm and the ERT system are discussed and recommendations are made for future work.

Chapter 2 LITERATURE REVIEW AND THEORY

2.1 Introduction

This chapter presents background knowledge on ERT system and its applications, as well as an overview on imaging techniques that are being used. Section 2.2 of this chapter presents an overview of various imaging techniques available. Background knowledge of ERT is investigated in Section 2.3 which includes the basic structure of the ERT ring sensor, the ERT data acquisition as well as the ERT measurement techniques. The description of the forward and inverse problem of ERT image reconstruction is presented in Section 2.4. The importance of ERT in the flow process applications and the industrial process field is emphasised in Section 2.5. The discussions of some publish work relevant to this research is presented in Section 2.6 and final the summary of this chapter is given in Section 2.7.

2.2 Overview of Imaging Techniques

Tomography is a technique used to visualise an opaque medium or a body internally, using different imaging techniques. In the medical field, the X-ray is one of the first imaging techniques used to reproduce the pictures of an internal structure. The X-ray uses radiation energy that has the ability to infiltrate the body cells in order to provide important information concerning the health of an individual. Due to the poor contrast resolution of the X-ray, Computer Tomography (CT) scanners were then introduced with the ability to produce more contrast images (Blink, 2004 & Barber, 2005).

In order to generate a 3-dimensional image of body structures, CT scans use large series of 2-dimensional X-rays. This combination gives a fair visualisation of the anatomy of tissues and their metabolic activity (Lionheart, Polydorides & Borsic, 2005; Holder, 2008).

Another imaging technique that is applied in the medical field is called the positron emission tomography (PET). PET is a nuclear medicine imaging technique which is able to produce a 3-dimensional image or a map of functional processes in the body, which is based on the

detection of positrons also called protons. The PET scan is based on the detection of a radioactive substance, also called a tracer, which is chemically injected into the body and then labeled using a positron emitter. Computer analysis is then used to reconstruct 3-dimension images of the tracer's concentration inside the body. (Cooper, Harnan, Meng, Ward, Fitzgerald, Papaioannou & Lorenz, 2011; Wells, de Kemp & Beanlands, 2009).

Magnetic Resonance Imaging (MRI) is one of the most widely used techniques in medical diagnostics. Compared to CT, MRI provides a better contrast between the different soft tissues of the body and no ionizing radiation is used. MRI scan uses a strong magnetic field and radiofrequency to form the images of the body by aligning nuclear magnetisation of atoms in water in the body, therefore, providing complete images of the body on every plane (Holder, 2008).

The identification of electrical chargeability of subsurface materials is done through the geophysical imaging technique and it is also called induced polarization (IP). IP consist of inducing an electric current into the surface through two electrodes and subsequently detecting the voltage through two other electrodes (Cooper *et al.*, 2011; Wells *et al.*, 2009).

Electrical Impedance Tomography (EIT) is a non-invasive medical imaging technique in which measurements obtained from surface electrode connected to the body are used to image the conductivity or permittivity of the body (Brown, 2009 & Cheney *et al.* 1999). The EIT family include systems such as Electrical Capacitance Tomography (ECT) and Electrical Resistance Tomography (ERT), which are methods commonly used in process tomography (Hartov, Soni & Halter, 2005). Over the past years, it has been intensely investigated and used in industrial applications. ERT and ECT respectively use a non-intrusive resistance and capacitance measurements between a set of electrodes attached to the circumference of a fixed cross-section with a given conductivity and permittivity distribution (Alme & Mylvaganam, 2006).

ERT, just as ECT, has been used in many applications such as the measurement of two-phase flow regimes in the pipelines or the analysis of dynamic progressions of fluidised beds. ERT, compared to other imaging techniques mentioned previously, appears to be simpler and cheaper.

Despite the advantages such as low-cost, rapid response and the non-invasion aspect of the ERT technique, the reconstruction of the internal conductivity of the pipe still faces a crucial challenge, which is the undetermined problem of the ill-posedness of the inverse problem when dealing with the reconstruction image (Queiroz, 2012 & Wang, Tang & Cao, 2007). The problem of recovering unknown conductivity using boundary measurement of current and potential is what constitutes the non-linear and the ill-posed nature of the inverse problem. A mathematical problem is well posed if: (1) for all admissible data, a solution exists, (2) for all admissible data, the solution is unique, and (3) the solution depends continuously on the data. The third criterion is what causes difficulties when solving the inverse problem (Lionheart *et al.*, 2005).

There have been some investigations done on the identification of flow regimes (which is discussed in more details in section 2.5.2) as well as comparison of different algorithms using different measurement techniques of ERT. However, there have not been many investigations on the use of ERT system in the identification of fluid bed in real time, or any identification or comparison of precise algorithms for real time applications (Scott and McCann, 2005; Mann, Dickin, Wang, Dyakowski, Williams, Edwards, Forrest & Holden, 1997; Sharifi & Young, 2013). Therefore, because of its numerous advantages, ERT will be used throughout this research, with the goal of identifying five algorithms which will provide reconstructed images of internal conductivity measurements with as much precision as possible.

As much as it is important to have an overview of different tomography and imaging techniques, the description of the ERT system also contribute to a better understanding of the use of ERT and its operation.

2.3 ERT System and Data Collection Strategies

As shown in Figure 2.1, the ERT system is typically composed of three main parts, namely: the sensors, the data acquisition system and the control PC with data processing software and reconstructing unit (Soulsby, Yazaki, & Evans, 2004). The following sub-sections will discuss in more detail each of these parts, starting with the ERT sensors.

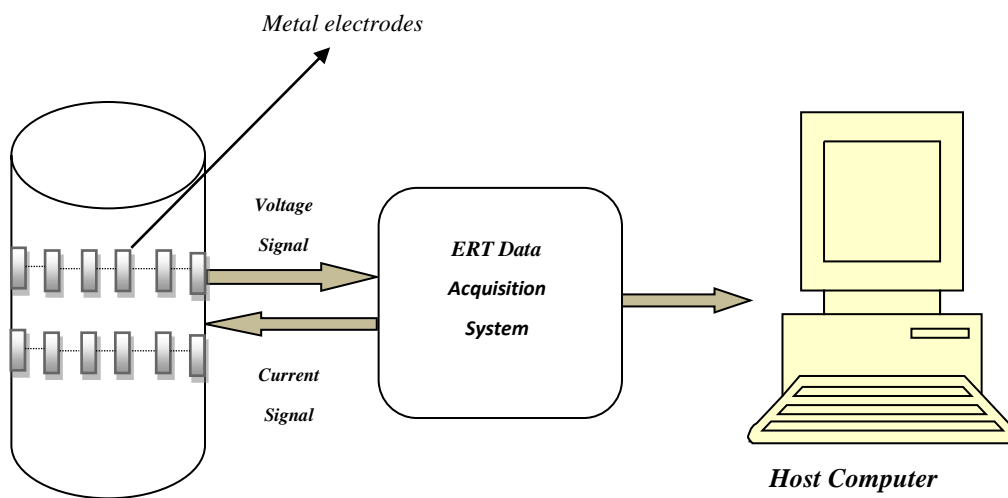


Figure 2.1 An overview of an ERT system.

2.3.1 ERT sensors

A set of rectangular or round electrodes are mounted on the inside surface of an insulating pipe forming what is called an annular sensing array (Tapp, Peyton, Kemsley & Wilson, 2003). The sensing electrodes are manufactured using metals such as titanium, platinum, gold brass, silver or stainless steel. They usually have characteristics such as low resistance, high conductivity and low installation costs. The ERT sensor system usually uses a 16 - electrode array which is symmetrically arranged around the measuring pipe circumference (Hartov *et al.*, 2005 & York, 2004). Each electrode is in contact with the inner conductive solution. Reliable measurements are obtained when the electrolyte is less conductive than the sensors (Dickin & Wang, 1996; Jia, Dong, Xu, Tan & Xue, 2005; Ying, Jinchuang, Shi & Xinjie, 2001).

The injection of current from one electrode to the other produces an electrical field within the measured medium. The voltages measured from the injected current are then used to reconstruct the conductivity distribution of the internal configuration of the pipe section using a suitable algorithm. An arrangement of sensitive electrode array is shown in Figure 2.2.

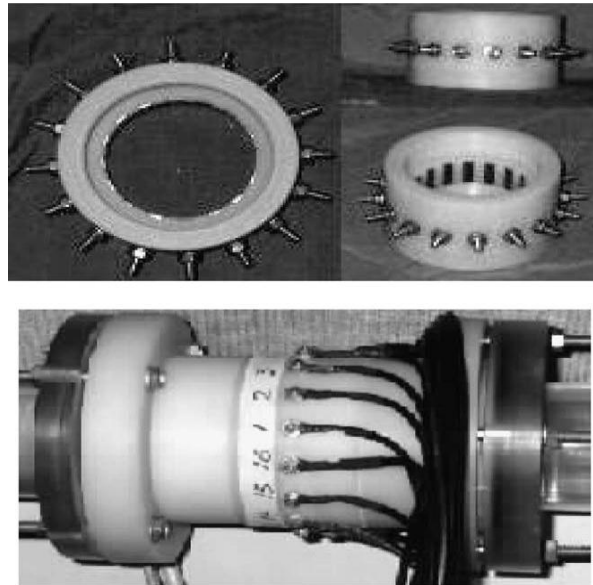


Figure 2.2 An arrangement of a typical 16 - electrode sensor ring (Dong, Xu, Hua & Wang, 2003).

Depending on the measurement technique (such as adjacent or opposite) used, each electrode pair is excited one at the time by an injected current. Each injected current produces an electrical field of all the measured voltages values between any other two electrodes. The data measured from the injected current is then used to reconstruct the tomogram detailing the conductivity distribution of the pipe's cross section.

2.3.2 ERT data acquisition system (DAQ)

The ERT data acquisition system is an element that injects current and then collects the quantitative information (the resultant voltages measured) which describes the internal conductivity distribution of a vessel (Sharifi *et al.*, 2013).

The ERT DAQ system is connected to a process vessel and a computer (PC). It communicates in a bi-directional way with the process vessel by implementing a cross-correlation current

injection strategy (York, 2004). The cross-correlation current injection strategy consists of measuring the voltage given the current simulation sequence, using the measurement sequence table which is downloaded into the computer. The PC communicates with the data acquisition system by extracting the stored measured voltage data in order to display reconstructed images using the reconstruction algorithm code stored in the PC (Adetunji, 2011; Mann *et al.*, 1997; Sharifi *et al.*, 2013; Pakzad, Ein-Mozaffari & Chan, 2008; Dong *et al.*, 2006). The different strategies used for the data acquisition will be discussed in the next section.

2.3.3 ERT data collection strategies

There is a variety of data collection strategies to choose from, which include adjacent strategy, opposite strategy, diagonal strategy and conducting boundary strategy (Mann *et al.*, 1997; Sharifi *et al.*, 2013; Pakzad *et al.*, 2008 & Dong *et al.*, 2006).

❖ *The adjacent electrode pair strategy*

The adjacent electrodes pair strategy shown in Figure 2.3, is the most used in the ERT data acquisition. In this method, electrical current is injected between adjacent electrodes. Thereafter, voltages are measured between pairs of neighbouring electrodes (refer to Figure 2.3) (Dickin and Wang, 1996; Sharifi *et al.*, 2013 & Jia *et al.*, 2005). The number of independent measurement is given by Equation 2.1:

$$M = N(N - 3)/2. \tag{2.1}$$

with M the number of independent measurements and N the number of electrodes.

The advantage of the adjacent method is the fact that the data collection is quicker and it requires minimal amount of hardware to be implemented. However, because of its non-uniform distribution and low current density at the centre of the vessel, the adjacent strategy is sensitive to error measurement and noise (Dickin and Wang, 1996; Jia *et al.*, 2005).

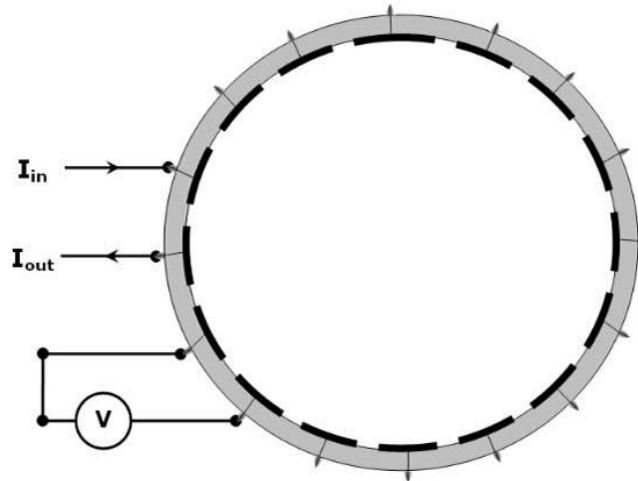


Figure 2.3 Adjacent measurement strategy (Dickin and wang, 1996).

❖ The opposite strategy

In the opposite strategy, current is applied between diametrically opposite electrodes (refer to Figure 2.4). The voltage is then measured between other adjacent electrodes pairs except the current injection electrodes. The next set of data is obtained by switching the current, in the clockwise direction, to the next pair of opposite electrodes (Graham, 2007 & Dickin & wang, 1996).

The opposite strategy has the advantage of providing even current distribution when compared to other methods and it gives better resolution at the centre than adjacent.

Its disadvantage lies in the fact that it provides fewer numbers of independent measurements for a specified number of electrodes (Oh and Sadleir, 2005).

Equation 2.2 provides the number of independent measurements M for this method.

$$M = \frac{N}{4} \left(\frac{3N}{2} - 1 \right). \quad (2.2)$$

For 16 electrodes, Equation 2.2 gives $M = 92$, a decrease of 23% in the number of voltage measurements compared with the adjacent strategy for the same number of electrodes (Dickin and Wang, 1996).

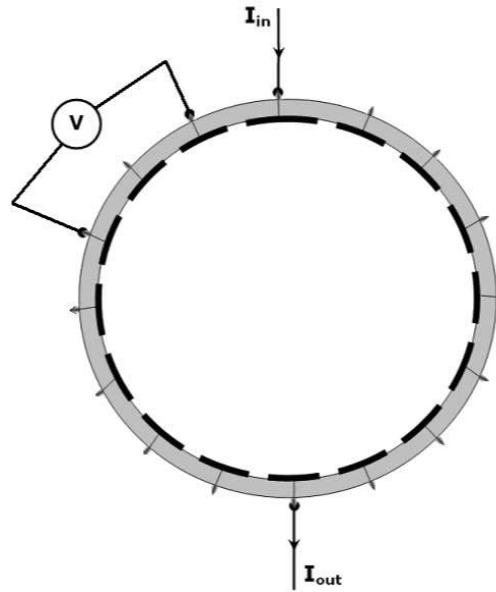


Figure 2.4 Opposite measurement strategy (Dickin and Wang, 1996).

❖ The conducting boundary strategy

The conduction boundary method was devised by Wang, Dickin & Mann, 1999 mainly for electrically conducting walled vessel. This method only uses two electrodes to measure voltages between the vessel and other electrodes when applying a current between the conducting vessel and the electrodes (Yunus, Rahim, Ayob, Jayasuman & Jumaah, 2014).

The advantage of the conduction boundary method is its low common-mode voltage compared to the adjacent strategy. The disadvantage of this method is the low voltage measurement amplitudes which decrease by a factor of seven compared to the adjacent strategy (Yunus, *et al.*, 2014). The number of measurements is given by equation:

$$M = \frac{N(N-1)}{2}. \quad (2.3)$$

For a 16 electrodes, an independent measurement of 120 can be achieved using Equation 2.3. The conductive boundary measurement strategy is shown in Figure 2.5.

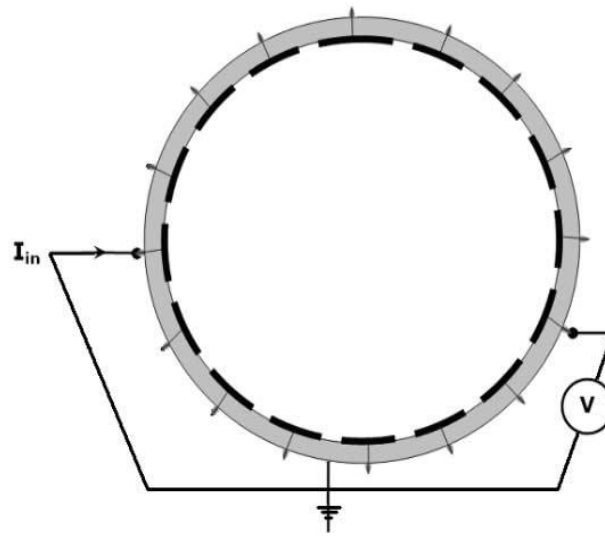


Figure 2.5 Conducting boundary measurement strategy (Dickin and Wang, 1996).

❖ The diagonal strategy

Also called the cross method, the diagonal strategy injects current between electrodes which are separated by large dimensions. Compared to the adjacent strategy, this method provides more uniform current distribution in the measurement region (Yunus, et al., 2014 & Dickin and Wang, 1996). For a 16-electrode configuration, the first electrode is fixed as the current reference and the second electrode is set as the reference voltage. Current is then injected into the third electrode up to the fifteenth electrode. From each current injection pairs, voltages (from all electrodes) are measured with respect to the second electrode except for the current electrodes as shown in the Figure 2.6. For a ring of 16 electrodes, a maximum of 182 data points can be achieved with only 104 independent measurements (Dickin and Wang, 1996).

The diagonal measurement strategy is shown in Figure 2.6.

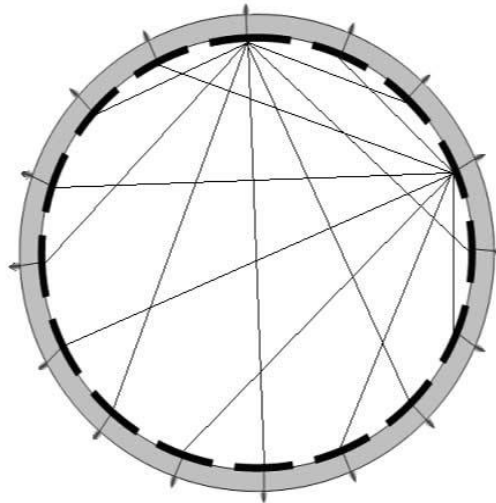


Figure 2.6 Diagonal measurement strategy (Dickin and Wang, 1996).

Compared to the adjacent method, the diagonal strategy does not provide high sensitivity in the periphery. However, the diagonal strategy is not so sensitive to measurement error and provides better image quality (Dickin and Wang, 1996).

2.4 ERT Image Reconstruction

The purpose of image reconstruction is to compute a tomogram showing the electrical conductivity of the material flowing within a vessel, based on voltages measured at the border of the sensors in response to the electrical current injected. The ERT problem consists of solving the forward and the inverse problem, which is a non-linear and ill-posed problem.

2.4.1 Forward modelling

Before the image reconstruction is done, the forward problem need to be solved. In order for the reconstruction to be accurate, the predictions of the measurement at the boundary from an inhomogeneous material need to be done.

The forward problem is the problem solved by finding the electrical potential between the electrode pairs for a given current injection (Giguère *et al.* 2008b & Lionheart *et al.*, 2005). Due to the complexity of the equation used in the forward problem, numerical methods are required given the fact that there is no analytical solution for an arbitrary conductivity distribution (Pineiro, Loh & Dickin, 1998). To model the forward problem, the finite-element method (FEM) is commonly used. This method discretises the region of interest into small elements with constant conductivity. The potential distribution is estimated using a polynomial basis to interpolate between identified nodal values (Pineiro *et al.* 1998; Vauhkonen Vauhkonen, Savolainen & Kaipio, 1999).

The FEM transforms the forward problem into one of solving a set of linear equations, which in the case of ERT provides an approximation of the potential differences for a given conductivity distribution (Pineiro *et al.* 1998; Giguère *et al.* 2008b).

Figure 2.7 shows a conductive medium with a volume V in space with a boundary C . The boundary C holds a finite number of ideally conducting electrodes $C_n(n = 1 \dots N)$.

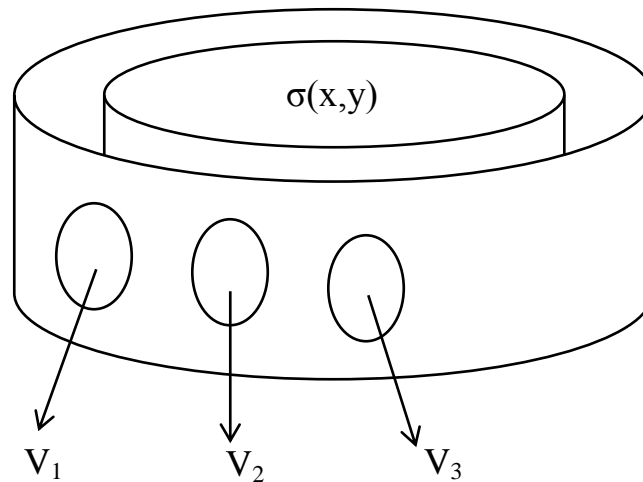


Figure 2.7 Electrodes attached to the boundary of a volume in space (Grootveld, Segal & Scarlett, 1998).

As shown in Figure 2.7, using the Maxwell's equation and Ohm's law, the governing equation is given in the form of:

$$\nabla \cdot (\sigma \nabla U) = 0 \quad (2.4)$$

where U is the electrical potential and σ is the electrical conductivity (Grootveld *et al.*, 1998).

Given the current injection and the current density, J is given as:

$$J = \begin{cases} \sigma \frac{\partial V}{\partial n} \mathbf{n}: & \text{at the current injecting electrodes.} \\ 0: & \text{Elsewhere,} \end{cases} \quad (2.5)$$

where n is the outward-pointing normal vector.

The injection currents i , are given by:

$$i = \int_S J \cdot \mathbf{n} \, dS \quad (2.6)$$

where S is the surface of the electrode. Therefore, the sum of injected currents, i_k is equal to zero.

Hence:

$$\sum_{k=1}^N i_k = 0. \quad (2.7)$$

The electrode potentials from the measured data consist of:

$$U(C_{j,k}) = u_{j,k} \left(j = 1 \dots N - 1, k = 1 \dots \frac{N}{2} \right) \quad (2.8)$$

Using the FEM, the equation $\nabla(\sigma \nabla U) = 0$. is discretised into a linear system: $Yv = c$.

Where v represents the voltage vector and c represent the boundary conditions (Grootveld *et al.*, 1998).

Since c and v change for every experiment while the matrix Y remains the same, the complete set of experiments is formed as:

$$YU = C \quad (2.9)$$

where U is an n -dimensional vector representing the potential (units in volt) at n discrete points, Y is a symmetric positive which delimits n by n conductance matrix (Siemens) and C is an n -dimensional vector containing the applied current at the previous n discrete point (Ampere) (Pinhero *et al.*, 1998).

2.4.2 Solving the inverse problem

The inverse problem is an ill-posed and nonlinear problem. It is, in other words, reconstruction of the conductivity distribution σ from the set of electrical measurements on the boundary (Queiroz, 2012; Pinheiro *et al.*, 1998 & Borcea, 2002). In order to obtain a stable solution to the ill-posed problem, regularisation techniques such as Tikhonov regularisation have to be implemented (Vauhkonen *et al.*, 1999 & Holder *et al.*, 2008). The idea behind the inverse problem is to continually solve the forward problem while updating the conductive distribution σ according to some criterion (Grootveld *et al.*, 1998).

Grootveld *et al.* (1998) used a criterion based on the minimisation of the norm of the difference between the calculated voltage vector F and the measured vector V_0 , where F is a subset of V which contains only the electrode potentials. The minimized object function is given by:

$$\emptyset = \frac{1}{2}(F - V_0)^T(F - V_0). \quad (2.10)$$

Equation (2.10) is then differentiated with respect to σ and set to zero in order to minimize the object function \emptyset , leading to:

$$\frac{\partial \emptyset}{\partial \sigma} = \emptyset' = [F']^T[F - V_0] = 0. \quad (2.11)$$

where F' is called the Jacobian matrix of which the $(g, h)^{\text{th}}$ element is defined by:

$$[F']_{gh} = \frac{\partial F_g}{\partial \sigma_h} \quad (2.12)$$

$$\emptyset' \approx \emptyset'(\sigma^k) + \emptyset''(\sigma^k)\Delta\sigma^k. \quad (2.13)$$

The \emptyset'' term is the Hessian matrix, which by Equation (2.11) equals:

$$\emptyset'' = [F']^T F' + F''[F - V_0] \otimes [F']^T F'. \quad (2.14)$$

Hence:

$$\emptyset'' \approx [F']^T F'. \quad (2.15)$$

When substituting Equation (2.13) and (2.15) into Equation (2.11) the following expression is obtained

$$[[F'(\sigma^k)]^T F'(\sigma^k)]\Delta\sigma^k = -[F'(\sigma^k)]^T [F(\sigma^k) - V_0], \quad (2.16)$$

$$\text{with } \Delta\sigma^k = (\sigma^{k+1} - \sigma^k). \quad (2.17)$$

This formulation is called the modified Newton-Raphson method, which also assures second-order.

2.4.3 Computation of the Jacobian matrix

Using the inverse solvers based on the optimisation, it is necessary to calculate the derivative of voltage measurements with respect to a conductivity parameter. The Jacobian or sensitivity matrix is the complete matrix of the partial derivatives relating a distributed set of impedance measurements and a conductivity distribution (Chin, 2010). The Jacobian matrix contains all the partial derivatives of the first order of a function vector valued and represents a linear approximation of a differentiable function near a given point.

The Jacobian matrix F' is calculated by multiplying Equation (2.16) by T and differentiating with respect to σ . Hence,

$$F' = T(Y^{-1}C)' = TQ \quad (2.18)$$

where the (i, j) th partition of Q is given by:

$$Q_{ij} = \frac{\partial Y^{-1}}{\partial \sigma_j} C_i. \quad (2.19)$$

The identity $Y^{-1}Y = I$ is used in place of Equation (2.13), which is then differentiated with respect to σ :

$$(Y^{-1}Y)' = (Y^{-1})'Y + Y^{-1}Y' = 0. \quad (2.20)$$

The derivative of the inverse of Y can therefore be written as:

$$(Y^{-1})' = -(Y^{-1}Y')Y^{-1}. \quad (2.21)$$

Substitution into Equation (2. 16) yields

$$\frac{\partial Y^{-1}}{\partial \sigma_j} C_i = -Y^{-1} \frac{\partial Y}{\partial \sigma_j} (Y^{-1} C_i) = -Y^{-1} \frac{\partial Y}{\partial \sigma_j} V_i. \quad (2.22)$$

The Jacobian matrix in the ERT system represents the sensitivity map linking a conductivity distribution to a particular boundary voltage measurement. The information on the effectiveness of ERT - related parameters and the precision of the inverse solution may be extracted by analysing the Jacobian matrix (Chin, 2010).

2.5 Applications of ERT

The ERT technique has been successfully applied in the field of biomedical, geotechnical and chemical engineering. This section explored the use of ERT in identifying two phase flow regime as well as the imaging of fluid bed using ERT.

2.5.1 Applications of ERT for industrial purpose

The purpose of process tomography is the ability to describe the internal composition of pipelines and mixing vessels. The progress made in the process industry in order to obtain the three-dimensional image reconstruction algorithm has been slow because of the absence of an effective way to compute the Jacobian matrix. Pinheiro *et al.* (1998) studied the application of a three-dimensional reconstruction algorithm in the process tomography industry, in which the image reconstruction procedure was based on a 3-D data collection, 3-D forward modelling as well as 3-D image reconstruction.

In the process industry, the ability to image the inside of pipes when conveying fluids from one place to the other for monitoring and control, represents a great benefit. The use of ERT gives a relatively low-cost route to determine the dynamic state of the internal composition of the pipes in a non-destructive and non-intrusive manner (Pinheiro *et al.* 1998). The image or

tomogram produced by the ERT can provide a better understanding of the process kinetics of the fluid inside the pipe as well as the fluid dynamics of the process. It can also provide an online control the process in order to increase product yield and reduce energy consumption (Pineiro *et al.* 1998).

Wang, Dorward, Vlaev & Mann (1999) investigated the application of ERT in identifying pseudo-stationary gas/liquid mix using ERT. Throughout this investigation, it was shown that ERT can separate the changes in pattern of gas hold-up in 3-D, which is caused by variations in liquid phase viscosity.

ERT was used by William *et al.* (1998) as a diagnostic tool for analysis of mixed processes for the formulation of improved mixing models and mixer design in 3-D. It was demonstrated that ERT can be used for the quantification of solid-liquid mixtures behaviour in a rapid and non-invasive manner.

Figure 2.8 illustrates a three-dimensional image of the conductivity maps for gas-liquid dispersion when gas is injected into the base of the mixer. The region of high gas hold-up is indicated by the color red while the green / yellow indicate the intermediate hold-up.

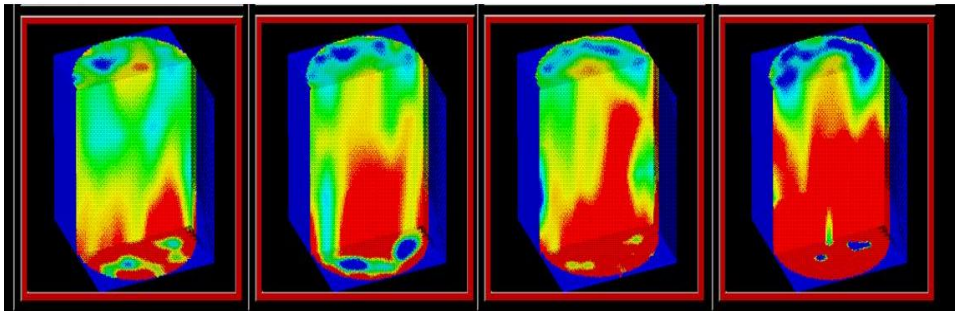


Figure 2.8 Conductivity maps for gas-liquid dispersion from a central sparger located at the bottom of the mixer for Rushton turbine (at 100 rpm) showing the effect of sparger rate (Williams *et al.*, 1998).

2.5.2 Applications of ERT for flow regime identification

ERT measurements can be used to identify the slurry flow regimes based on the flow velocity, the solids concentration and the particle characteristics. The determination of the slurry concentration profile can help in anticipating pipe blockages or slack flow which can take place in a gravity-assisted backfill distribution system and can also lead to excessive wear.

Flow patterns (flow regime) change with the properties of the solid particles relative to the properties of the liquid as well as the size of the pipe.

The classification of slurry flow regimes is done according to the profile of the solid phase concentration, which is also a function of the velocity inside the pipe. Based on the solid phase concentration, four main regimes can be defined in a horizontal pipe, namely: heterogeneous flow with a stationary bed, heterogeneous flow with a moving bed, heterogeneous flow and homogenous flow (Giguère, Fradette, Mignon & Tangy, 2008a; Crowe, 2006). ERT measurements can be used to identify the slurry flow regimes based on the flow velocity, the solids concentration and the particle characteristics (Qi, Dong, Xu, Wu & Hu, 2005).

The determination of the slurry concentration profile can help in anticipating pipe blockages or slack flow which can take place in a gravity-assisted backfill distribution system and can also lead to excessive wear (Giguère *et al.* 2008a).

Figure 2.8 illustrates the particle distributions profile of different slurry flow regimes in a pipe. The characteristic of homogeneous slurry flow is the even distribution of solid particles during the carrier liquid and across the pipeline cross section. It is also characterised by the high solids concentration of solid particles (Bolton, Hooper, Mann, & Stitt, 2004).

Heterogeneous slurry flow is characterised by the settling of sufficiently diluted solid particles to various degrees in a way that those particles are no longer consistently distributed in the flow.

In the flow regime with moving bed, the accumulation of the larger and/or denser particles at the bottom of the pipe forms the bed. The intensity of the moving fluid causes the particles in

the bed to slide along the bottom of the pipe. A stationary bed is formed due to the inability of a slow the moving fluid to enable motion of immersed particles.

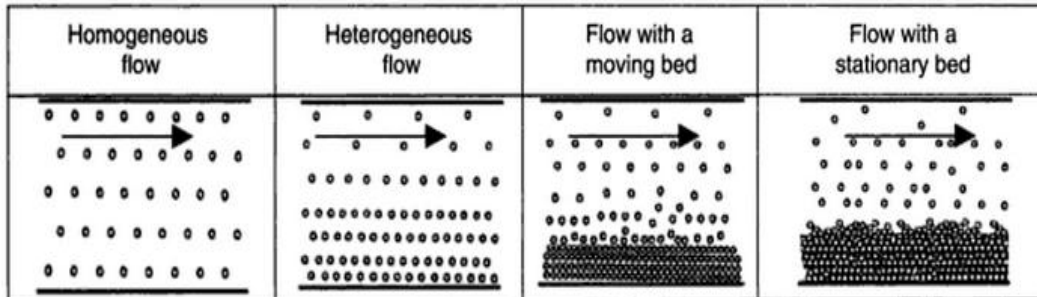


Figure 2.9 Illustration of particle distributions profile in a pipe for different slurry flow regime (Crowe, 2006).

Steven et al. 2008 investigated the imaging in three-dimension of solid-liquid suspension for changing agitation rates. Figure 2.10 shows the image comparison between MRI and ERT at the same concentration profiles.

The results were presented as voxel-resistivity distributions which provide a representation of the extent of mixing within the system (Stanley and Bolton, 2008).

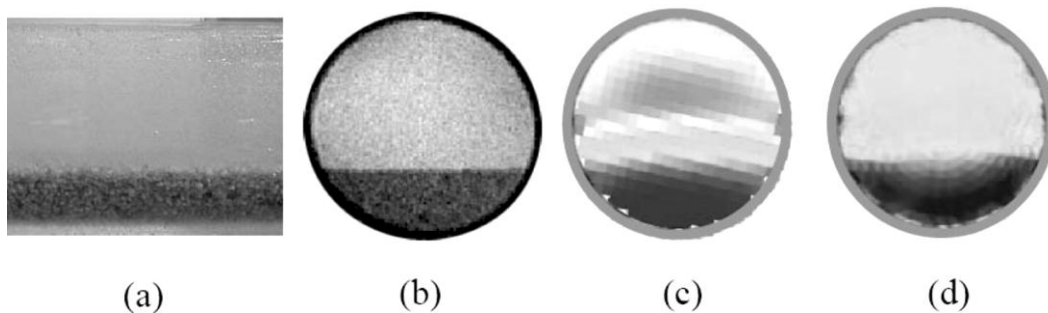


Figure 2.10 Comparison between ERT and MRI concentration profiles (a) photograph of sliding bed of sand particles in CMC taken during concentration data acquisition, (b) concentration map obtained with MRI, (c) real time concentration map obtained using ERT and (d) concentration map using ERT data and post-processing software (Stanley and Bolton, 2008).

2.6 Published Work Relevant to the Current Research

Stephenson, Mann and York (2008) investigated the effect that measurement strategies can have on electrical impedance tomography images. The adjacent and opposite techniques were compared in terms of image accuracy using different reconstruction algorithms. The impact of the choice of measurement techniques on the image-derived process metrics was also investigated, but no velocity and concentration profiles of the fluid were determined, neither was the level of sliding bed in the pipe.

Giguère *et al.* (2008a) conducted a study to identify homogeneous and heterogeneous slurry flow regimes. Transient tomograms, representing the concentration of solid phase, were computed using the LBP method and the GIA method. It appeared that, for a constant slurry velocity, the bed height tends to increase with the slurry concentration. The concentrations of homogeneous and heterogeneous slurry flow profiles were studied and compared using only the two algorithms, but assessment of the quality and accuracy of the algorithms were not conducted.

Giguère, Fradette, Mignon & Tangy (2008b) described quantitative image reconstruction techniques for an ERT system evaluated using synthetic and experimental test cases. The reconstructed images were compared using the GIA and LBP techniques. They demonstrated that a 2D model is suitable to solve the forward problem in the GIA method and that GIA can output quantitative images to visualise solid particle beds. The study was only limited to the comparison of reconstructed images of solid particle data with synthetic data, and no velocity and concentration profiles were determined.

A characterisation of the influence of pipe bend between slurry flow regimes in a horizontal pipe after a downward flow vertical bend section using ERT was conducted by Giguère *et al.* (2009). The onset of a particle bed was identified using the quantitative GIA image reconstruction method. It appears that the reconstruction of concentration tomogram using LBP algorithm could provide reliable quantitative measurements, although it over estimates the concentration of solid particles. No comparison regarding the degree of accuracy as well as the

quality of image was done since only one reconstruction algorithm was used to characterise the slurry flow concentrations.

2.7 Summary

It is clear that the 2-D images reconstruction algorithms have been extensively applied in the field of chemical processes. However, there has been very little research done on applications of the 2D or 3-D image reconstruction algorithms for the reconstruction of the internal composition or conductivity of vessels. Therefore, this research focused on the comparison of different 2-D algorithms with the aim of finding the accuracy of their computation.

Although previous work showed the potential of various algorithms for the reconstruction of ERT tomograms, no full characterisation and comparison of different algorithms could be found for real flow situations. A comprehensive analysis and comparison of different image reconstruction algorithms is needed where important parameters such as algorithm computational time, quality of images and accuracy for different experimental conditions are characterised and evaluated. This research work should therefore be considered as an important contribution to the field.

Chapter 3 RESEARCH EQUIPMENT AND METHODOLOGY

3.1 Equipment and Instrumentation

3.1.1 Experimental flow loop

The ERT system consists of fitted electrodes rings around a pipe, a data acquisition system used for the injection of current and measurement of voltage and a computer that communicate with the data acquisition and produce an image or tomogram.

The FPRC tomography rig consisted of a PVC clear pipe (internal diameter of 42.6cm) used to observe the flow, a centrifugal pump controlled by a variable speed drive (VSD) which allowed full control of the pump speed (flow rate), a tank with a conical base and a capacity of 160-200 litres. The rig also included an electromagnetic flow meter (Krohne Optiflux 4000) to measure the bulk flow rate, valves used to control the inlet (Sutherland, Slatter, Wilkinson, Randall; Long, 2005). The tomography rig was a cylindrical vessel made from non-conductive PVC. Two sets of electrode rings were fitted around the pipe section. Only one electrode ring was used for the measurements, the other ring served as a backup and at the same time provided a level ground to the electrode that was used to collect data. Salt was added to the water to provide a homogenous conductive medium.

Figure 3.1 shows a schematic of the experimental setup at the FPRC in Cape Town. The experimental procedure is explained in Section 3.2.

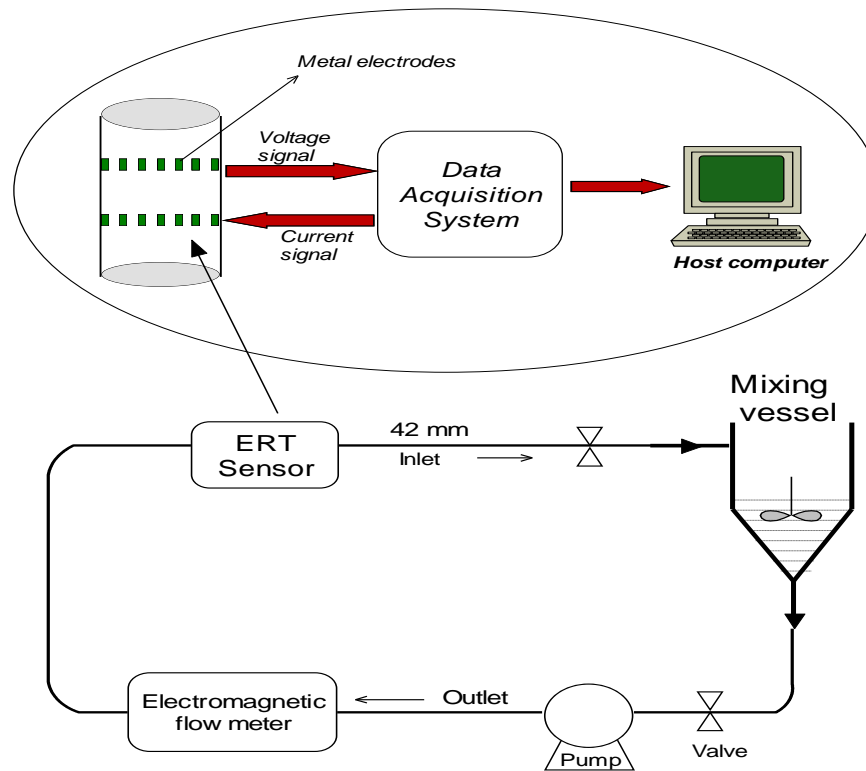


Figure 3.1 Experimental setup at the FPRC.

3.1.2 Off-line static pipe setup

Static tests were conducted separately from the flow loop. The main reason for these tests was to confirm the flow loop results.

As shown in Figure 3.2, the static set-up included a pipe of one metre in length with a radius of 42.6cm. Two set of electrode rings were fitted around the pipe separated by 10cm. The rings consisted of 16 stainless steel electrodes that were equally spaced around the boundary of the pipe. This experimental set-up was basically a duplicate of the set-up used in the experimental flow loop.



Figure 3.2 Static pipe setup fitted with two electrode rings

3.1.3 The Eagle Data Acquisition System (DAQ)

The Eagle data acquisition system (as shown in Figure 3.3) injects current and measures the voltages based on the measurement technique that is applied. The Eagle DAQ system is referred to as the Eagle USB I/O device in other works (Wilkinson, Randall, Long & Collins, 2006). It then communicates with the computer to load the measured data and then displays those measurements in a tomographic form which is shown in Figure 3.4. In this example the adjacent pair measurement sequence was applied.

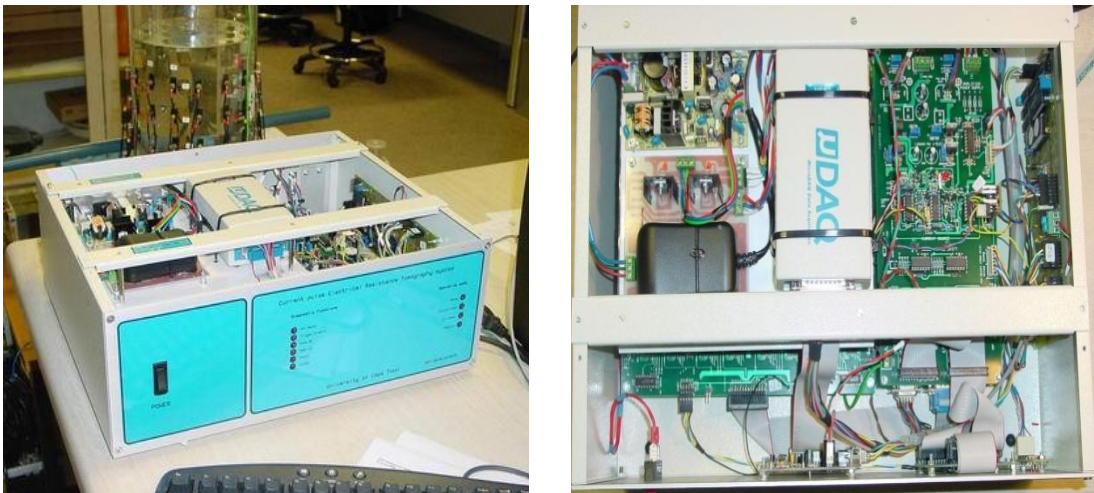


Figure 3.3 The Eagle DAQ (left), and the internal view of the DAQ system (right).

The adjacent measurement strategy was implemented during this research work, where by, current was injected through pairs of electrodes and voltage measurements were simultaneously taken through pairs of neighbouring electrodes. The current injections and voltage measurement are implemented by the data acquisition according to the sequence table downloaded to the instrument by the PC.

The ERT DAQ also communicates with the computer using special software which has an on-line reconstruction algorithm that displays the tomogram in real-time. The ability of the ERT DAQ to display a live tomogram (see Figure 3.4) enables the user to adjust settings (i.e. current injection level) before recording the data.

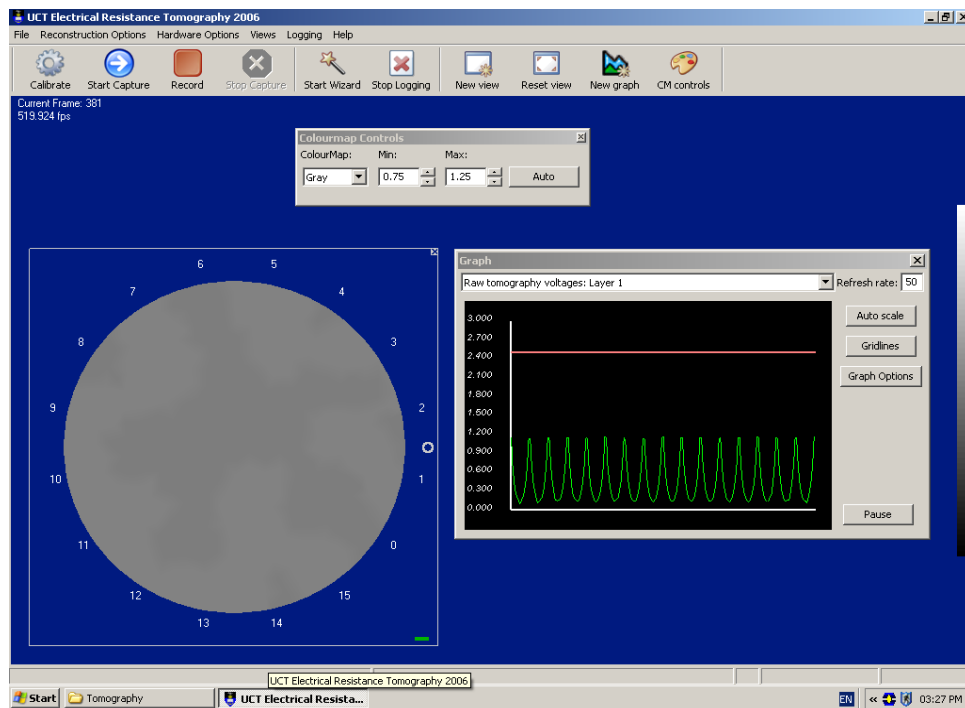


Figure 3.4 Picture of a tomogram showing the measurement using the adjacent measurement sequence with no object in the tank.

One ring of sixteen electrodes was used for the experiment, although the design of the ERT DAQ allowed up to eight rings of sixteen electrodes. Multiple rings are achieved by an additional multiplexing system. A version of the ERT DAQ instrument for single ring of 16 electrodes basic current pulse is shown in Figure 3.5.

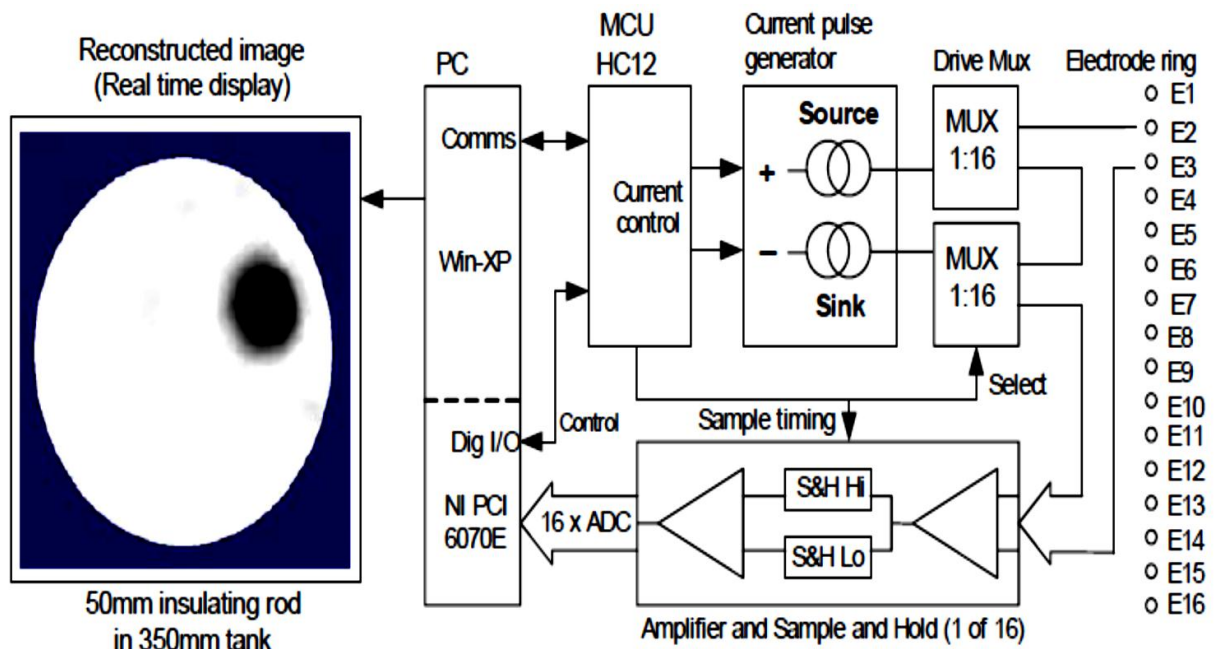


Figure 3.5 Basic current-pulse ERT systems for single ring of 16 electrodes (Wilkinson *et al.*, 2006).

The DAQ instrument consists of: the current source and sink circuits, a current drive multiplexers which is used to select the current drive electrode pair, a 16- channel amplifier which measures and amplifies the differential voltages between adjacent measuring electrodes simultaneously and the processor which is used to control the current pulse and measurement timing as well as the multiplexer (Wilkinson *et al.*, 2006).

Multiplexing strategies allow the implementation of different measuring sequence by adding multiplexer layer or modules connected in parallel. This also allowed the acquisition of data necessary for image reconstruction of a single layer, which consisted of a ring, fitted with 16 electrodes, that was attached to the circumference of the measuring vessel. The Eagle DAQ can achieve a three - dimensional data acquisition with four built-in multiplexing systems, which provides an array of 128 electrodes that is rearranged in eight rings of 16 electrodes or 4 rings of 32 electrodes (Randall, Wilkinson, Long & Collins, 2005).

The DAQ system has the ability to inject current in both opposite and adjacent sequences as well as voltage measurement on each ring. The adjacent measurement strategy was implemented using a single layer of electrodes as indicated in Figure 3.6 (Wilkinson *et al.*, 2006).

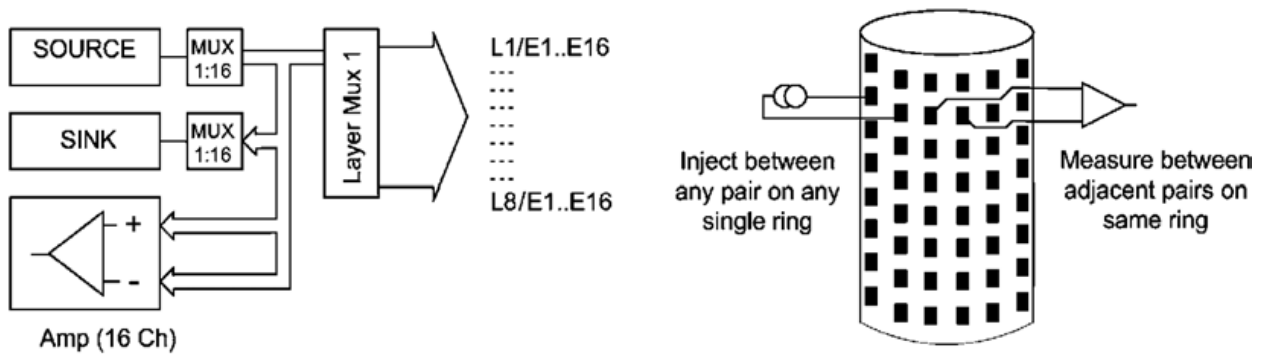


Figure 3.6 Single-layer multiplexer allows single plane measurements to be made on any one of eight rings (Randall *et al.*, 2002).

Figure 3.6 shows the injection of current between any pair of electrode on one layer and the measurement of voltage between adjacent pairs on the same layer. This configuration allows the recording of up to eight independent single plane data sets at a frame rate of 1000frames/second (Randall *et al.*, 2002).

Depending on the number of rings that are used, a single ring of 16 electrodes can produce 120 independent measurements based on the formula: $N(N - 1)/2$ where N represent the number of electrodes. 16 voltage measurements were made between neighbouring electrodes, in which three of the measurements had been discarded, resulting in 13 measurements per injection. The 120 independent measurements were therefore reduced to 104 independent measurements, because the voltage measurements that include the drive electrodes were cast-off (Randall *et al.*, 2002).

In order to implement a reconstruction algorithm, three sets of voltage measurement needed to be collected. These voltages represented the voltage distribution for homogeneous (i.e. there was no object inside the measuring vessel) distribution of the conductivity when no current was injected, the voltage distribution for homogeneous distribution of the conductivity when a fixed magnitude of current was injected and the voltage distribution for inhomogeneous (i.e. there is an object inside the measuring vessel) distribution of the conductivity when the same magnitude of current was injected. The first two voltage distributions were obtained during the ERT calibration procedure. These voltage measurements were then used in the inverse solver (*inv-solve*) developed by Electrical Impedance and Diffuse Optical Reconstruction Software (EIDORS) for image reconstruction.

The image reconstructions were based on the voltage difference between the inhomogeneous and homogeneous measurements when a certain current was injected into the solution, and the voltage measurements from the homogeneous solution when no current was injected into the solution.

3.2 ERT Calibration Procedure

When running the ERT system for the first time, one had to ensure that settings were put in place correctly. The user had to ensure that the instrument is properly calibrated. Therefore several steps had to be followed:

a. Calibration setup

The calibration of the ERT instrument started by filling up the pipe test with a homogenous medium with some added salt in order to increase the conductivity level of the medium. The saline water would then be used to calibrate the instrument.

b. Select a mesh and a precomputed file

In order to calibrate of the ERT instrument, a mesh and the precomputed file that was associated with it for the image reconstruction algorithm had to be selected. The precomputed file was useful to speed up the on-line reconstruction algorithm and contained the results of an off-line calculation.

c. Setting up the measurement sequence and testing serial comm

The communication between the software and the tomography instrument (ERT DAQ) had to be setup properly. This process involved selecting the proper download file which ran on the tomography hardware and contained the measurement sequence file. The measurement sequence file indicated the number of electrode rings that was used during the experiment. For

example, if the measurements were taken using one electrode ring, the sequential file would be seq_table_1L_indep as provided by the ERT software.

d. Setting the current level

The setting up of the current level was done manually according to the conductivity of the solution, the size of the electrode and the tank diameter used for the experiment. To make sure that the right level of current was selected, a graph window is provided to look at the raw voltage measurements. The user was able to adjust the current up until the voltages were at the right level (i.e. the measured voltages had to be under the reference voltage which was 2.4 V) while the instrument was running. This is shown in Figure 3.7. The current level adjustment would depend on the concentration of the fluid used for the experiment as well as the noise level that might occur during the measurement. Electromagnetic noise interference might be present due to pumps and process equipment.

Figure 3.7 shows the measured voltages when no current is applied and the measured voltages when a fix magnitude of current is applied.

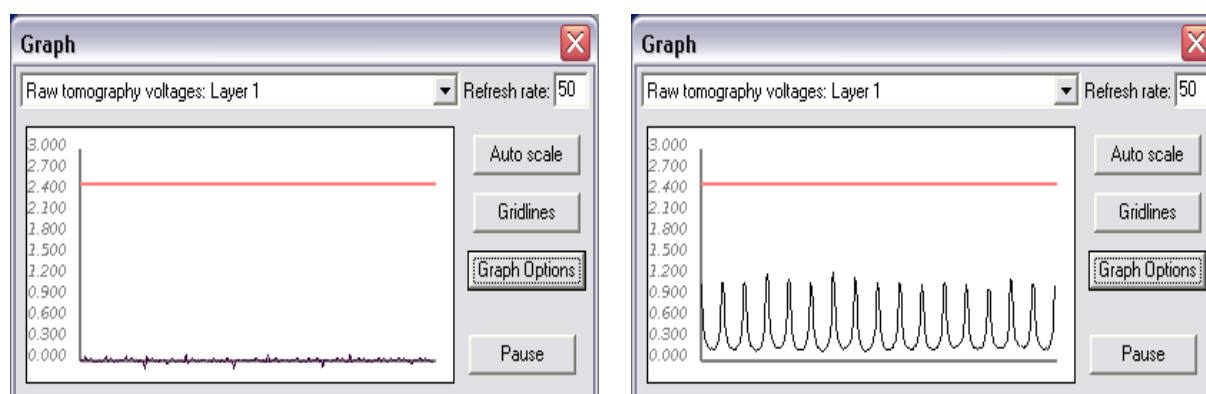


Figure 3.7 Data capture with no current applied and data capture with current applied.

e. Start the calibration

The calibration routine was done to capture a dataset used to calculate calibration factors. During this routine, the user was able to specify how many frames of data must be averaged and how long the instrument should run before saving data.

f. On-line reconstruction

The online reconstruction is done by pressing the start button. A tomogram of the measurement is then displayed on the computer as well as the colour map.

For all the experiments, the ERT instrument was set to average 100 frames per second with an injection current varying from 1.5mA to 2.5mA, and data was captured over 2 minutes.

A detailed calibration procedure can be found in the user manual in Appendix A.

3.3 Experimental Procedures and Investigation

The objective of this research was to investigate the performance of different reconstruction algorithms and compare them in different conditions or applications.

A series of experiments (shape tests, static level bed tests and flow loop tests) was conducted with the purpose of determining the performance of five 2-D reconstruction algorithms using EIDORS function and MATLAB software. The experiments were categorised into the following steps:

- the geometry of different objects when placed into a saline solution.
- the detection of the level bed formed by different plastic beads submerged into saline solution.
- the determination of the sliding bed inside a pipe when flowing at a constant speed (flow loop test).

3.3.1 Material tested

The experiments were conducted using a one meter long PVC pipe with a diameter of 4.26cm. The PVC pipe was fitted with an electrode ring placed at the middle with connecting cable attached to it. Bead particles were used to create different level beds, which represented the low conductivity distribution. Different objects were used and positioned at different places in the pipe, filled with a homogeneous solution (water and salt).

Black and white plastic beads with a diameter of 3mm were used. The size of the beads was big enough to settle within the water. This made it possible to create different flow regimes (e.g. sliding/moving bed flow) and test the efficiency of the selected algorithms. The white beads were mixed with black beads in order to follow the movement or speed of the settled bed. This also made it easier to determine and describe the flow conditions at different flow rates. Figure 3.8 shows the insulating materials that were submerged into the homogeneous solution to initiate the region of low conductivity distribution.

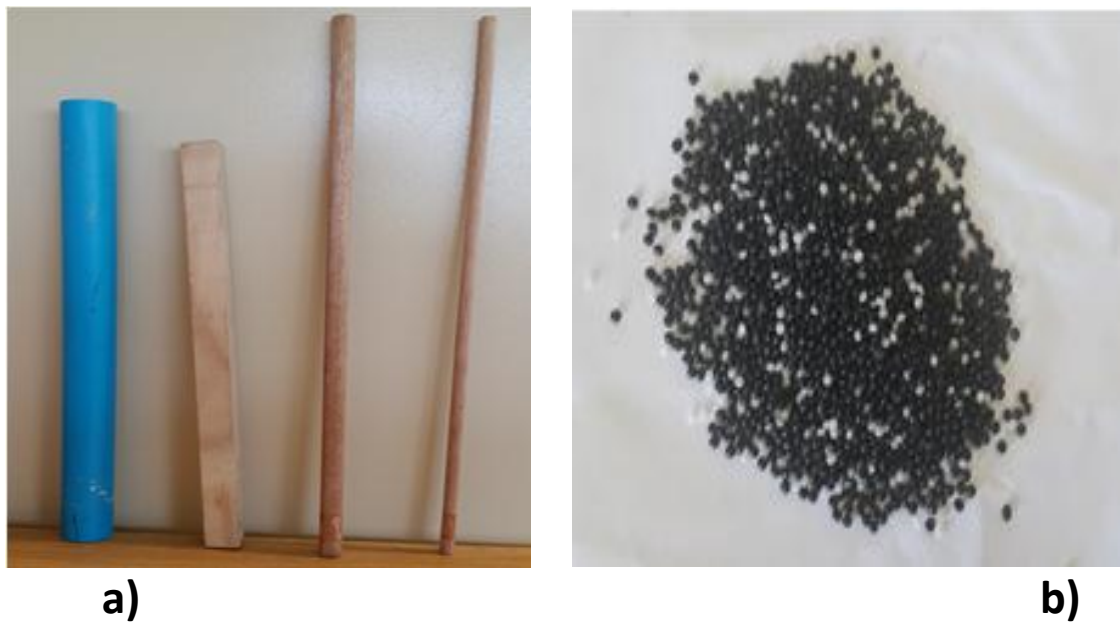


Figure 3.8 Different materials used in the experiment. a) 3.3cm blue pipe, 2x2cm rectangle wood, b) white and black beads (3mm).

3.3.2 The static experimental procedure

Different static tests were carried out using a PVC pipe of 1m long with a diameter of 4.26cm, on which two set of 16 electrodes were mounted. Although two rings of electrodes were fixed on the pipe section, only one ring was used for the measurement while the other ring was used to provide a ground connection which is also in contact with the solution inside the pipe.

a. The shape tests

Different shape tests were conducted using different current injections (1.5mA and 2.5mA). For these experiments, different sizes of objects were used. These objects were placed in the centre of the pipe (the 2x2cm square wood, the 3.3cm PVC pipe and 1.3cm rod wood), then on the side of the pipe (1.3cm rod wood) and finally two different objects were placed inside the pipe at the same time (1.3cm and 0.8cm rod wood). The purpose of these tests was to establish how well the selected algorithm could reproduce the edges and shapes of different objects.

Figures 3.9 and 3.10 show the different measurement configurations.

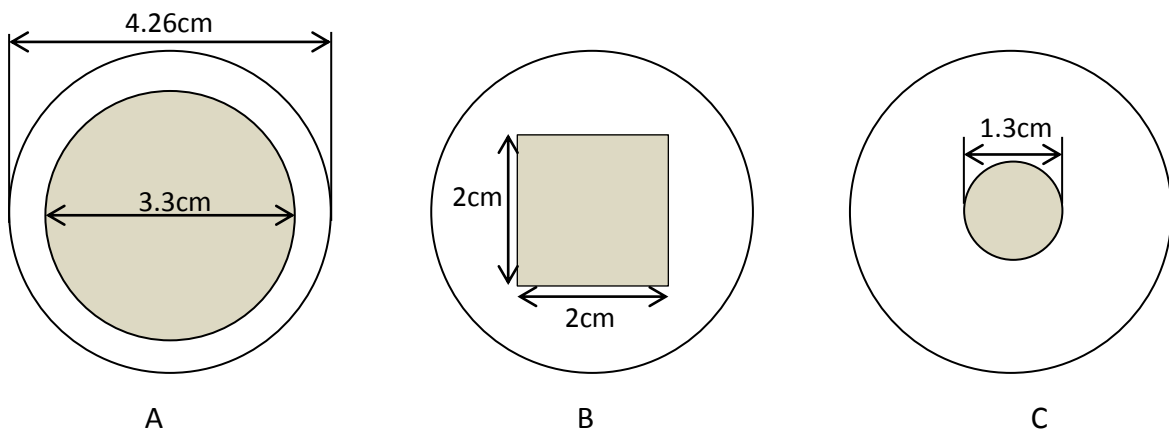


Figure 3.9 Shape test set up using a PVC pipe with 4.26cm in diameter: A) 2x2cm square wood position in the centre of the pipe, B) PVC pipe with 3.3cm diameter placed at the centre of the pipe and C) Rod wood with 1.3cm diameter position in the centre of the pipe.

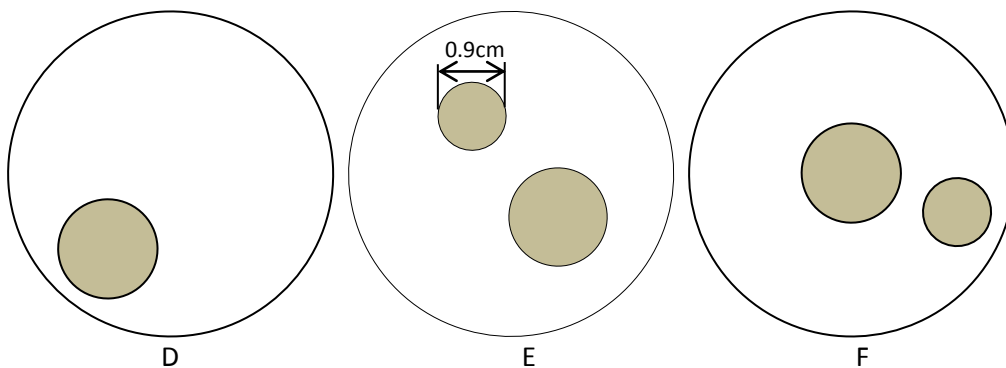


Figure 3.10 Shape test set up using a PVC pipe with 4.26cm in diameter: D) Rod wood with 1.3cm diameter placed on the side close to the edge of the pipe, E) Two rod woods with 1.3cm and 0.8cm diameters placed inside the pipe.

diameter position both in the pipe close to the edge and F) Two rod woods with 1.3cm and 0.8cm of diameter position both in the pipe, the 1.3cm in the centre and the 0.8cm close to the edge.

b. Level bed tests

The level bed tests were conducted with plastic beads submerged in saline water. Three different levels of bed were made using the beads as shown in the Figure 3.11. The objective of the level bed experiment was to determine how well the selected algorithms could detect the height of impurity inside the pipe.

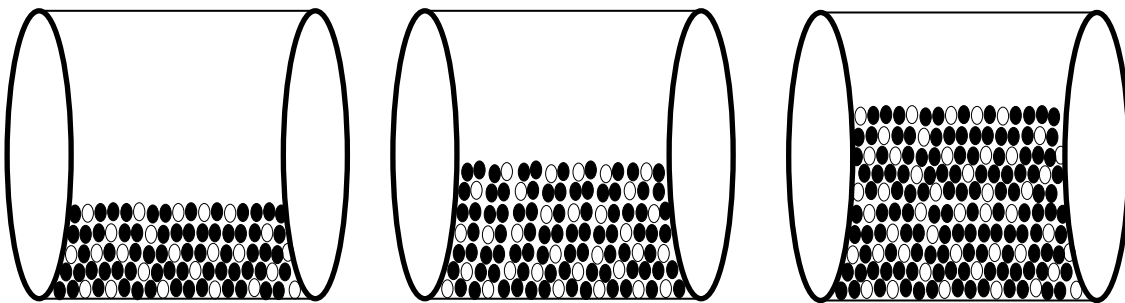


Figure 3.11 Static tests set up using a PVC pipe with 4.26cm in diameter, with different level bed formed by beads submerged in saline water.

During the experimental setup, the first level bed was measured at 1.5cm (L1), the second level bed at 2.4cm (L2) and the third level bed at 3.7cm (L3). These measurements were taken from the pictures shown in Figure 3.12.

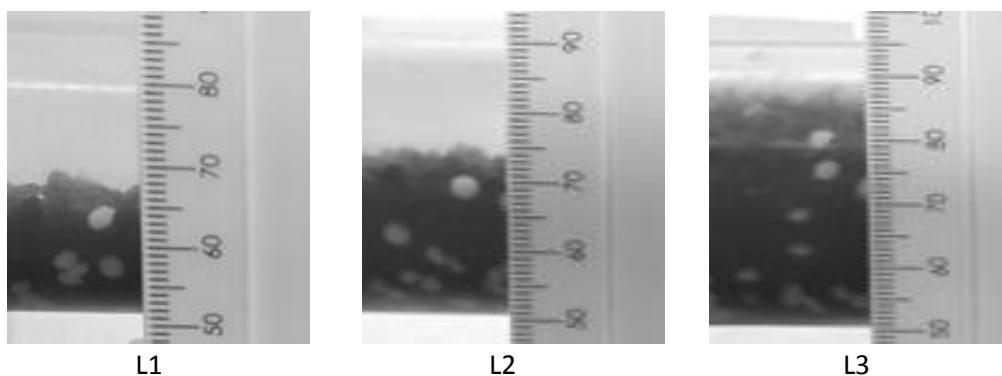


Figure 3.12 Experimental static test setup 2: Photographs of different level of bed formed by sand submerge into water.

c. The flow loop tests

The flow loop test was conducted in the flow loop rig in Figure 3.1 (see Section 3.1) using saline water and beads. The calibration procedure (see Section 3.2) that was applied for the shape test and static test was also applied to the flow loop. Measurements were taken with three different flow rates:

- The first flow rate was set at a slow speed of 0.86 litres per second. In this case, the flow consisted of slow moving bed at the bottom of the pipe with a few beads and water flowing on top of the pipe.
- **The second flow rate was set at 1.3 litres per second (l/s). The flow condition was partially suspended with a faster and constant moving bed at the bottom of the pipe.**
- **The third flow rate was set at 2.82l/s. The flow condition was suspended with a visible moving bed at the bottom of the pipe.**
- **Finally the last flow rate was set at 4.5l/s. The flow in this case is fully suspended, with no visible level bed and water and beads mixed together.**

The purpose of these tests was to determine how accurate the ERT system and image reconstruction algorithms were in detecting the level bed heights when different flow regimes and flow conditions were applied.

3.4 EIDORS Software

Electrical Impedance and Diffuse Optical Reconstruction Software (EIDORS), version 3.7, which is a public domain and MATLAB (R2014b) tool kit, was used in this research (Adler & Lionheart, 2006). The choice of EIDORS open source is based on the fact that it is capable of addressing the ill-posed and nonlinear inverse problem of the ERT. These problems are usually solved using a finite element model (FEM) to solve the forward problem and the regularized Newton's method to solve the inverse problem (Polydorides and Lionheart, 2002).

EIDORS software consists of four primary objects: *data*, *image*, *fwd model*, *inv model* and each object is represented by a structure (Adler & Lionheart, 2006). The solution to the inverse problem is achieved by first solving the forward problem which consists of calculating predicted voltage measurements given the properties of the interior material; then secondly, computing the Jacobian matrix which consists of calculating the electric fields in the interior material (Polydorides *et al.*, 2002). During the course of this research, the prediction of voltage measurements was replaced by the calibration data obtained from the ERT instrument.

The flow chart of the reconstruction code is shown in Figure 3.13.

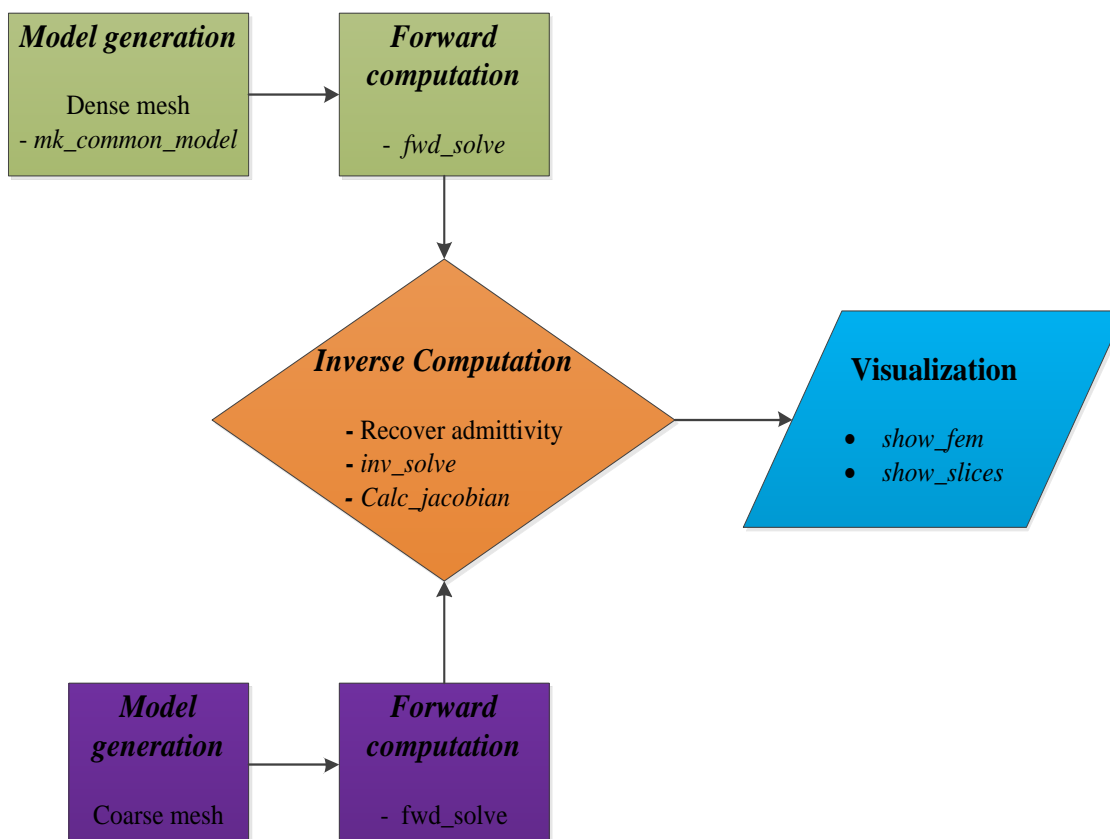


Figure 3.13 Flow chart of the reconstruction procedure (Ahn S., 2011).

3.4.1 Solving the forward problem

The forward problem is the problem solved by finding the electrical potential between the electrode pairs for a given current injection (Giguère *et al.* 2008b). Due to the complexity of the equation used in the forward problem, the finite element method (FEM) is normally used to obtain the solutions to the forward problem.

As shown in Figure 3.14, the basic idea of FEM is to obtain an approximate solution by dividing the body into finite elements, connected by nodes, which is also called the finite element mesh, using the process called mesh generation.

The FEM offers an efficient methodology through which the solution can be determined using a computer program. The solution for linear problems is determined by solving a system of linear equations, and the results are generally presented as computer visualisation (i.e. tomogram).

The finite element methodology used in addressing the forward problem can be summarised into four steps: (1) Preprocessing, which subdivides the problem domain into finite elements, therefore generating a mesh, (2) Development of partial differential equations for the finite elements, during which the behaviour of each element is described, (3) Assembly, which consists of finding the equations of the complete system using the equations of individual elements, (4) Solving the equations, (5) Postprocessing, during which the visualisation of the response are obtained (Fish & Belytschko, 2007).

Figure 3.14 shows an example of a finite element meshes.

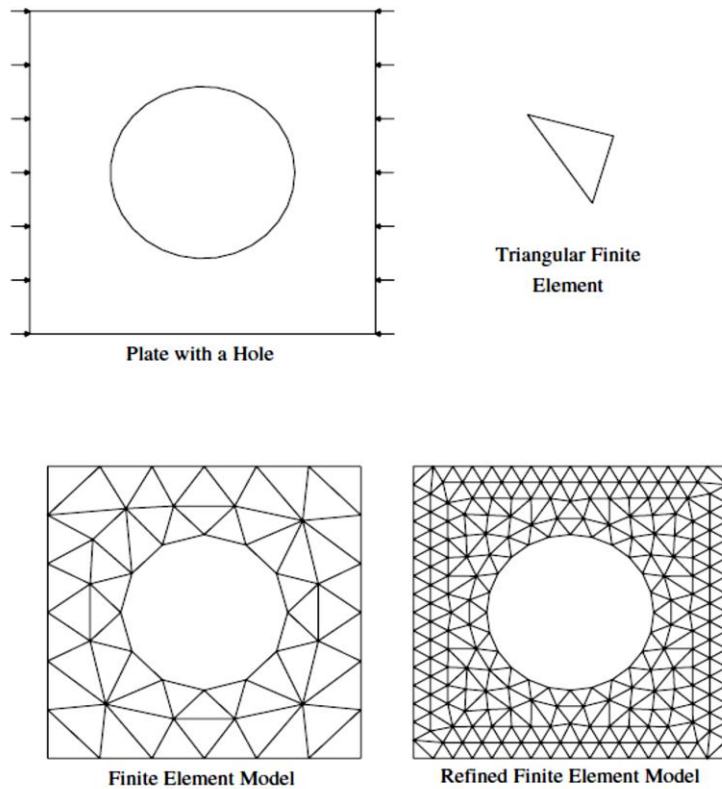


Figure 3.14 Geometry, loads and finite element meshes (Fish et al., 2007).

The FEM transforms the forward problem into one of solving a set of linear equations, which is a well-posed or stable problem (Karhunen *et al.*, 2010). In this case, ERT provides an approximation of the potential differences for a given conductivity distribution (Pinheiro *et al.*, 1998; Giguère *et al.* 2008b).

The forward computation include three main functions: (1) the functions responsible for constructing the global admittance or system matrix, (2) the functions responsible for setting up the current patterns and (3) the functions which solve the forward problem by extracting the array of boundary measurements.

The calculation of the Jacobian is also an important element needed for the reconstruction using the interior electric fields.

In a domain Ω with an admittivity distribution $\xi \in \mathbb{C}^k$, the electric potential u satisfies the partial differential equation:

$$\nabla \cdot \xi \nabla u = 0. \quad (3.1)$$

The complete electrode boundary conditions are defined by the equations:

$$V_l = u + z_l \xi \frac{\partial u}{\partial n}, \quad (3.2)$$

$$I_l = \int_{E_l} \xi \frac{\partial u}{\partial n} dS, \quad (3.3)$$

where I_l is the current injected from the l^{th} electrode E_l which has a contact impedance z_l , and V_l is the constant voltage on the electrode E_l , n the outward unit normal vector, and

$\xi \frac{\partial u}{\partial n} = 0$ is the current density on the boundary inter-electrode gap (Somersalo, Cheney & Isaacson, 1992).

The `forward_model` (*fwd_model*) in EIDORS is a function designed to represent the finite element model, the electrode positions and properties, the simulation patterns as well as the pointers to functions to solve the forward problem (Polydorides *et al.*, 2002).

Figure 3.15 illustrates the structure of a *fwd_model*.

The FEM is described by the fields nodes ($V \times D$), elems ($N \times (D + 1)$), and boundary ($B \times D$), where V is the number of vertices, N is the number of unknown conductivities to be solved by the inverse solution, B the number of simplices with a face on the boundary, and D the model dimension ($D = 2$ for 2D and $D = 3$ for 3D). The electrodes are specified by a vector ($E \times 1$) of electrode fields. Each E electrode objects has `z_contact` fields and nodes which represent the (possibly complex) contact impedance and vertices to which that electrode is connected.

There are three function pointers involved in the solution of the forward problem: *solve*, *jacobian* and *system_mat*. The function name (as a string) or a function pointer to calculate these quantities are contained in each field. These quantities are solved using the utility functions *fwd_solve()*, *calc_jacobian()* and *calc_system_mat()* (Adler *et al.*, 2006). During this research work, the *fwd_solve* was not used for the reconstruction because the simulated data used by Adler *et al.* (2006) was replaced by the calibration data obtained from the ERT instrument.

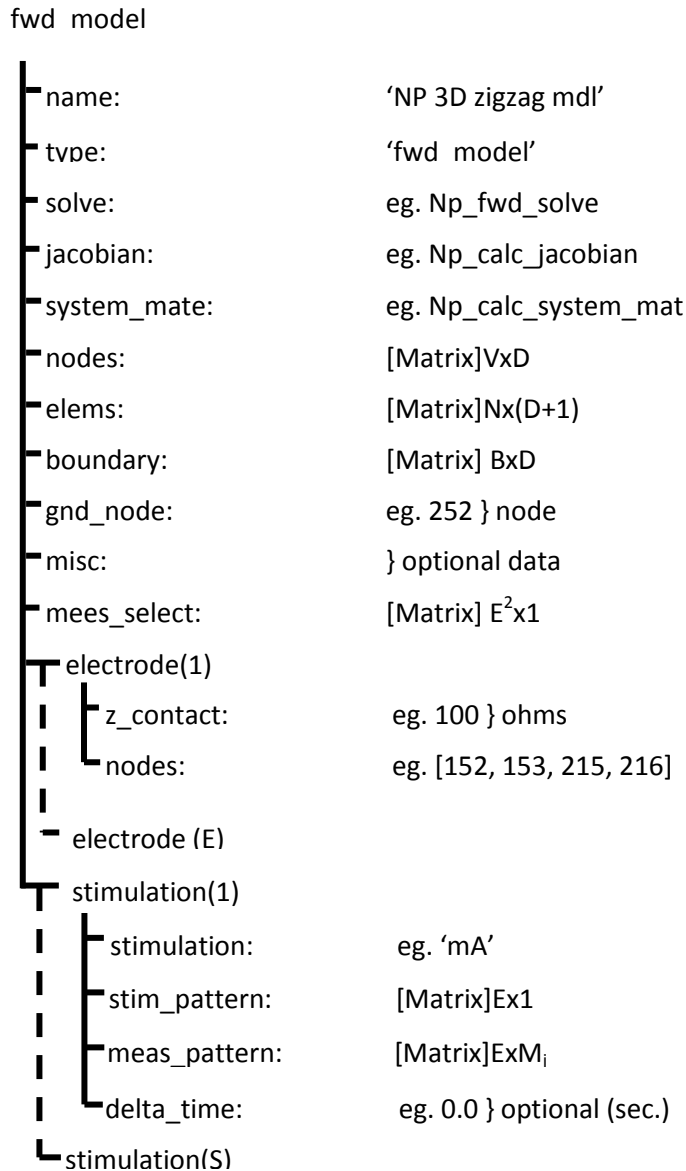


Figure 3.15 Structure of the EIDORS fwd_model objects (Adler et al., 2006).

3.4.2 Solving the inverse problem using EIDORS

There are two approaches in solving the inverse problem. The first approach, referred to as Gauss-Newton method, eliminates the second derivative terms of the non-linear forward problem as described by the Taylor expansion. It then constructs a generalise inverse of the Jacobian and consequently inverts the well-posed problem using the Newton-Raphson method. The second approach considers a linearised form of the inverse problem and then adopts a

Tikhonov type regularisation method to obtain a step solution within the Newton-Raphson algorithm (Kim, Kim, Kim, Lee, Park, Lee & Choi, 2000; Vauhkonen *et al.*, 1999 & Holder *et al.*, 2008).

The inverse problem aims at obtaining a stable solution ξ^* which minimises the residual error

$$f(\xi) = \frac{1}{2}(F(\xi) - V)^*(F(\xi) - V) = \frac{1}{2}\|F(\xi) - V\|_2^2 \quad (3.4)$$

where $F(\xi) : \mathbb{C}^n \rightarrow \mathbb{C}^m$ is the non-linear forward operator in a problem with n parameters (voxels) and m measurements, and $V \in \mathbb{C}^m$ is the vector of voltage measurements for a fixed set of current patterns (Adler *et al.*, 2006).

As shown in Figure 3.16, the *inv_model* object assembles informations that are necessary for the reconstruction of images. There are two basic types of reconstruction based on the *reconst_type* field “*difference*” and “*static*”. The *reconst_type* “*difference*” calculates an image based on the difference between two data objects while the “*static*” calculates an image based on a single data object. In this research, the inverse reconstruction was solved using three data sets, therefore the reconstruction type “*difference*” was used for the image reconstruction.

The solver functions used for the inverse problem require an *image prior* and a choice of *hyperparameter*. Those functions are based on regularised image reconstruction algorithms. There are two ways of using the image priors, using either a regularisation term of $\|\lambda R x\|$ or a regularisation term of $\|\lambda x\|_R$, where x is the vector of image element values.

EIDORS defines two different functions that can be used to calculate the image priors. These functions are: *R_prior* and *RtR_prior*. Therefore it is really important to make sure of which type of image prior is necessary and provide a value for either of them or both of them (Adler *et al.*, 2006).

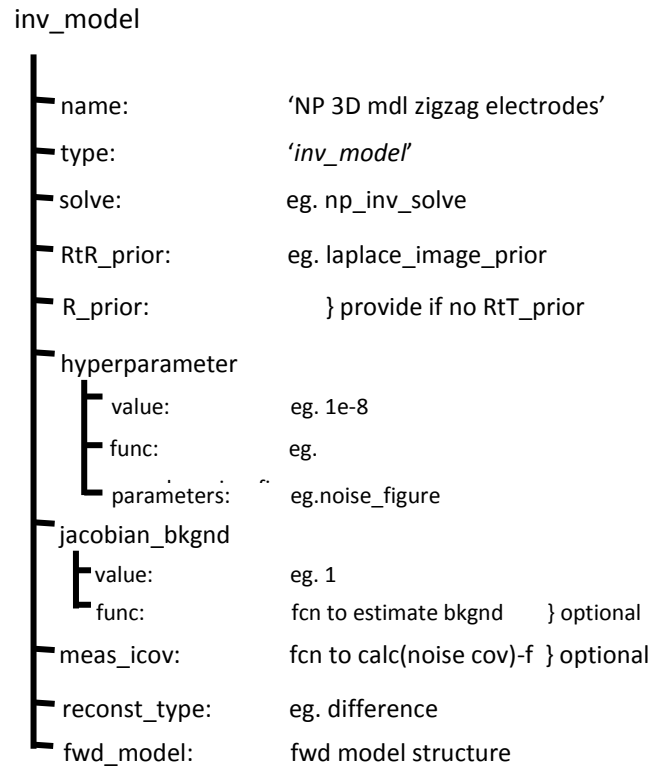


Figure 3.16 Structure of the EIDORS `inv_model` object (Adler *et al.*, 2006).

3.4.3 Step-wise approached into solving the forward problem using EIDORS

a. Creating a two dimensional mesh using EIDORS

In addressing the forward problem, the first step requires generating a two-dimensional mesh using the function `mk_common_model` on line 55 in Figure 3.17.

```
55 - imdl= mk_common_model('d2c0',16);

54 % Simulation (forward model) 1024 elements
55 - imdl= mk_common_model('d2c0',16);
56 - fmdl= imdl.fwd_model;
57 - fmdl = ReplaceStimulationPattern(fmdl, drive_lay, drive_elec, sense_lay);
58 - sim_img= mk_image(fmdl,1);
59 - v_homg= fwd_solve(sim_img);
```

Figure 3.17 Line of code used to solve the forward problem.

The `mk_common_models` is a utility function used to create common ERT FEM models. It calls the basic function as a string such as 'c2d0c'. Table 3.1 shows the details specification of the 'c2d0c' model.

Table 3.1 Detail specifications of the 'c2d0c' model available from `mk_common_model`

c	Vertex density (a=low, j=high)
2	Two dimensional
d	Use the "distmesh" generator
0	Electrode refinement level is 0 (no refinement)
c	Circular model

b. Creating an EIDORS-object with appropriate input variables

The EIDORS object includes input variable with well-defined properties. The EIDORS is required by the forward solver function and includes the type (image) and the forward modelling mesh linked to the object (fmdl) with the name fwd_model, as shown in line 56 of Figure 3.17.

```
56 fmdl= imdl.fwd_model;
```

c. Defining the Stimulation Pattern of Sequence of Current Injections and Voltage Measurement on the Periphery Electrode

For every current injection made on the electrode ring, voltage measurement must be made on the boundary do the electrode, around the perimeter of the domain of the vessel, in a 2-dimensional way. The *mk_stim_patterns* function in EIDORS is the function used to create different current injection sequence and voltage measurement. The function *ReplaceStimulationPattern (fmdl, drive_lay, drive_elec, sense_lay)*, called in line 57 of Figure 3.17, replaces the simulation patterns of an EIDORS forward model with one matching the sequence file of the ERT instrument.

```
57 fmdl = ReplaceStimulationPattern(fmdl, drive_lay, drive_elec, sense_lay);
```

d. Creating an EIDORS image object

The EIDORS image object is created by *sim_img*, which combines the forward modelling mesh and the conductivity of each element contained in the mesh, as shown in line 58 of Figure 3.17.

```
58 sim_img= mk_image(fmdl,1);
```

e. Calling the Forward Solver Function to Solve for the Boundary Voltages Arising from Injecting Current into a Homogeneous Solution

The forward solver function *fwd_solve* (as shown in line 59 of Figure 3.17) is a function that was used to solve the boundary voltages when current was injected. The *forward_solver* solves the forward problem using different methods such as: the LU decomposition for the

conductivity values that lies in the set of complex numbers, the Cholesky method or the preconditioned conjugate gradients for the conductivity values that are real (Polidorides, 2002).

```
59 v_homg = fwd_solve(sim_img);
```

3.4.4 Step-wise approach into solving the inverse problem using EIDORS

a. Creating an EIDORS Object for the Inverse Solver Function

The inverse solver function just like the forward solver function requires an EIDORS object (*eidors_obj*) with input variables and properties as shown in line 71 of the line of code in Figure 3.18. Since the reconstruction was done using the difference between two data objects, the reconstruction type 'difference' was selected as show in line 72.

```
70 % Create Inverse Model
71 inv2d= eidors_obj('inv_model', 'EIT inverse');
72 inv2d.reconst_type= 'difference';
73 inv2d.jacobian_bkgnd.value= 1;
74 inv2d.fwd_model= imb.fwd_model;
75 inv2d.fwd_model.np_fwd_solve.perm_sym= '{y}';
76
77 % Guass-Newton solvers
78 inv2d.solve= @inv_solve_diff_GN_one_step;
79
80 % Laplace image prior
81 inv2d.hyperparameter.value = 1e-3;
82 inv2d.RtR_prior= @prior_laplace;
83 imgr= inv_solve( inv2d, caldata, v);
84 show_fem(imgr);
85 show_slices(imgr);
```

Figure 3.18 Line of code used to solve the inverse problem.

Using the Nick Poldorides's function, the jacobian matrix was computed using line 73 in Figure 3.18.

```
73 inv2d.jacobian_bkgnd.value= 1;
```

In order to fully solve the inverse problem, Laplace image prior (@prior_laplace) was explored in line 82, while the Automatic hyperparameter used the Gaussian HPF prior (@prior_gaussian_HPF). Tthe Conjugate Gradient and the Total Variation used the TV prior

('prior_TV'). The Gauss-Newton solver (@inv_solve_diff_GN_one_step) was used in association with the Laplace prior and Gaussian HFP prior. In the other hand, the Conjugate Gradient used the conjugate gradient solver ('inv_solve_conj_grad'), while the Total Variation used the total variation solver ('inv_solve_TV').

The hyperparameter value, which is a very important parameter for the inverse reconstruction, is specified on line 81 in Figure 3.18.

b. Calling the Inverse Solver Function and Plotting the Reconstructed Images in 3-D and 2-D

Two main functions are provided by EIDORS for visualising tomography images or results: *show_fem()* and *show_slices()*. The *show_fem* function plots the finite element mesh used in the reconstruction in 2D. For example, *show_fem(fwd_model)* plots the empty tank mesh showing the electrodes, *show_fem(inv_img)* plots the mesh and tries to find areas of conductivity that are different from the background value. The *show_slices* displays an arbitrary set of planar slices through the model (Long, 2006; Adler *et al.*, 2006).

Line 83 of the line of code in Figure 3.18 shows the inverse solver function (*inv2d*) with input variables set as the EIDORS object, the data sets from the simulated voltages for homogeneous solution (*caldata*) and the data sets from the measurement for inhomogeneous solution (*v*). Line 84 and 85 display the solution of the *inv_solve* (*img*) in a two-dimensional mesh by calling the function *show_fem*. The *show_slices* (*img*) in the other hand displays the two-dimensional plane of the reconstructed image in slices.

c. The effect of the hyperparameter on the image reconstruction

The hyperparameter selection was important for a qualitative image reconstruction. Naturally, hyperparameter selection should yield solutions that preserve the measured data as much as possible by applying minimal apriori information to obtain a useful reconstructed image (Graham, 2007; Graham *et al.*, 2006).

Although heuristic technique is empirical, it is quick to implement (Tapp *et al.*, 2003). Heuristic selection is one of the most common methods of selection of the hyperparameter (Adler, Dai & Lionheart, 2007). It consists of examining a set of image reconstructions that are generated over a range of hyperparameter values, then select the value that produce a reconstructed image close to the reference images (Queiroz, 2012; Graham, 2007).

The heuristic approach was used during the experiments in order to select the appropriate hyper-parameter which would produce the best reconstructed images for each experiment.

Figure 3.19 shows reconstructed images of 3.3cm round PVC pipe using Laplace Prior algorithm with different hyperparameter values.

Figure 3.19 (B) shows the reconstructed image using a hyperparameter of $1e-3$ (i.e. 0.001), which do not give a good qualitative and distinguishable image. Figure 3.19 (C and D) were obtained using hyper-parameters values of $15e-3$ (i.e. 0.015) and $30e-3$ (i.e. 0.03) respectively. As shown, the images were of a better quality than the one on Figure 3.19 (B).

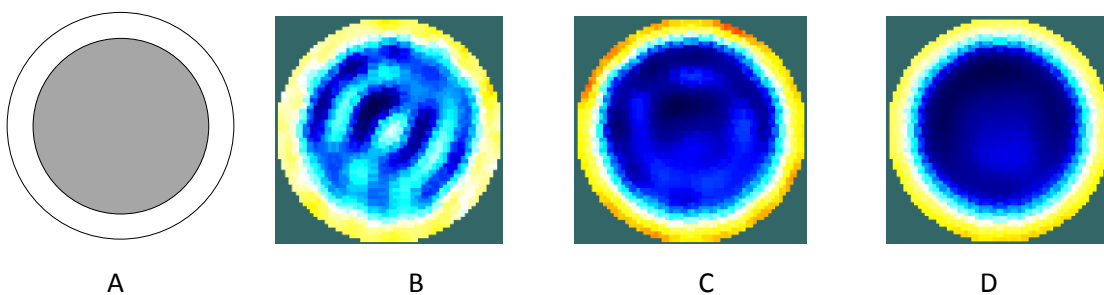


Figure 3.19 A- Initial configuration (3.3 cm PVC pipe), B to D - reconstructed images using Laplace prior with hyperparameter value of: $1e-4$, $1e-3$ and $30e-3$.

The selection of the best image was done based on the criteria explained in section 3.62.

3.5 Image Reconstruction Algorithms used in this work

3.5.1 Overview of some selected reconstruction algorithms

The choice of a suitable algorithm and related numerical parameters frequently requires a trial-and-error scheme in order to reach a solution comparable to the experiments.

Stephenson *et al.* (2008) established that the conjugate gradient and the Nonlinear Gauss Newton algorithms appear to produce reconstructed images with a quality that are the most accurate representation of the target distribution.

The study conducted by Borsic A. (2002) show that the Total Variation (TV) regularisation yield to an image reconstruction which is able to retain sharp features of reconstructed block images.

Sarode *et al.* (2013) made a comparative study of various 2D algorithms such as Gauss-Newton algorithm with priors like Noser, Laplace and Tikhonov, the Total Variation algorithm and the Back Projection algorithm. It was proven that the Gauss-Newton algorithm produced better images with respect to the size and the shape of the region of low conductivity. Furthermore, the Total Variation Prior provides superior circular shape and the size of the object as well as sharper reconstructed images compared to the other algorithms under investigation.

It was decided to implement and compare the Conjugate Gradient algorithm, the Total Variation algorithm and the Gauss-Newton algorithm with Laplace Prior. One of the algorithms which do not appear to be widely used by many researchers is the Automatic Hyperparameter Selection algorithm which is the Gauss-Newton algorithm with the Gaussian_HPFI Prior. For this reason, it was decided to include this as a fourth algorithm in this investigation. The fifth algorithm selected for the comparison is referred to as the One-step algorithm develop by Long (2005). The difference is that it works independently of EIDORS functions and operates only with MATLAB functions. This is also used in the UCT software that comes with the UCT ERT instrument. For each of these algorithms, the hyperparameter was selected using a heuristic approach.

3.5.2 Algorithm Characteristics

❖ ***One-step algorithm***

One of the characteristic of the one-step algorithm is the fact that it has no memory, meaning that it treats each new time step computation as an initial problem. The one-step algorithm does not use any previously computed solution points to produce a tomogram. One of the advantages of the one-step algorithm is that it is very fast and only requires a simple matrix multiplication (Long, 2005).

❖ ***Gauss-Newton algorithm***

Electrical impedance imaging is a highly nonlinear and ill-posed inverse problem in which a minimization algorithm is used to obtain its approximate solution. The Gauss-Newton (GN) algorithm is used to solve non-linear least squares problems. Although the Gauss-Newton algorithm can only be used to minimize a sum of squared function values, it has the advantage that second derivatives, which can be challenging to compute, are not required. An objective function is minimized by taking the difference between the experimental measurement data and the computationally predicted data (Islam and Kiber, 2014; Sarode *et al.*, 2013 & Adler and Rober, 1996).

Reconstructed images could be obtained using the GN solver with different priors such as the Gaussian High Pass Filter image prior (*prior_gaussian_HPF*) and the Laplace image prior (*prior_laplace*). The GN algorithm with the laplace prior is referred to as the Laplace Prior algorithm while the GN algorithm with the Gaussian HPD is referred to as the Automatic Hyper Parameter Selection (AHPS) algorithm.

❖ Total Variation algorithm

The algorithm reconstruction using the Total Variation algorithm produced sharper reconstructed images with preserved discontinuities (Sarode et al., 2013 & Borsic et al., 2010). The Total Variation algorithm used the total variation inverse solver using the Primal/Dual interior point method (*TV_pdlpm*), in association with the total variation prior (*prior_TV*). The number of iteration used was 10 with a tolerance of 0.001.

❖ Conjugate Gradient algorithm

The conjugate gradient method is an algorithm used for the numerical solution of particular systems of linear equations. The conjugate gradient method is often applied as an iterative algorithm, applicable to sparse systems that are too large to be handled by a direct implementation or other direct methods. The conjugate gradient method can also be used to solve unconstrained optimization problems (Avriel, 2003). Reconstructed images were obtained using the conjugate gradient algorithm, which incorporated the conjugate gradient solver (*solve_conj_grad*) with the laplace prior (*prior_laplace*). A number of 1000 iteration was used with a tolerance of 0.001.

3.6 Algorithm Performance Criteria

The reconstructed images obtained from the various reconstruction algorithms were compared based on different criteria such as: the running time of each algorithm, the quality and the accuracy of the reconstructed images.

3.6.1 Running time

The reconstruction computational time of each algorithm were tested. Each algorithm requires a certain amount of time in order to produce a tomogram. By calculating that time it easy to determine which algorithm performs faster. Table 3.2 shows the specifications of the personal computer (PC) used for the image reconstructions.

Table 3.2 Personal Computation specifications used for the image reconstructions

Model	Toshiba
Processor	2.13GHz Dual Core
RAM	4GB
System architecture	64-bit
Hard drive	Solid state
OS	Window 8
Graphics	Intel

The running time was obtained using the average measurement data capture over two minute.

3.6.2 Image quality and distinguishability

The quality of the images was compared based on the large conductivity difference. The image distinguishability of the chosen algorithms was investigated and compared. The quality of the images obtained from each algorithm was measured based on visual inspection, i.e. based on how well the algorithms were able to reconstruct the shape of the different objects used in the

shape test experiments. For the level bed and flow loop tests, photos were taken in order to evaluate the quality of the reconstructed images. Although the background colour varied, it did not affect the visual analysis as the focus was on the dark blue.

The criteria used to score image distinguishable was:

- 1- Poor representation of real shape (shape out of proportion, completely different shape from the actual shape used in the experiment). See Figure 3.20.



Figure 3.20 On the left: the real shape and level bed used in the experiment, on the right: Image of a poor representation of the real shape and the level bed.

- 2- Average representation of the real shape (i.e. shape can be distinguished, but not 100% comparable). See Figure 3.21.



Figure 3.21 On the left: the real shape and level bed used in the experiment, on the right: Image of an average representation of the real shape and level bed.

- 3- Very good representation of the real shape. See Figure 3.22.



Figure 3.22 On the left: the real shape and level bed used in the experiment, on the right: Image of a good representation of the real shape and level bed.

3.6.3 Accuracy

The adjacent measurement strategy applied during the experiment produces voltage data sets with which the voltage distribution of the values of resistivity of the resulting solution of the inverse problem must be the same as the actual distribution. Distribution map of the resistivity was measured by comparing the area of the actual object with the area of the region of high resistivity values of the corresponding reconstructed image.

Figure 3.23 shows the resistivity of the region increases with the degree of 'blueness' and is the region between 0 and 30% in the colour bar scale maps, whereas the 'redness' indicate the region of high conductivity.

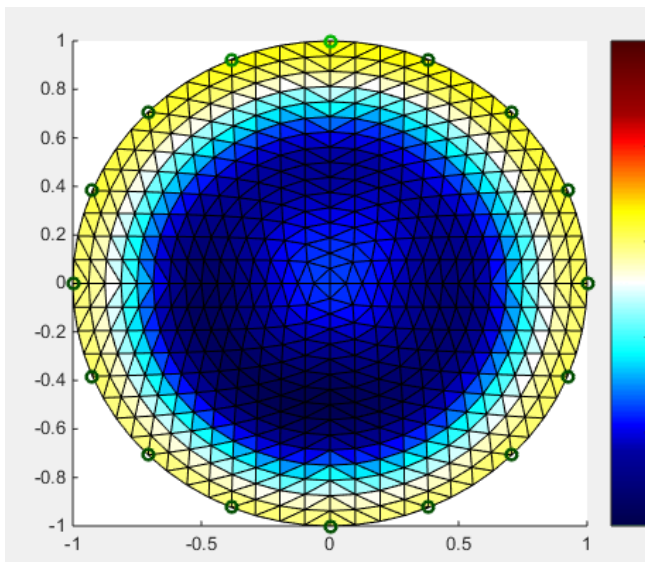


Figure 3.23 Resistivity map of the solid object based on the colour bar scale.

The accuracy at which the selected algorithms reconstructed the objects and level bed was investigated. For the shape test experiment, the actual area of low conductivity was calculated (using various shapes) and compared to the actual area of the object used in the experiment. For the level bed and the flow loop test experiments, the comparison was done based on the height of the level bed. In this way, another quantitative measurement and percentage error could be obtained and compared for different reconstruction algorithms using Equation:

$$PE = \left| \frac{\text{Actual Area} - \text{Reconstructed Area}}{\text{Actual}} \right| \times 100 \quad (3.4)$$

where the Actual Area is equal to the area of the object placed inside the pipe test.

The method used for the calculation of the area of low conductivity is shown in Figure 3.24. The threshold used to determine the area was 30% of the colour bar code. The dark contour contains the area of low conductivity which is a circle shape. Therefore the area could easily be calculated using the formula that applied to a circle.

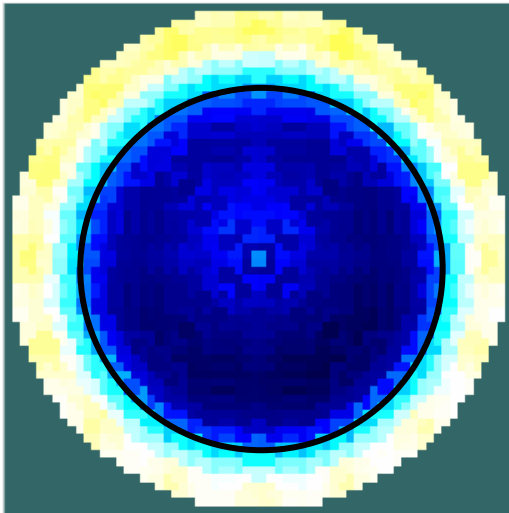


Figure 3.24 An example of the calculation of the area of low conductivity.

3.7 Development of a User-friendly GUI for ERT Post-data Analysis

GUI, which stands for graphical user interface, is a graphical display containing controls in one or more windows. It allows the user to execute interactive tasks without having to create a script or type commands. In order to run the algorithm comparison, the users of a GUI do not need to understand the details of how the tasks are performed or the complexity of the code. A MATLAB GUI responds to each user action whenever an end user manipulates a control or whenever user-operated components are activated. The GUI uses callback functions that can be used to perform specific operation when the user clicks or manipulates the components with keystrokes.

The idea behind the creation of a user friendly GUI for algorithm comparison is to enable a user, with no practical knowledge in programming, to use different algorithms in EIDORS and perform image reconstruction. It was made in a way that, the user can easily compare four

EIDORS algorithms and at the same time be able to modify the hyper-parameter value, or select different mesh size.

Figure 3.25 shows the front panel of the GUI created using MATLAB software for the algorithms comparison. The algorithm comparison GUI was designed in four different sections/panels: load data, input parameters, algorithm selection and running time.

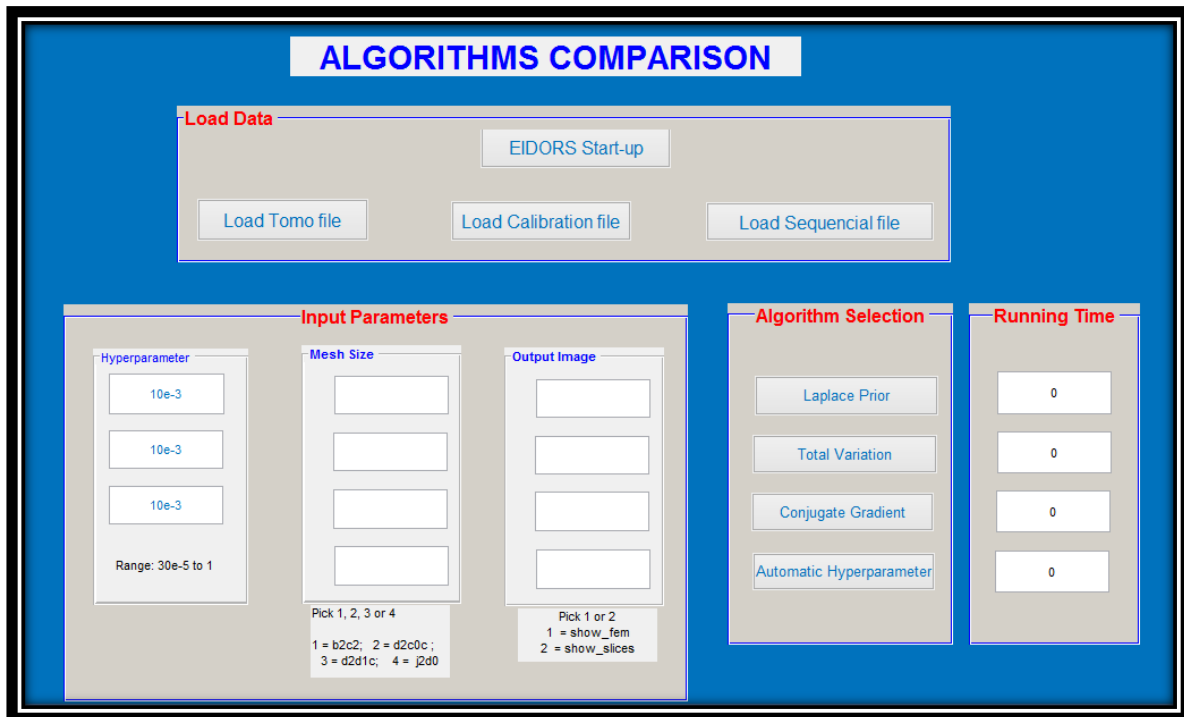


Figure 3.25 Image of the GUI created using MATLAB software.

a. Load Data

This panel allowed the user to efficiently load the data that will be used for the reconstruction. The GUI started with the start-up EIDORS, which ran all the functions that would be used in EIDORS. Depending on the specifications used during the experiments, the user had the possibility to load the data by simply clicking onto the “Load Data” push button. Similarly the calibration file and the sequence file needed for the reconstruction could be loaded into the programme by clicking onto the “Load Calibration file” and “Load Sequential file” pushbuttons. Once the data has been loaded into the programme it was immediately stored in the memory. This allowed the user to re-use the same data when needed without having to reload data every time.

b. The Input parameters

The input parameter section allowed the user to enter and change specific inputs before the reconstruction. The user could easily change the hyperparameter value for each reconstruction, as well as the mesh size and the output images. For the mesh size there were three options to choose from: the b2c2 option for less finer mesh, the d2d1c option for a finer mesh and the j2c0 option for a dense mesh. The output image had two options: the show_fem to display a reconstructed image with mesh or the show_slices which displays images with no mesh.

c. The Algorithm selection panel

The algorithm selection section offered the option of selecting between four different algorithms. The user can easily reconstruct images by clicking on the algorithm selection pushbutton, once the input parameters have been entered.

d. Running time

The running time panel provided the user with the opportunity to view the time taken by each algorithm to run and therefore the user could make a comparison based on the speed of each algorithm (See Figure 3.26).

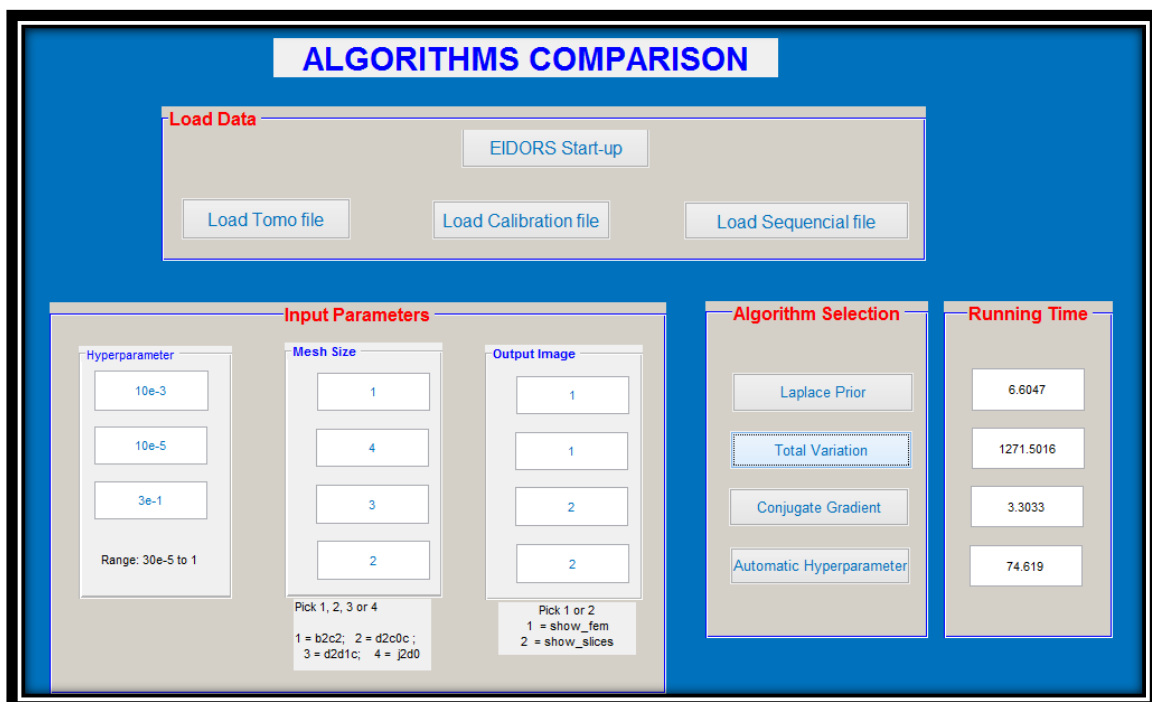


Figure 3.26 Example of image comparison using the GUI.

Figure 3.27 shows results obtained using the GUI programme.

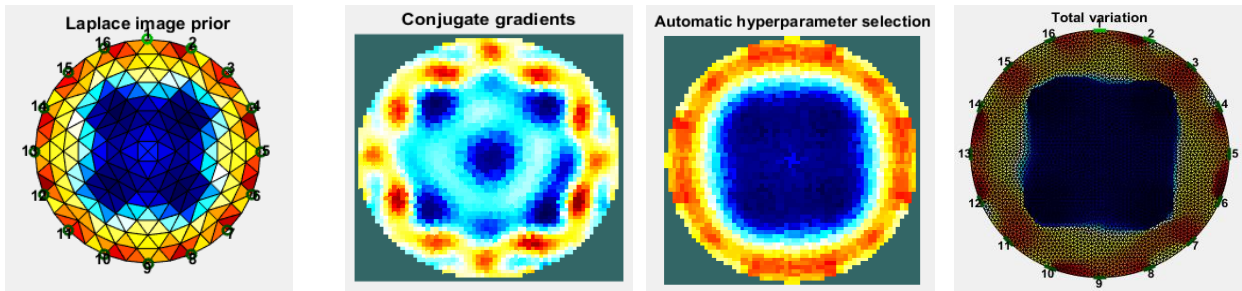


Figure 3.27 Results of reconstructed images from the GUI.

3.8 Summary

This chapter discusses the apparatus used and research methodology followed. Previous works regarding reconstructions algorithms were discussed and it was decided to compare the following algorithms: the Laplace Prior, the Total Variation, the Conjugate Gradient, the AHPS and One-step algorithms.

Different tests were conducted in a 4.26cm diameter pipe with saline water. For the algorithm comparison, three experimental setups were put in place: the static test where objects were placed inside the pipe, the level bed test where beads were mixed with water to form three different bed levels and finally the flow loop test where data was collected at four different flow rates. The data from these configurations were saved over 2 minutes, using a 2.5mA current injection.

The EIDORS software together with MATLAB was implemented for the off-line image reconstruction. A calibration procedure was discussed and data obtained using this procedure were used together with data collected from experiments in order to conduct the image reconstructions type “difference”.

The algorithm comparison was done based on three criteria namely: the image quality, the accuracy of the reconstruction and the running (computational) time. Depending on how good or bad the results of the reconstruction were, scores from 1 to 3 were allocated to the each

reconstructed images. Furthermore, the accuracy was calculated based on the percentage error given by the calculated area of low conductivity of each reconstructed images. This was done for the shape tests, static level bed tests and the flow loop tests.

A GUI was designed using MATLAB to enable an inexperienced user to perform the comparison of the four selected EIDORS algorithms. The GUI gives the option to change variables such as the hyperparameter value. It also allows the user the option of choosing different type of meshes as well as choosing how to display the reconstructed image.

Chapter 4 RESULTS AND DISCUSSION

In this chapter, the performances of five 2D reconstruction algorithms in different experimental setups are examined. Four of these algorithms are based on EIDORS, while the fifth algorithm was developed by the University of Cape Town (UCT), which is referred to as the “One-step algorithm” in this work (Long, 2005). These performances are examined from three different perspectives: firstly, the time taken by each algorithm to produce results, secondly, the quality of each reconstructed image and thirdly, the accuracy of each algorithm. The algorithms based on EIDORS that were selected for the comparison are: Gauss-Newton (GN) algorithm with Laplace prior, Gauss-Newton (GN) algorithm with Gaussian High Pass Filter image prior (referred to as the Automatic Hyperparameter Selection (AHPS) algorithm), the Total Variation (TV) algorithm and the Conjugate Gradient (CG) algorithm. The fifth algorithm was the One-step algorithm. A 1024 elements mesh was used for all the four EIDORS algorithms, while the One-step algorithm only used 384 elements mesh. The region of low conductivity, which indicated the location of the solid, was represented by the area of dark blue. The results of each experimental test were obtained using measurement data captured over two minutes. The average of this data was then used to reproduce the results (in the form of a tomogram).

4.1 Shape Test Experiment

Figure 4.1 shows the configuration of all the shapes used for this experiment.

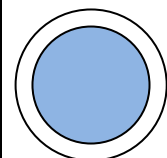
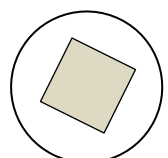
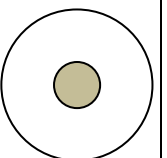
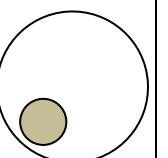
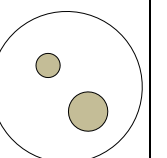
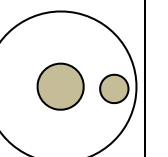
	A	B	c	D	E	F
Configurations						

Figure 4.1 Configuration of different objects used in the shape experiment.

In order to obtain qualitative reconstructed images, different hyperparameter values were used for the shape test experiment. For each experiment, the hyperparameter varied from 0.0001 to 1 and it was specified on each reconstructed figure.

4.1.1 Image reconstruction of Configuration A

Figure 4.2 show the results obtained from a 3.3 cm PVC pipe (actual area 8.55cm²) placed inside the measuring pipe section. The results obtained showed a distinguishable round shape of the object as expected.

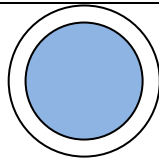
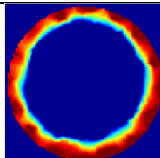
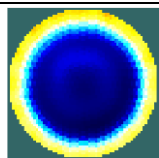
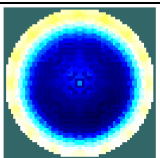
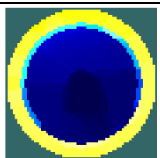
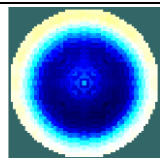
Configurations	One-step HP = 0.01	Laplace Prior HP = 0.03	AHPS	Total Variation HP = 0.0003	Conjugate Gradient HP = 0.03
A 					

Figure 4.2 Reconstructed image comparison for measurement configuration A - 3.3cm PVC pipe.

Table 4.1 shows the estimated values for the area of the reconstructed images, the image quality as well as computational time. For more information on the algorithm comparison criteria please refer to Chapter 3, Section 3.7.

Table 4.1 Algorithm performance comparisons for measurement configuration A - 3.3 PVC pipe

	Comparison Criteria			
	Size(cm ²)	Accuracy PE (%)	Image Quality (-)	Computational Time (s)
One-step	8.043	5.9	3	18.40
Laplace Prior	8.043	5.9	3	3.67
AHPS	7.548	11.7	3	66.41
Total Variation	8.814	3.1	3	9.17
Conjugate gradient	8.043	5.9	3	2.99

The percentages of error for the reconstructed algorithms varied from 3.1% to 11.7%. The Total Variation algorithm produced the lowest percentage error while the AHPS algorithm produced the highest percentage error for a difference in measurement of 1.002cm² from the actual area of the object. Although the Conjugate Gradient algorithm did not produce the most accurate result, it was the fastest algorithm of all five with a computational time of 2.99s, followed by the Laplace Prior algorithm (3.67s) and the Total Variation algorithm (9.17s), while the One-step algorithm and the AHPS algorithm were the slowest algorithms with 18.40s and 66.41s respectively.

4.1.2 Image reconstruction of Configuration B

Figure 4.3 shows the results obtained using a 2x2cm square wood piece (actual area: 4cm²) submerged inside the test pipe. The results obtained show a distinguishable square shape for all five algorithms.

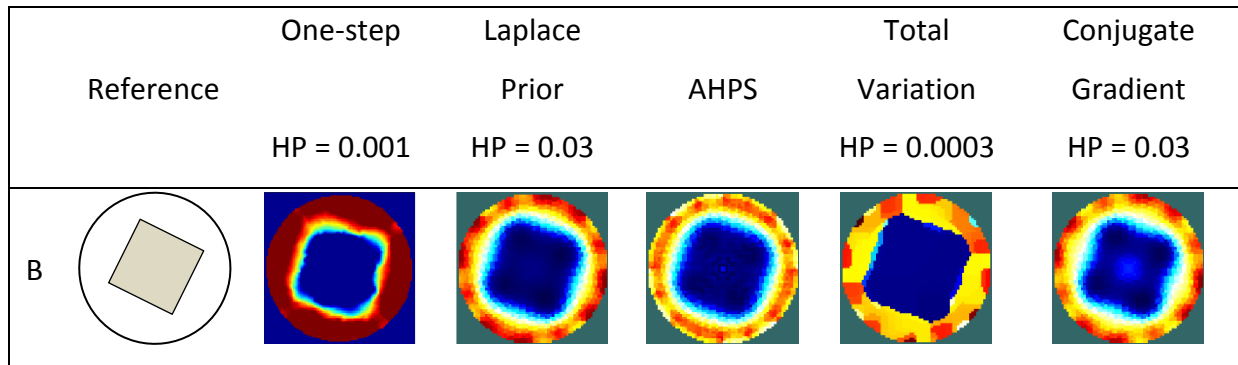


Figure 4.3 Reconstructed image comparison for measurement configuration B - 2x2cm square wood piece.

Table 4.2 summarises the performance of each reconstruction algorithm for measurement configuration B. The Laplace Prior, the AHPS, the Total Variation and the Conjugate Gradient algorithms produced reconstructed images bigger than the actual size of the object that was used for the experiment, while the One-step algorithm reproduced a shape closer to the actual size. This time the algorithms with the highest percentage error were: Total Variation (56.3%), follow by the Conjugate Gradient algorithm (52.3%), the Laplace prior (50.0%) and the AHPS algorithm (50.0%). For this particular experiment, the One-step algorithm had the lowest percentage error of 20.4%. For each of these algorithms, the difference in measurement of the area of conductivity was: 0.816cm² for the One-step, 2cm² for the Laplace and the AHPS, 2.25cm² for the Total Variation and 2.091cm² for the Conjugate Gradient. Although the One-step algorithm produced the lowest percentage error, the Total Variation in the other hand produced a better image quality with a sharper shape compare to the other algorithms. Overall, all the reconstructed algorithms overestimated the actual area of the measuring object. The algorithm with the fastest time once again was the Conjugate Gradient while the algorithm with the slowest time was the AHPS algorithm.

Table 4.2 Algorithm performance comparison for measurement configuration B - 2x2cm square wood piece

	Size(cm ²)	Comparison Criteria		
		Accuracy PE (%)	Image Quality	Computational Time (s)
One-step	4.816	20.4	3	18.38
Laplace Prior	6.00	50.0	2.5	3.55
AHPS	6.00	50.0	2.5	65.56
Total Variation	6.250	56.3	3	8.69
Conjugate gradient	6.091	52.3	2.5	2.83

4.1.3 Image reconstruction of Configuration C

Figure 4.4 displays the results obtained from a 1.3 cm round wood stick placed at the centre of the pipe (actual area: 1.327cm²). A round shape is visible when looking at each tomogram. The size of the conductivity area is very disproportionate when observing the result obtained using the AHPS algorithm.

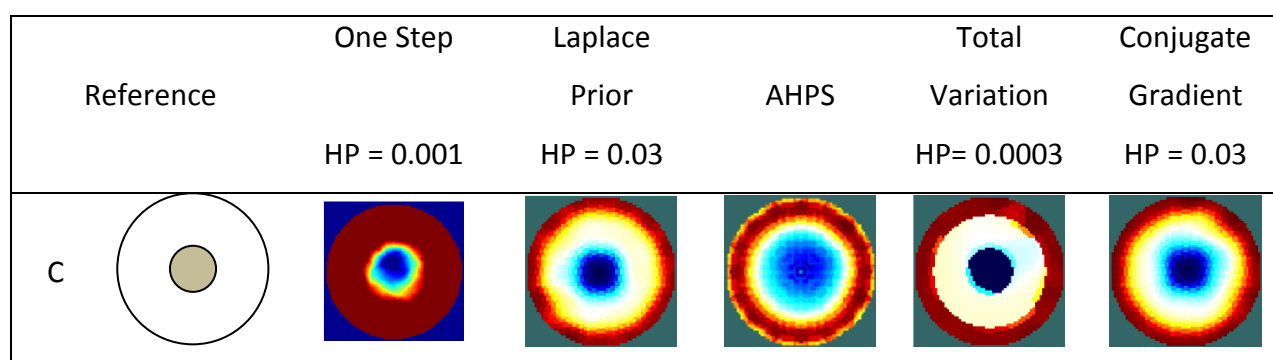


Figure 4.4 Reconstructed image comparison for measurement configuration C – 1.3 cm rod wood place at the centre of the experimental pipe.

Based on the results showed in Table 4.3, the AHPS algorithm produced the highest percentage error of 51.54%, followed by the Laplace Prior (6.48%) and the Conjugate Gradient (6.3%). The Total Variation and the One-step produced the closest reconstructed images with a percentage error of 1.6% and 3.01% respectively. Looking at the quality of the reconstructed images, the Total Variation algorithm produced a more qualitative image (sharper shape) compared to the other algorithms.

The difference in measurement of the area of low conductivity for each of these algorithms is: 0.04cm² (One-step), 0.086cm² (Laplace Prior), 0.684 cm² (AHPS algorithm), 0.021cm² (Total Variation) and 0.083cm² (Conjugate Gradient) respectively.

The computational times clearly shows that the Conjugate Gradient algorithm is the fastest, followed by the Laplace Prior algorithm and the Total Variation algorithm. The AHPS algorithm and the One-step algorithm, however, were the slowest.

Table 4.3 Algorithm performance comparison for measurement configuration C – 1.3cm rod wood placed at the centre of the experimental pipe

	Comparison Criteria			
	Size(cm ²)	Accuracy PE (%)	Image quality	Computational time (s)
One-step	1.287	3.01	3	18.75
Laplace Prior	1.413	6.48	3	3.53
AHPS	2.011	51.54	2	65.42
Total Variation	1.348	1.6	3	8.48
Conjugate Gradient	1.410	6.3	3	2.84

4.1.4 Image reconstruction of Configuration D

Figure 4.5 displays the results obtained using a 1.3cm round wood stick (actual area: 1.327cm²) placed on the side of the pipe test.

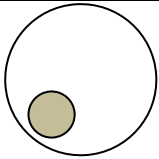
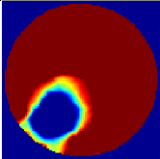
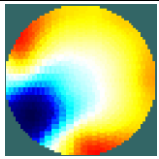
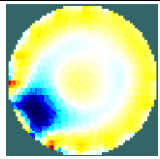

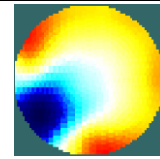
	Reference	One-step HP = 0.001	Laplace Prior HP = 1	AHPS	Total Variation HP = 0.05	Conjugate Gradient HP = 1
D						

Figure 4.5 Reconstructed image comparison for measurement configuration D – 1.3 cm rod wood place on the side of the experimental pipe.

For the Laplace Prior, the AHPS, the Total Variation and the Conjugate Gradient algorithms, the reconstructed images did not display a round shape as expected. Instead, the images display a sort of trapeze or square shape. However, the area of impurity displayed in each one of them gave a value close to the area of the objet used for the reconstruction. The One-step algorithm however produced a shape very closed to the one used for the experiment.

As shown in Table 4.4, the percentages errors varied between 8.21% and 26.6%. The lowest percentage is given by the Total Variation with a value of 8.21%, followed by the One-step algorithm with 12.74%, the AHPS algorithm with 11.23% and finally the Laplace prior algorithm and the Conjugate Gradient algorithm with 26.6% each. The difference between the calculated and true area for each of these algorithms was: 0.169cm² for the One-step algorithm, 0.353cm² for the Laplace Prior and Conjugate Gradient algorithms, 0.149cm² for the AHPS algorithm and 0.109cm² for the Total Variation algorithm respectively.

The Conjugate Gradient algorithm produced the fastest reconstructed image with a computational time of 2.89s, followed by the Laplace prior (3.58s), the Total Variation (8.60s), the One-step algorithm (18.20s) and the AHPS algorithm (65.81s).

Table 4.4 Algorithm performance comparison for measurement configuration D – 1.3cm rod wood placed on the side of the experimental pipe

	Size(cm ²)	Comparison Criteria		
		Accuracy PE (%)	Image quality	Computational time (s)
One-step	1.496	12.74	3	18.20
Laplace Prior	1.680	26.6	2	3.58
AHPS	1.476	11.23	2	65.81
Total Variation	1.436	8.21	2	8.60
Conjugate gradient	1.680	26.6	2	2.89

4.1.5 Image reconstruction of Configuration E

Figure 4.6 displays the results obtained using a 1.3cm and 0.9cm diameter round wood sticks (actual areas: 1.327cm² and 0.636cm²) placed close to the edge of the experimental pipe section.

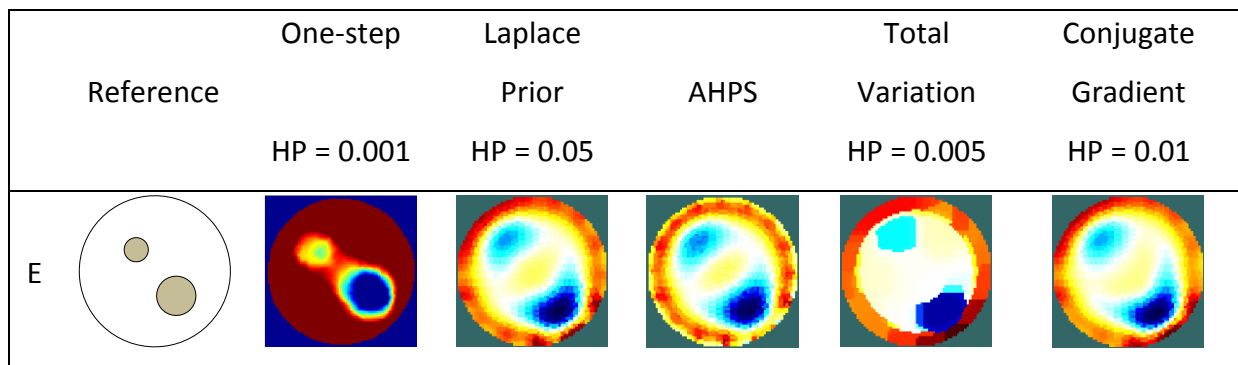


Figure 4.6 Reconstructed image comparison for measurement configuration E – 1.3cm and 0.9cm rod woods placed close to the side of the experimental pipe.

Based on the results obtained, only the One-step algorithm was able to produce the expected round shapes which are representative of the experimental setup. The other four algorithms

showed images that display a trapeze shape for the 1.3cm rod wood and a semi-circle shape for the 0.9cm round wood stick.

The performance of each algorithm is shown in Table 4.5.

Table 4.5 Algorithm performance comparison for measurement configuration E – 1.3cm rod wood placed at the centre and 0.9cm placed close to the edge of the experimental pipe

	Size(cm ²)	Comparison Criteria		
		Accuracy PE (%)	Image quality	Computational time (s)
One-step	1.713	12.74	3	18.17
Laplace Prior	2.305	17.42	2	3.57
AHPS	2.395	22.00	2	66.75
Total Variation	2.103	7.13	2.5	8.49
Conjugate gradient	2.091	6.52	2	2.86

Based on the results obtained, the percentage error for the combined shape varied between 6.52% and 22%, with the Conjugate Gradient algorithm having the lowest percentage and AHSP algorithm having the highest percentage. The One-step algorithm produced a percentage error of 12.74%; the Laplace Prior algorithm produced a percentage error of 17.42%, while the AHPS algorithm produced a percentage error of 22%.

The Conjugate Gradient was the fastest algorithm followed by the Laplace Prior, the Total Variation, the One-step algorithm and the AHPS algorithm.

4.1.6 Image reconstruction of Configuration F

The results obtained from a 1.3cm and 0.9cm round (actual areas: 1.327cm² and 0.636 cm²) wood stick placed close to the centre of the pipe test section are displayed on Figure 4.7.

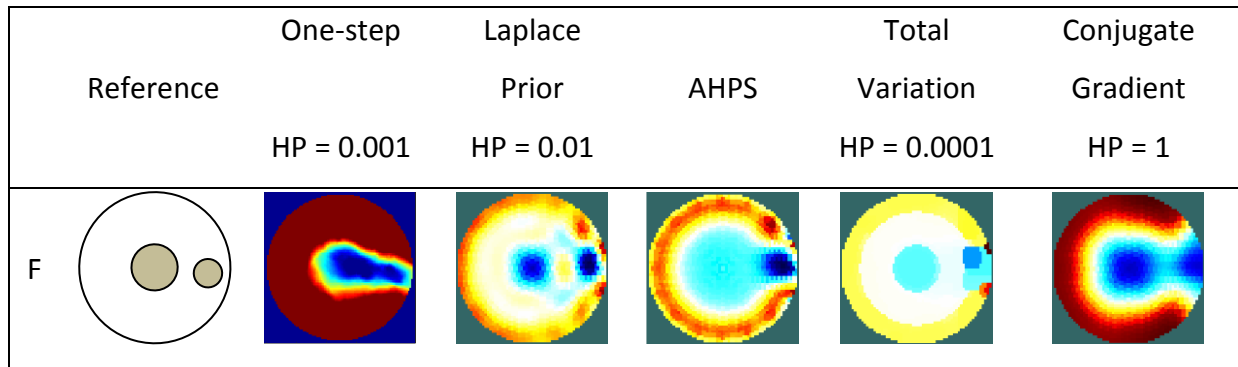


Figure 4.7 Plot of the reconstructed image of the inverse problem for the 1.3cm and 0.9cm rod woods placed at the centre and closed to the edge of the pipe.

The reconstructed images showed a distinctive round shape in the centre of the pipe for the Laplace Prior, the Total Variation and the Conjugate Gradient algorithm. For the object placed on the side of the experimental pipe, the shapes do not appear round for most of the algorithms. The One-step algorithm and AHPS algorithm showed an object which is the combination of the two objects.

Table 4.6 indicates high percentage errors for the AHPS algorithm and the Conjugate Gradient with the value of 133.67% and 40.96% respectively. The lowest percentages occurred on the One-step algorithm, the Total variation and the Laplace Prior with the value of 9.78%, 22.41% and 22.77% respectively. The computational time clearly indicated that the Conjugate Gradient produced the fastest time of 3.19s, followed by the Laplace Prior (3.91s), the Total Variation (8.97s) and the One-step algorithm (18.44s). The AHPS algorithm on the other hand had the slowest computational time of 69.34s.

Table 4.6 Algorithm performance comparison for measurement configuration F – 1.3cm and 0.9cm rod wood placed close to the edges of the experimental pipe

	Comparison Criteria			
	Size(cm ²) 1.3cm & 0.9cm	Accuracy PE (%)	Image quality	Computational time (s)
One-step	1.771	9.78	1.5	18.44
Laplace Prior	1.516	22.77	1.5	3.91
AHPS	4.587	133.67	1.5	69.34
Total Variation	1.523	22.41	2	8.97
Conjugate gradient	2.767	40.96	2	3.19

4.1.7 Summary of experimental shape results

Figure 4.8 juxtaposes the region of low conductivity of the reconstructed images with the actual region of the object in the measurement pipe section.

The reconstructed images shown in Figure 4.8 indicate that the One-step algorithm produced good quality images which reflected in most cases the object used during the experiment. On the other hand, the Total variation produced a sharper shape compared to the other three EIDORS algorithm reconstructions.

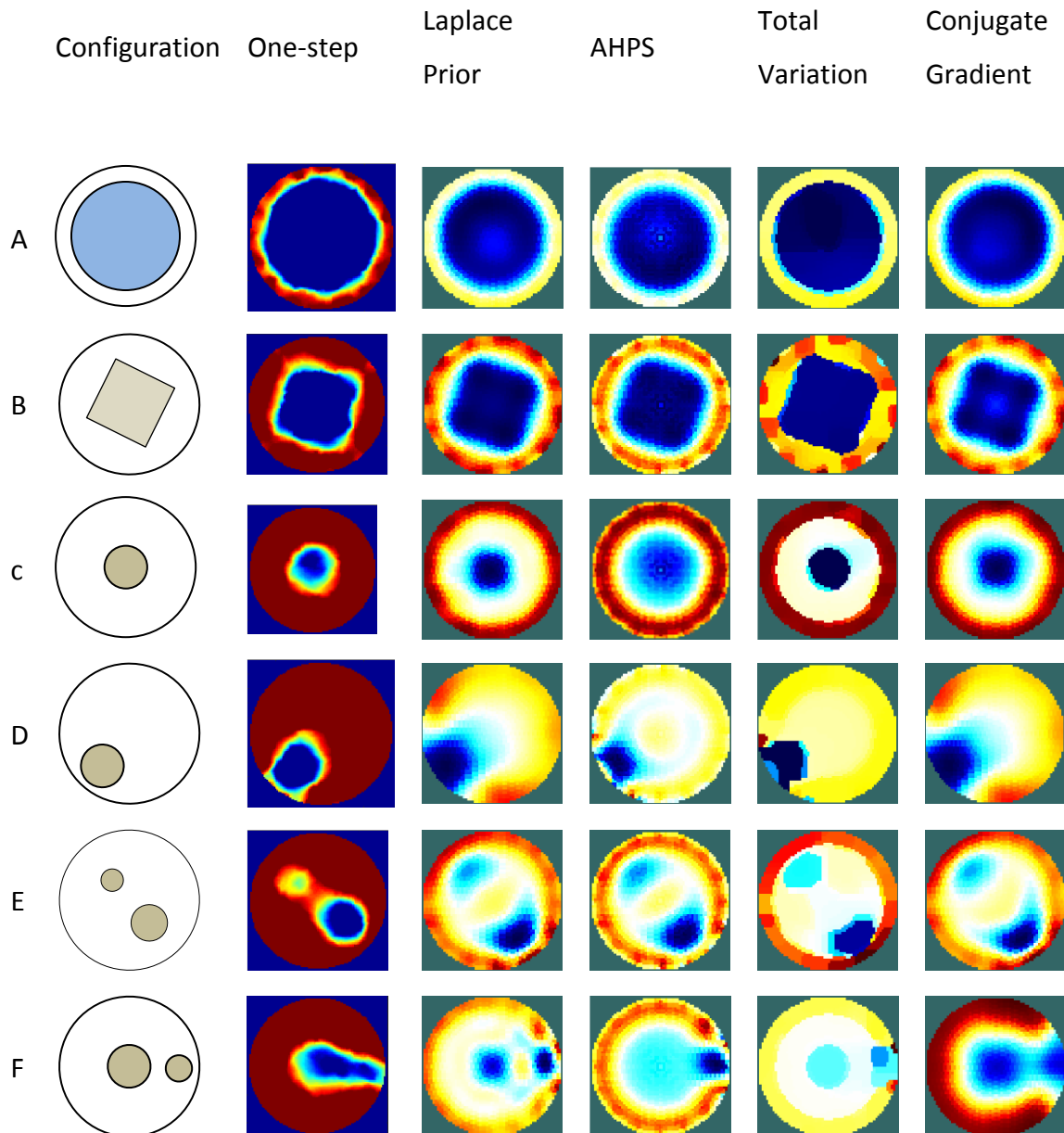


Figure 4.8 Summary of image reconstruction comparison for measurement configuration A-F

The hyperparameter values used for the image reconstructions are shown in Table 4.7. The One-step algorithm is the only algorithm with a constant hyperparameter value. For the other three algorithms (Laplace Prior, Total Variation and the Conjugate Gradient), the hyperparameter value increased for shapes placed close to the edge of the pipe.

Table 4.7 Summary of Hyperparameter values for the shape test experiments (A – F)

Configurations	One step	Laplace Prior	Total Variation	Conjugate Gradient
A	0.001	0.03	0.0003	0.03
B	0.001	0.03	0.0003	0.03
C	0.001	0.03	0.0003	0.03
D	0.001	0.03	0.05	1
E	0.001	0.03	0.005	0.01
F	0.001	0.03	0.0001	1

When looking at the average value of the percentage difference (obtained from area of the shapes) in Table 4.8, it is clear that the One step, the Total variation, the Laplace Prior and the Conjugate Gradient algorithms were more accurate with average values 10.76%, of 16.46%, 21.53% and 23.10% respectively. The AHPS algorithm produced an average value of 46.69%.

Based on the results obtained, it can clearly be concluded that the One-step algorithm and the Total variation algorithm demonstrated the best performance for these types of experiments. Compare to the other four algorithms, the AHPS algorithm is clearly not suitable for the reconstruction of shapes or objects.

Table 4.8 Average percentage difference error for each algorithm for the shape test experiments (A – F)

Configurations	PE (OS)	PE (LP)	PE (AHPS)	PE (TV)	PE (CG)
A	5.9	5.9	11.7	3.1	5.9
B	20.4	50.0	50.0	56.3	52.3
C	3.01	6.48	51.54	1.6	6.3
D	12.74	26.6	11.23	8.21	26.6
E	12.74	17.42	22.00	7.13	6.52
F	9.78	22.77	133.67	22.41	40.96
Average	10.8	21.5	46.7	16.5	23.1

The computational time of all five algorithms is shown in Table 4.9. Based on the average value obtained, the Conjugate Gradient algorithm is the fastest of all five algorithms, while the AHPS algorithm is the slowest of all five algorithms.

Table 4.9 Average computational time (in seconds) of each algorithm for the shape test experiments (A – F)

Configurations	CT (OS)	CT(LP)	CT (AHPS)	CT (TV)	CT (CG)
A	18.40	3.67	66.41	9.17	2.99
B	18.38	3.55	65.56	8.69	2.83
C	18.75	3.53	65.42	8.48	2.84
D	18.20	3.58	65.81	8.60	2.89
E	18.17	3.57	66.75	8.49	2.86
F	18.44	3.91	69.34	8.97	3.19
Average	18.39	3.63	66.55	8.73	2.93

The image quality (IQ) averages obtained in Table 4.10 showed that the One Step algorithm produced the best image quality, followed by the Total Variation, the Laplace Prior algorithm and the Conjugate Gradient. The AHPS algorithm was clearly the least satisfactory.

Table 4.10 Image Quality of each configuration (A – F)

Configurations	IQ (OS)	IQ(LP)	IQ (AHPS)	IQ (TV)	IQ (CG)
A	3	3	3	3	3
B	3	2.5	2.5	3	2.5
C	3	3	2	3	3
D	3	2	2	2	2
E	3	2	2	2.5	2
F	1.5	1.5	1.5	2	2
Average	2.75	2.3	2.2	2.6	2.4

Based on the accuracy, the computational time as well as the quality of the images, the Total Variation was the best algorithm of all five.

4.2 Level Bed Analysis

The pictures of the different level bed heights are shown in Figure 4.9. The true height of the static bed levels was measured using a ruler and visual inspection. This was then compared to the bed level height determined from the low conductivity region of the various tomograms. See Chapter 3, Section 3.3.2 for more detail about the experimental setup and methodology.

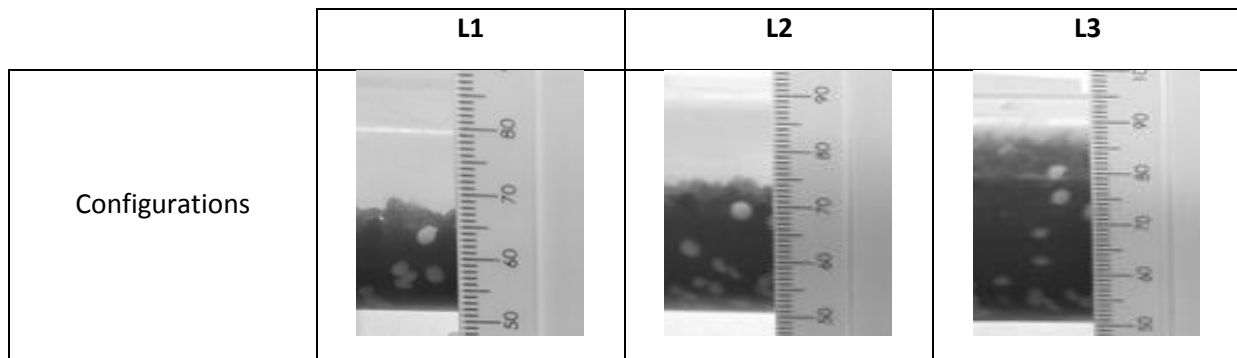


Figure 4.9 Configuration of different level bed heights used in the static level bed experiment

Contrary to the shape test experiment, the level bed experiment used the same hyperparameter value of 1 for all three level bed experiments. Using a heuristic approach, this value was found to be the highest value that could be used in order to obtain the best quality image without any distortion of the images.

4.2.1 Image Reconstruction of Configuration L1

Figure 4.10 shows the results obtained from reconstruction of the first level bed (actual height 1.5cm). On the left hand side, photos of the experimental condition are shown.

Based on visual analysis, the low conductivity at the bottom of the pipe clearly indicates the formation of a level bed.

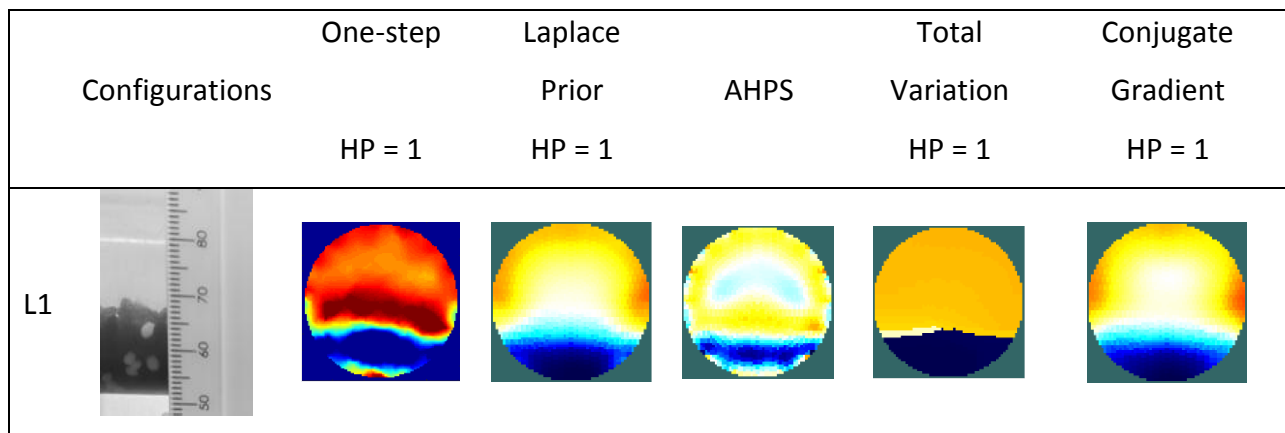


Figure 4.10 Image reconstruction comparison for measurement configuration L1 (static level bed test)

Table 4.11 illustrates the estimated values of the height of the level bed and the area of low conductivity for the reconstructed images obtained using the different algorithms.

The height of the level bed in all five reconstructed images varied from 1.02cm to 1.25cm. The difference in heights obtained from each reconstructed image, when compares to the actual height, are: 0.06cm, 0.2cm, 0.4cm, 0.15cm and 0.3cm for the One-step algorithm, the Total Variation algorithm, the AHPS algorithm, the Total Variation algorithm and the Conjugate Gradient algorithm respectively.

These values indicate that the reconstructed images obtained from all five algorithms are not far from the actual height of the level bed.

Table 4.11 Algorithm performance comparison for measurement configuration L1 – level bed 1.5 cm

	Comparison Criteria			
	Height Size(cm)	Accuracy PE (%)	Image quality	Computational time (s)
One-step algorithm	1.56	4.0	3	18.03
Laplace Prior	1.3	13.3	3	4.09
AHPS algorithm	1.1	26.7	2	66.03
Total Variation	1.35	10.0	3	8.89
Conjugate gradient	1.2	20.0	3	3.05

The percentage error varied from 4.0% to 26.7%. The results clearly show that the One-step algorithm (4%) and the Total Variation algorithm (10%) produced the least percentage errors follow by the Laplace Prior algorithm (13.3%) and the Conjugate Gradient algorithm (20%).

On the other hand, the AHPS algorithm gave the highest percentage error with the slowest computational time of 66.03s.

4.2.2 Image Reconstruction of Configuration L2

The results of the reconstructed images of the second level bed (actual Height 2.2cm) obtained from the selected algorithms are shown in Figure 4.11.

The visual analyses of the images clearly show the area of low conductivity at the bottom edge of the pipe on each reconstructed image. However, when moving toward the centre of the pipe, the region of low conductivity decreases when observing the result obtained using the AHPS algorithm.

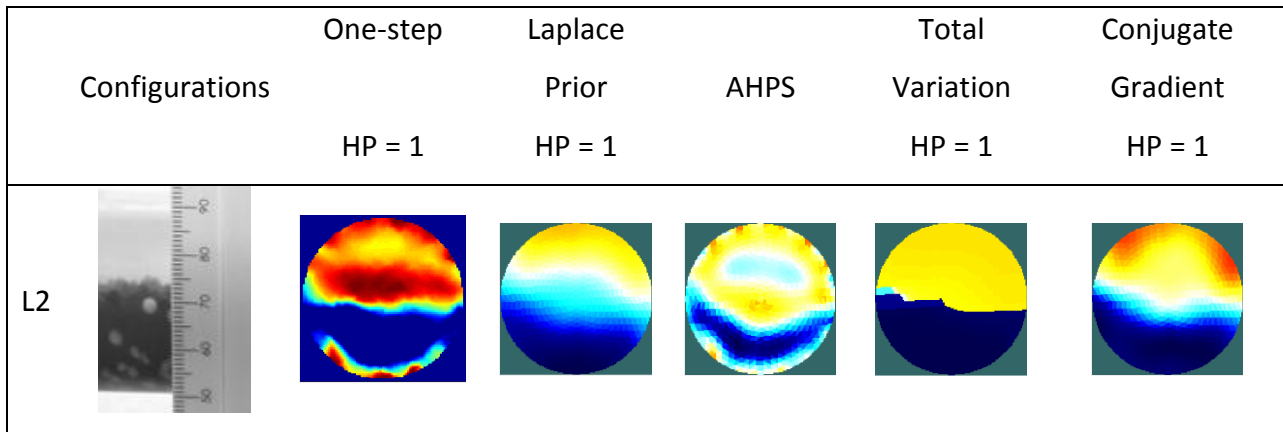


Figure 4.11 Image reconstruction comparison for measurement configuration L2 (static level bed test)

The results of the measurement of the heights of the bed and the calculation of the percentage difference error obtained from the reconstructed images are presented in Table 5.12.

All the measurements of the level bed height were made on the edge of the low conductivity region. The measurements varied from 1.86cm to 2.02cm. The differences in measurement are: 0.2cm, 0.19cm, 0.34cm, 0.18cm and 0.19cm for the One-step algorithm, the Laplace Prior algorithm, the AHPS algorithm, the Total Variation algorithm and the Conjugate Gradient algorithm respectively.

Table 4.12 Algorithm performance comparison for measurement configuration L1 – level bed 2.2 cm

	Comparison Criteria			
	Height (cm)	Accuracy PE (%)	Image quality	Computational time (s)
One-step	2	9.1	3	18.97
Laplace Prior	2.01	8.7	3	3.75
AHPS	1.86	15.5	2	65.72
Total Variation	2.02	8.2	3	8.62
Conjugate gradient	2.01	8.7	3	2.99

The lowest percentage was obtained from the Total Variation algorithm (8.2%), followed by the Laplace Prior and Conjugate Gradient (8.7%) and the One-step algorithm (9.1%). The AHPS algorithm had the highest percentage error (15.5%). The computational time of each algorithm varied from 2.99s to 65.72s, with Conjugate Gradient algorithm the fastest and the AHPS algorithm the slowest.

4.2.3 Image Reconstruction of Configuration L3

Figure 4.12 shows the results of the reconstructed images of the third level bed (actual Height 3.4cm) configuration.

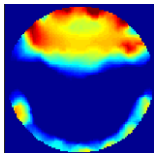
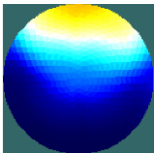
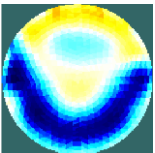

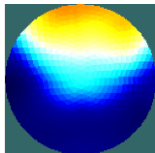
Configurations	One-step HP = 1	Laplace Prior HP = 1	AHPS	Total Variation HP = 1	Conjugate Gradient HP = 1
L3					

Figure 4.12 Image reconstruction comparison for measurement configuration L3 (static level bed test).

As the level bed increases in height, the area of low conductivity area decreased significantly toward the centre of the pipe in the case of the AHPS algorithm and the Conjugate Gradient algorithm. The One-step algorithm, the Laplace Prior algorithm and the Total Variation algorithm produced reconstructed images with level beds which were more representative of the actual pipe condition.

The area of low conductivity and the height of the level bed of the reconstructed images are illustrated in Table 4.13.

Table 4.13 shows the performance of the algorithms for this particular experiment. The measurements of the height of the level bed varied between 2.75cm and 3cm (actual height

3.4cm). The percentage of error varied from 11.8% to 19.2%. The One-step algorithm, the Laplace Prior and the Total Variation algorithms had the lowest percentage errors. The Conjugate Gradient and the AHPS algorithm produced the highest percentage errors.

Table 4.13 Algorithm performance comparison for measurement configuration L1 – level bed 3.4cm

	Comparison Criteria			
	Height Size(cm)	Accuracy PE (%)	Image quality	Computational time (s)
One-step	3	11.8	2.5	19.17
Laplace Prior	3	11.8	3	4.00
AHPS	2.75	19.2	1	65.91
Total Variation	2.95	13.2	3	8.62
Conjugate gradient	2.92	14.1	2.5	3.00

Based on the results of the computational time obtained, the fastest algorithm was the Conjugate Gradient algorithm (3.00s), followed by the Laplace Prior (4.00s), the Total Variation (8.62s), the One-step algorithm (19.17s) and the AHPS algorithm (65.91s).

4.2.4 Summary of experimental level bed results

Figure 4.13 shows the reconstructed images of the level beds (water and plastic beads) produced by the five image reconstruction algorithms. On the left hand side photos of the experimental condition are shown.

The computation of the accuracy of each algorithm based on the level bed height is shown in Table 4.14.

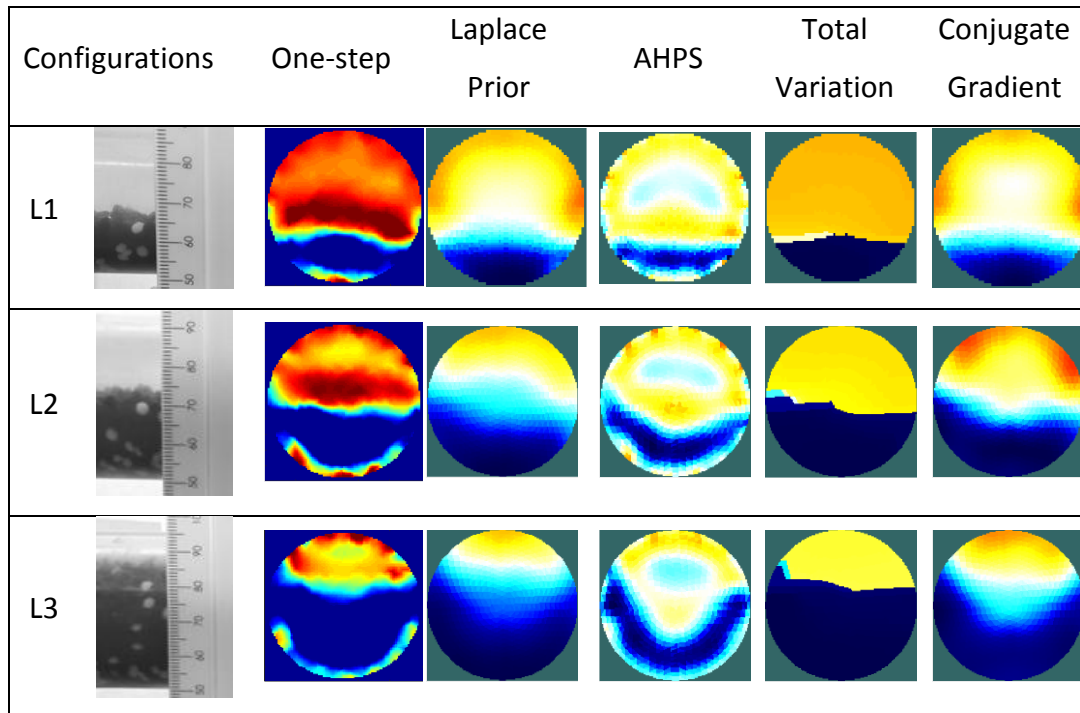


Figure 4.13 Summary of image reconstruction comparison for measurement configurations L1 – L3.

Based on the results obtained in Table 4.14, the One Step and the Total Variation algorithms yielded better results with an average of 14.9% and 15.2%, followed by the Laplace Prior algorithm with a value of 17.8%, the Conjugate Gradient algorithm with a value of 18.0% and finally the AHPS algorithm with a value of 22%.

Based on the quality of the images obtained from the AHPS algorithm, it is clear that the AHPS algorithm is not suitable for the level bed experiment.

Table 4.14 Average accuracy for each algorithm for the level bed experiments (L1 – L3)

Configurations	PE (OS)	PE (LP)	PE (AHPS)	PE (TV)	PE (CG)
L1	4.0	13.3	26.7	10.0	20.0
L2	9.1	8.7	15.5	8.2	8.7
L3	11.8	11.8	19.2	13.2	14.1
Average	8.3	11.3	20.5	10.5	14.3

The computational time of all three experiments are shown in Table 4.15. The Conjugate Gradient algorithm had the fastest reconstruction time while the AHPS algorithm had the slowest reconstruction time.

Table 4.15 Average computational time (in second) of each algorithm for the level bed experiments (L1 – L3)

Configurations	CT (OS)	CT(LP)	CT (AHPS)	CT (TV)	CT (CG)
L1	18.03	4.09	66.03	8.89	3.05
L2	18.97	3.76	65.72	8.62	2.99
L3	19.17	4.00	65.91	8.62	3.00
Average	18.72	3.95	65.89	8.71	3.01

Table 4.16 show the computation of the image quality scores. Based on the average obtained, the Laplace Prior and the Total Variation algorithms produce the best image quality, followed by the UCT and Conjugate Gradient algorithms. The AHPS gave the least satisfactory quality with an average score of 1.7.

Table 4.16 Average of the image quality (IQ) scores of each algorithm for the level bed (L1 – L3)

Configurations	IQ (OS)	IQ (LP)	IQ (AHPS)	IQ (TV)	IQ (CG)
L1	3	3	2	3	3
L2	3	3	2	3	3
L3	2.5	3	1	3	2.5
Average	2.8	3.0	1.7	3.0	2.8

Once again, the Total Variation algorithm was the best algorithm based on the accuracy, the computational time and the image quality.

4.3 Flow Loop Test Analysis

Figure 4.14 shows the pictures of the different flow rates used during this experiment.

Different flow rates were used in order to create different flow conditions: 0.68l/s, 1.86l/s, 2.84l/s and 4.76l/s. For the image reconstruction of all four flow rates, a hyperparameter value of 1 was used in all four of the algorithms (Laplace Prior, AHPS, Total variation and Conjugate Gradient) using a heuristic approach. The One-step algorithm used a hyperparameter of 0.001 for all four flow rates. Those values were found to be the highest value that could be used in order to obtain the best image quality. Two sets of flow loop experiments were conducted, but only one was presented in this thesis. The results obtained from the second experiment are presented in Appendix B. Similar results were obtained for both sets of flow loop experiments.

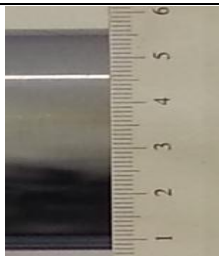
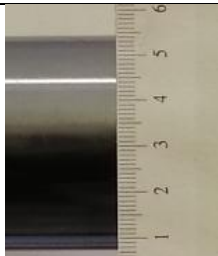
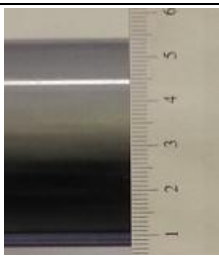

	A	B	C	D
	Flow rate: 0.68l/s Height: 1.7cm	Flow rate: 1.86l/s Height: 2.2cm	Flow rate: 2.84l/s Height: 1.9cm	Flow rate: 4.76l/s Height: 0cm
Configurations				

Figure 4.14 Configuration of different flow rates and level bed heights used in the flow loop experiment.

4.3.1 Image Reconstruction of flow loop experiment A (0.68l/s)

The results of the reconstruction of the level bed flowing at 0.68l/s are shown in Figure 4.15.

The flow condition at this speed was a moving bed at the bottom of the pipe flowing at a slower rate compared to the water.

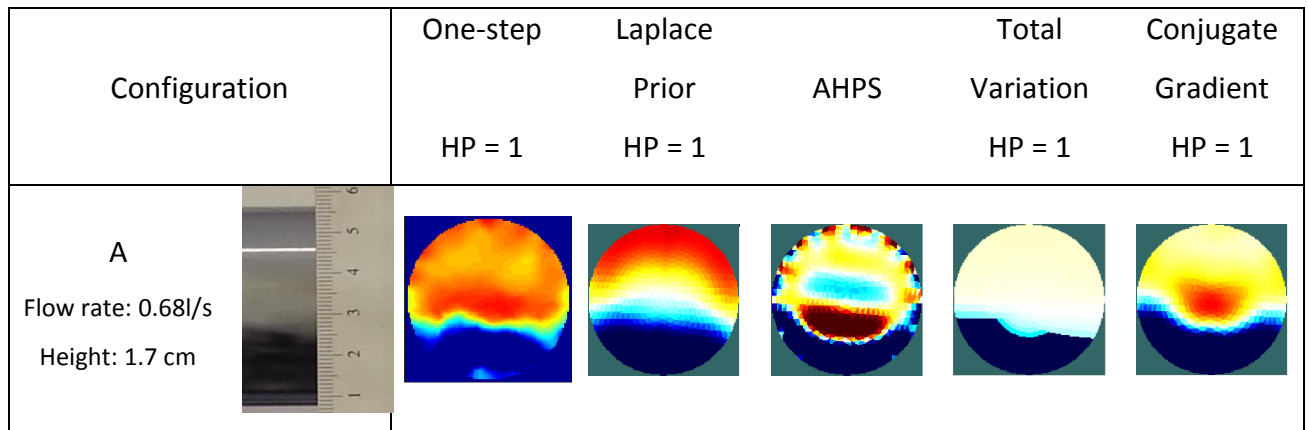


Figure 4.15 Image reconstruction comparisons for flow loop experiment A (0.86l/s).

The visual analysis of the results (tomogram) indicates the formation of a level bed at the bottom of the pipe, which was expected.

The measured height of the level beds for each algorithm together with the computational time and image quality score are presented in Table 4.17.

The heights of the level bed on the reconstructed images varied from 1.2cm to 1.63cm. The percentage errors calculated from these measurements varied from 4.1% to 29.4%, with the Laplace Prior having the lowest percentage error and the AHPS algorithm having the highest percentage error. The One-step algorithm and the Total Variation produced a percentage error of 11.8% and 17.7% respectively, while the Conjugate Gradient had a value of 5.9% with the fastest reconstruction time.

Table 4.17 Algorithm performance comparison for flow loop experiment A (0.86l/s)

	Comparison Criteria			
	Height Size(cm)	Accuracy PE (%)	Image quality	Computational time (s)
One-step	1.5	11.8	2.5	29.53
Laplace Prior	1.63	4.1	2.5	13.72
AHPS	1.2	29.4	1.5	70.13
Total Variation	1.4	17.7	2.5	18.81
Conjugate gradient	1.6	5.9	2.5	12.98

4.3.2 Image Reconstruction of the flow loop experiment B (1.3 l/s)

Figure 4.16 shows the results of the reconstruction of the level bed flowing at the rate of 1.3 litre per second (l/s).

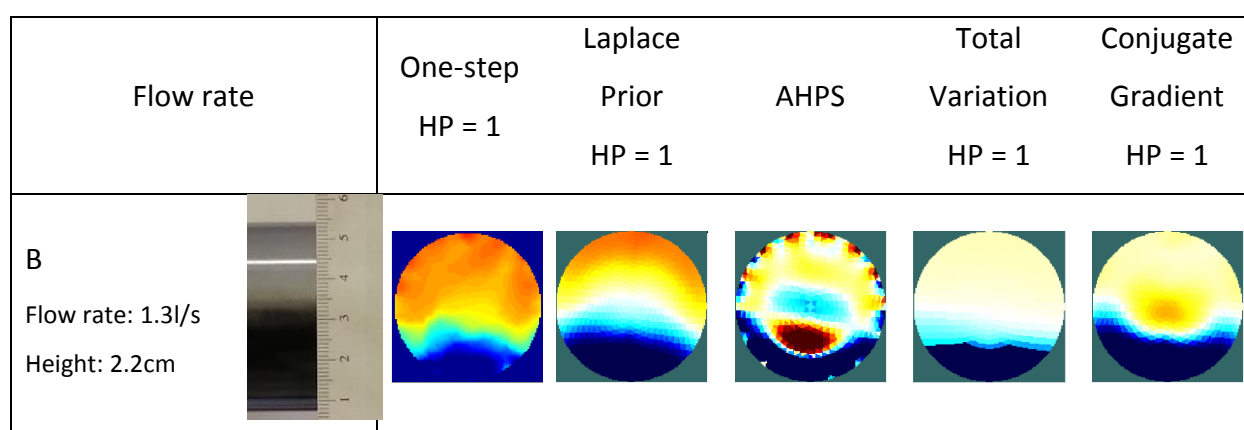


Figure 4.16 Image reconstruction comparisons for flow loop experiment B (1.3 l/s).

The flow condition in this experiment was partially suspended with a faster and more constant moving bed at the bottom of the pipe test. Due to the increase of the flow rate from 0.68 l/s to 1.3 l/s, the height of the level bed also increased from 1.5cm to 2.2cm.

Based on the reconstructed images obtained, there is evidence of a level bed at the bottom of the pipe for all five reconstruction algorithms.

The percentage accuracy, the image quality as well as the computational time are shown in Table 4.18.

Table 4.18 Algorithm performance comparison for flow loop experiment B (1.3l/s)

Reconstructed image	Height Size(cm)	Comparison Criteria		
		Accuracy PE (%)	Image quality	Computational time (s)
One-step	1.4	36.4	2.5	28.29
Laplace Prior	1.55	29.6	2.5	13.54
AHPS	1.1	50.0	1	78.69
Total Variation	1.2	45.5	2.5	18.51
Conjugate gradient	1.4	36.4	2.5	12.86

The percentage errors calculated from the measurements vary from 29.6% to 50.0%, with the Laplace Prior having the lowest value, followed by the Conjugate Gradient (36.4%), the One-step algorithm (36.4%), the Total Variation (45.5%) and the AHPS algorithm with the highest value. The slowest reconstruction time was obtained from the AHPS (78.69s), followed by the One-step algorithm (28.29s), the Total Variation (18.51s), Laplace Prior (13.54s), and the Conjugate Gradient (12.86s).

4.3.3 Image Reconstruction of the flow loop experiment C (2.82l/s)

The flow condition during this experiment was a suspended flow with a visible moving bed flowing almost at the same rate (2.82l/s) as the water.

The reconstructed images of the 2.82l/s flow loop experiment (C) are show in Figure 4.17.


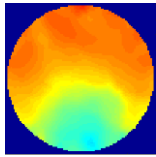
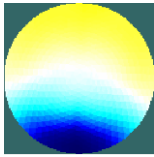
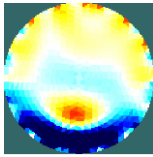

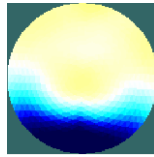
Configuration	One-step HP = 1	Laplace Prior HP = 1	AHPS	Total Variation HP = 1	Conjugate Gradient HP = 1
C Flow rate: 2.82l/s Height: 1.9cm 					

Figure 4.17 Image reconstruction comparisons for flow loop experiment C (2.82l/s).

Despite the fact that the particles were flowing at a high speed, the area of low conductivity, which is the characteristic of a level bed, was visible at the bottom of the pipe, except for the AHPS algorithm which presented a level bed smaller than anticipated.

As shown in Table 4.19, the calculations of the percentage errors varied between 15.8% and 52.6%. The lowest percentage in this case was obtained from the One-step algorithm and the highest percentage from the AHPS algorithm. The Laplace Prior had the next smallest percentage error of 34.2%, while the Total variation and the Conjugate Gradient both produced a percentage error of 33.7% and 34.2% respectively.

Table 4.19 Algorithm performance comparison for flow loop experiment C (2.82l/s)

	Comparison Criteria			
	Height Size(cm)	Accuracy PE (%)	Image quality	Computational time (s)
One-step	1.6	15.8	2.5	28.67
Laplace Prior	1.25	34.2	2.5	13.70
AHPS	0.9	52.6	1	79.57
Total Variation	1.26	33.7	2.5	18.77
Conjugate gradient	1.25	34.2	2.5	13.03

4.3.4 Image Reconstruction of the flow loop experiment D (4.5l/s)

Figure 4.8 shows the results obtained from the flow loop test at a flow rate of 4.5l/s. At this high flow rate, the flow condition was fully suspended with water and beads mixed together, with no visible level bed.

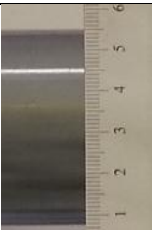
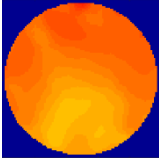

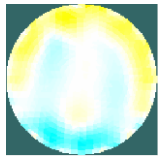


Flow rate	One-step HP = 1	Laplace Prior HP = 1	AHPS	Total Variation HP = 1	Conjugate Gradient HP = 1
<p>D</p> <p>Flow rate: 4.5l/s</p> <p>Height: 0cm</p> 					

Figure 4.18 Image reconstruction comparisons for flow loop experiment C (4.5l/s).

The level bed is not clearly visible on the reconstructed images obtained from all five algorithms. However, the reconstructed images indicated a different conductivity level (bright yellow and sky blue) at the bottom of the pipe, which is the indication of the presence of some particles inside the pipe.

Given the fact that the level bed was travelling at a high speed, with no visible level bed, the estimation of the heights of the bed was difficult to establish. Therefore it was decided not to include the accuracy (PE) calculation for this test. However, based on the photo and observed flow condition, an image quality score could still be given.

Table 4.20 presents the image quality score as well as the computational time.

Table 4.20 Algorithm performance comparison for flow loop experiment D (4.5l/s)

	Comparison Criteria		
	Accuracy PE (%)	Image quality	Computational time (s)
One-step	-	3	28.16
Laplace Prior	-	2.5	15.58
AHPS	-	2.5	83.35
Total Variation	-	3	20.77
Conjugate gradient	-	2.5	14.78

The One-step and the Total Variation algorithms had the highest score of 3, while the Laplace Prior, the Conjugate Gradient and the AHPS had the lowest score of 2.5.

The Conjugate Gradient algorithm was the fastest, followed by the Laplace Prior algorithm, the Total Variation algorithm, the One-step algorithm and the AHPS algorithm.

4.3.5 Summary of experimental flow loop results

Figure 4.19 displays the summary of results obtained from the dynamic flow loop experiments.


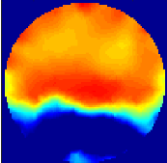
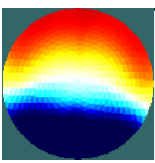
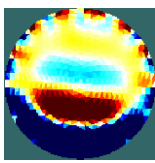

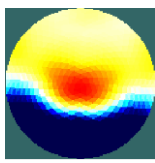

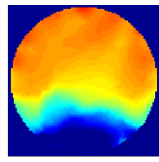
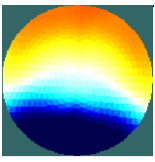
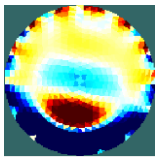

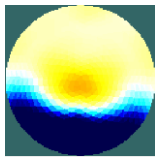

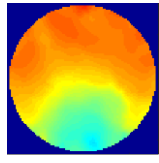
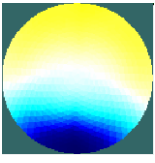
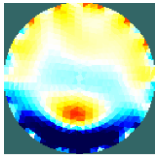

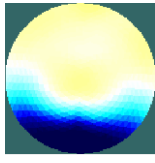

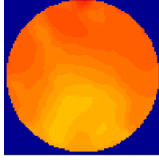

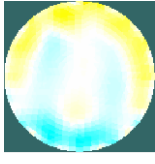


Configurations		One-step	Laplace Prior	AHPS	Total Variation	Conjugate Gradient
A Flow rate: 0.68l/s Height: 1.7 cm						
B Flow rate: 1.3l/s Height: 2.2cm						
C Flow rate: 2.82l/s Height: 1.9cm						
D Flow rate: 4.5l/s Height: 0cm						

Figure 4.19 Summary of image reconstruction comparison for flow loop experiments A-D

The accuracy of each algorithm (based on the bed level height) obtained from all four flow loop experiments is shown in Table 4.21. The calculation of the average of the percentage error clearly indicates that the Laplace Prior yielded better results with an average accuracy of 26.2%, followed by the One-step algorithm with a value of 31.2%, the Total Variation with a value of 35.3%, the Conjugate Gradient with 36.5% and finally the AHPS algorithm with 51.5%.

Table 4.21 Average accuracy for each algorithm for the flow loop experiments

Flow rates	PE (OS)	PE (LP)	PE (AHPS)	PE (TV)	PE (CG)
A	11.8	4.1	29.4	17.7	5.9
B	36.4	29.6	50.0	45.5	36.4
C	15.8	34.2	52.6	33.7	34.2
Average	21.3	22.6	44.0	32.3	25.5

The computational time of all three experiments is shown in Table 4.22. Although the reconstruction time of all four algorithms increased significantly compared to the computational time of the shape test and level bed experiment, the results clearly indicated that the Conjugate Gradient was still the fastest algorithm with an average value of 13.41s, then the Laplace Prior with 14.14s, the Total variation with 19.22s and the AHPS algorithm with 77.94s.

Table 4.22 Average computational time (in second) of each algorithm for the flow loop experiments

Configurations	CT(OS)	CT(LP)	CT (AHPS)	CT (TV)	CT (CG)
A (0.86 l/s)	29.53	13.72	70.13	18.81	12.98
B (1.3 l/s)	28.29	13.54	78.69	18.51	12.86
C (2.82 l/s)	28.67	13.70	79.57	18.77	13.03
D (4.5 l/s)	28.16	15.58	83.35	20.77	14.78
Average	28.66	14.14	77.94	19.22	13.41

The image quality scores of each algorithm are shown in Table 4.23. The average score obtained show that the AHPS algorithm produced poor image quality (with a score of 0.6 out of 3). On the other hand, the Total Variation algorithm had the highest score of 2.4 (out of 3) followed by the Laplace Prior algorithm (with a score of 2.3 out of 3), the UCT and Conjugate Gradient algorithms with a score of 1.9 (out of 3) each.

Table 4.23 Average of the image quality scores of each algorithm for the flow loop experiments

Configurations	IQ (OS)	IQ (LP)	IQ (AHPS)	IQ (TV)	IQ (CG)
A (0.86 l/s)	2.5	2.5	1.5	2.5	2.5
B (1.3 l/s)	2.5	2.5	1	2.5	2.5
C (2.82 l/s)	2.5	2.5	1	2.5	2.5
D (4.5 l/s)	3	2.5	2.5	3	2.5
Average	2.6	2.5	1.5	2.6	2.5

When considering the accuracy, the computational time and the image quality scores for this experiment, the Laplace Prior appears to be the best algorithm.

4.4 Final Summary

The performance of five reconstruction algorithms was tested in three different situations. Firstly, reconstructed images were obtained when various objects with different shape were placed inside the ERT pipe test section. Secondly, the algorithm performances were put to test in a level bed setup experiment and finally, the algorithms were applied to a real flow situation, where different flow rates were applied.

Tables 4.24, 4.25 and 4.26 present the summary of the results of the percentage errors, the computation time and the image quality of all the experiments.

Table 4.24 Average values of the percentage difference error (PE) of each experiment

Average values (%)	PE (OS)	PE (LP)	PE (AHPS)	PE (TV)	PE (CG)
Shape Tests	10.8	21.5	46.7	16.5	23.1
Level bed	8.3	11.3	20.5	10.5	14.3
Flow loop	21.3	22.6	40.0	32.3	25.5
Average	13.5	18.5	35.7	19.8	21.0

Table 4.25 Average values of the computational time (CT) for each experiment

Average values (s)	CT (OS)	CT(LP)	CT (AHPS)	CT (TV)	CT (CG)
Shape Test	18.39	3.63	66.55	8.73	2.93
Level bed	18.72	3.95	65.89	8.71	3.01
Flow loop	28.66	14.14	77.94	19.22	13.41
Average	21.92	7.24	70.13	12.22	6.45

The computational times of all experiments shown in Table 4.25 clearly indicates a significant increase of the reconstruction time when moving from static tests to dynamic tests.

Table 4.26 Average values of the image quality (IQ) for each experiment

Average values	IQ (OS)	IQ (LP)	IQ (AHPS)	IQ (TV)	IQ (CG)
Shape Test	2.75	2.3	2.2	2.6	2.4
Level bed	2.8	3.0	1.7	3.0	2.8
Flow loop	2.6	2.5	1.5	2.6	2.5
Average	2.7	2.6	1.8	2.7	2.6

The results obtained clearly show that, although the One-step algorithm was not the fastest algorithm, it was the best algorithm to produce the best results in terms of accuracy. Among the EIDOR based algorithm, the Laplace Prior was clearly the best algorithm in terms of accuracy (low percentage difference error), follow by the Total Variation. Although the Total Variation algorithm did not produce the lowest percentage difference error, it had the best quality images as well as sharper reconstructed images that were representative of the actual configuration and flow condition.

The Conjugate Gradient also yielded better reconstructed images with respect to the shape and the size of the area of low conductivity. It was also the fastest among the selected algorithms.

The AHPS algorithm was the least performing algorithm in term of accuracy and the quality of the reconstructed images. Also, it was the slowest computational times of all five algorithms.

Although the One-step algorithm was the best performer with regards to the accuracy, it did not produce sharper reconstructed images.

Based on the results shown in Tables 4.24, 4.25 and 4.26, the overall best algorithm, based on the percentage error, computational time and the image quality was the Total Variation.

Chapter 5 SUMMARY, CONCLUSIONS, CONTRIBUTIONS, LIMITATIONS AND RECOMMENDATIONS

5.1 Summary

Sarode et al. (2013) conducted a comparative study of the image reconstruction of a circular plastic phantom using different 2-D algorithms such as Back Projection, Total Variation and Gauss-Newton (with Priors such as Noser, Laplace and Tikhonov) were compared based on the size and shape of the impurity.

The effect of measurement strategies (adjacent and opposite technique) were investigated by Stephenson et al. (2008). The implication of the choice of measurement techniques on the image-derived process metrics was also investigated. The results obtained were compared in term of image accuracy using different 2D reconstruction algorithms.

The description of quantitative image reconstruction techniques for an ERT system evaluated using synthetic and experimental test cases was investigated by Giguère et al. (2008b). The reconstructed images were compared using the GIA and LBP algorithms. The study was only limited to the comparison of reconstructed images of solid particle data with synthetic data.

Although 2D reconstruction algorithms have been extensively applied in various processes, there has been very little research done on the comparison of 2D or 3D reconstruction algorithms in the identification of fluid bed or objects. A comprehensive analysis of image reconstruction algorithms is needed where important parameters such as algorithm computational time, quality of image and accuracy of reconstructed images of objects or the characterisation and evaluation of real multiphase flow regimes are involved.

Therefore, the main objective of this research was to focus on the comparison of different 2-D algorithms with the aim of finding the accuracy of their computation as well as the quality of the reconstructed images and the computational time of each algorithm.

An ERT system developed by UCT was used in order to collect measurement data. Reconstructed images, using the measurement data, were determined using five reconstruction algorithms. Four of the algorithms (namely: the Laplace Prior, the Automatic Hyperparameter Selection (AHPS), the Total Variation and the Conjugate Gradient) were based on EIDORS 2D with MATLAB functions open source free library. The fifth algorithm, referred to as the One-step algorithm, was developed by Long (2005) and operated with MATLAB functions.

In order to achieve these comparisons, three different experimental setups were put in place namely: the shape test, the level bed and the flow loop experiments.

Two electrode rings spaced at a fixed distance apart were fitted on a pipe test section. Since the selected algorithms are 2D algorithms, only one electrode ring was used to record the data while the second electrode ring was used to provide a ground level to the measuring electrode.

Three experimental tests were conducted in a 4.26 cm diameter pipe test using saline water, different shape of objects and beads with a particle size of 3 mm. the first experiment consisted of collecting measurement data while various objects with different size were placed inside the pipe test section. The second experimental test consisted of recording data, when different level beds were formed inside the pipe test section using beads and water. This was a static test where no flow was present, ie the beads and water was stationary. Finally, the last experimental test was done in a flow loop pipe, where data was captured at four different flow rate (with beads and water). During these tests different flow regimes were tested.

The measured data from all experimental setups were then used to reconstruct the image of the low conductivity area within the conductive saline solution. The reconstructed images, obtained using five reconstruction algorithms, were then compared with each other based on the three specific criteria, namely: the accuracy of the reconstructed images, the quality of the images and the computational time of each algorithm.

5.2 Conclusion

The following final conclusions can be drawn:

- The best reconstructed images were obtained by using a heuristic approach for selecting the appropriate hyperparameter for each experiment. The level bed and flow loop experiments mostly used a hyperparameter value of 1, while the shape test experiments required various hyperparameter values ranging from 0.0001 to 1.
- Of all five algorithms, the Total Variation algorithm produced better reconstructed images with respect to more defined shape of objects and sharper reconstructed images. Furthermore, it reproduced the most realistic flow conditions of the flow loop experiments in terms of image quality. Although the Total Variation algorithm was not the fastest algorithm, it reproduced accurate reconstructed images with an average percentage difference error of 19.8%. The average quality score and computational time obtained were 2.7 and 12.22s respectively.
- With respect to the shape and the size of the area of low conductivity, the Laplace Prior algorithm was the best EIDORS based algorithm with an average percentage error of 18.5%. The Conjugate Gradient algorithm also yielded good reconstructed images with an average percentage error of 21.0%. Both algorithms produced an average quality score of 2.6 each. Those two algorithms were the fastest with an average computational time of 6.45s and 7.24s, respectively.
- In terms of accuracy and the quality of the reconstructed images, the AHPS algorithm was the least performing algorithm with an average percentage error of 35.7% and an average image quality score of 1.8 out of 3. Also, it was one of the slowest computational times of all five algorithms, with an average value of 70.13s.
- Although the One-step algorithm was the overall best performer in terms of accuracy (with an average value of 13.5%), it was not the fastest reconstruction algorithm. The

One-step algorithm yielded a good reconstructed image with respect to the shape of the objects and the size of the level bed. The average value of the image quality score obtained was 2.7 out of 3. In term of computational time, the One-step algorithm came in third position with an average value of 21.92s.

In conclusion, all five selected algorithms were able to determine the location of low conductivity (where the objects and the level bed were placed) for all three experiments. However, the AHPS algorithm, which was the slowest algorithm, was not a good fit for the level bed and flow loop experiments, as the reconstructed images did not agree with the actual measurement conditions. Although the Conjugate Gradient algorithm was not the best algorithm, it was the fastest algorithm among the five selected algorithms. It was proven that all five algorithms are able to successfully reproduce images that are representative of different flow conditions. The One-step and the Total Variation algorithms in the other hand were the best algorithms for the shape test experiments. In application where interface detection are critical, these two algorithms could be prove useful. For industrial applications, where the characterisation of fluid flow inside the pipes is of most importance, it can be concluded that of all five selected algorithms, the Laplace Prior, the Total Variation, the Conjugate Gradient algorithms as well as the One-step algorithm could be very usefully in the early detection of pipe blockages.

5.3 Contributions

Although the selected reconstructed algorithms have already been developed by previous authors, the following contributions were made:

- Five reconstruction algorithms were tested and evaluated in three different experimental setups. It was found that the performances of the different algorithms are not similar and that some algorithms are more suitable for specific ERT applications.

- Software (GUI) was developed for post data analysis. This software enables other users to easily perform a comparative study of four reconstruction algorithms in EIDORS using measurement data.
- A database of measurement data captured in a wide range of different experiments was compiled. This can now be used to test other EIDORS algorithms and to experiment with different parameters such as mesh sizes and types, number of iterations as well as additional evaluation of the hyperparameter value.

5.4 Limitations

The main limitations found in this work are as follow:

- The hyperparameter value had a great influence on the results of all reconstruction algorithms. The fact that it was not possible to set it automatically was an overall limitation. The exception in this case was the AHPS algorithm which had the ability of setting the hyperparameter value automatically although it did not produce good results. When industrial applications are considered this parameter must be automated.
- Due to the restriction of the memory and processing power of the PC, the number of elements used to reconstruct images was restricted to 1024.
- The limitation of the 2D reconstruction over the 3D is the fact the 2D reconstructs the image located in the plane of the electrodes; therefore the resolution and the magnitude of the reconstructed image decrease while the radial error increases.
- The main limitation during this research was the size of the pipe test. Given the fact that a pipe test section of 4.26 cm in diameter was used for the experiments, there were restrictions on the size of objects used for the experiments.

5.5 Recommendations

The following aspects should be explored for future research:

- Given the fact that, in order to produce reconstructed images with good resolution, the hyperparameter value for each reconstruction had to be selected based on a heuristic approach, the design of new codes with the ability to automatically select the optimum value for hyperparameter will prove useful, especially for industrial applications.
- During this research, reconstructed images were obtained using measured data as well as calibration data (which were taken when the pipe test was filled with water only, with no objects or particles inside). Investigation of 'static' reconstruction methods using measurement data only could be very useful for industrial applications where initial calibration is often not possible.
- In order to further investigate industrial applicability, more tests are needed in real fluid suspensions for example sand and oil suspensions
- Although the adjacent strategy is one of the quickest measurement methods, it is very sensitive to error measurement and noise due to non-uniform distribution and low current density at the centre of the vessel. The effect of noise could be addressed by incorporating a system (such as filters) that is able to significantly reduce the noise level associated with the data collection.

REFERENCES

- Adetunji, O.C., 2011. Implementation of an advanced algorithm for enhanced signal analysis in electrical resistance tomography using the EIDORS toolbox. Unpublished M.Eng dissertation, University of Cape Town.
- Adler, A., & Lionheart, W. R. 2006. Uses and abuses of EIDORS: an extensible software base for EIT. *Physiological measurement*, 27(5), S25.
- Adler, A., Dai, T., & Lionheart, W. R. 2007. Temporal image reconstruction in electrical impedance tomography. *Physiological measurement*, 28(7), S1.
- Adler, A. and Guardo, R., 1996. Electrical impedance tomography: regularized imaging and contrast detection. *Medical Imaging, IEEE Transactions on*, 15(2), pp.170-179.
- Alme, K. J., & Mylvaganam, S. 2006. Analyzing 3D and Conductivity Effects in Electrical Tomography Systems Using COMSOL Multiphysics EM Module. In *Proceedings of the Nordic COMSOL Conference*. November 2006.
- Avriel, M., 2003. *Nonlinear programming: analysis and methods*. Courier Corporation pp 287.
- Barber, D. C. 2005. EIT: The view from Sheffield. *Electrical impedance tomography: methods, history and applications*, DS Holder, ed, 348-371.
- Blink, E. J. 2004. mri: Physics. *Online PDF file*.
- Bolton, G. T., Hooper, C. W., Mann, R., & Stitt, E. H. 2004. Flow distribution and velocity measurement in a radial flow fixed bed reactor using electrical resistance tomography. *Chemical engineering science*, 59(10), 1989-1997.
- Borcea, L. 2002. Electrical impedance tomography. *Inverse problems*, 18(6), R99-R136.
- Borges, A. R., De Oliveira, J. E., Velez, J., Tavares, C., Linhares, F., & Peyton, A. J. 1999. Development of electromagnetic tomography (EMT) for industrial applications. Part 2: Image reconstruction and software framework. In *Proc. 1st World Congr. Industrial Process Tomography* (pp. 219-225), April 1999.
- Borsic, A., Graham, B.M., Adler, A. and Lionheart, W.R., 2010. In vivo impedance imaging with total variation regularization. *Medical Imaging, IEEE Transactions on*, 29(1), pp.44-54.

-
- Borsic, A. 2002. *Regularisation methods for imaging from electrical measurements*. Unpublished Doctoral dissertation, Oxford Brookes University.
- Brown, B.H., 2009. Electrical impedance tomography (EIT): a review. *Journal of medical engineering & technology*.
- Cheney, M., Isaacson, D. and Newell, J.C., 1999. Electrical impedance tomography. *SIAM review*, 41(1), pp.85-101.
- Cheng, L. K. 2001. *Non-invasive electrical imaging of the heart*. Unpublished Doctoral dissertation, ResearchSpace, Auckland.
- Chin, R. K. Y. (2011). *3D tomographic imaging using ad hoc and mobile sensors*. Unpublished Doctoral dissertation, University of Manchester.
- Cooper, K. L., Harnan, S., Meng, Y., Ward, S. E., Fitzgerald, P., Papaioannou, D. & Lorenz, E. 2011. Positron emission tomography (PET) for assessment of axillary lymph node status in early breast cancer: a systematic review and meta-analysis. *European Journal of Surgical Oncology (EJSO)*, 37(3), 187-198.
- Crowe, C.T. 2006. *Multiphase flow handbook*. Taylor & Francis Group (FL): CRC Press.
- Dickin, F., & Wang, M. 1996. Electrical resistance tomography for process applications. *Measurement Science and Technology*, 7(3), 247.
- Dong, F., Xu, Y., Hua, L., Wang, H., 2006. Two methods for measurement of gas-liquid flows in vertical upward pipe using dual-plane ERT system. *IEEE Transactions on Instrumentation and Measurement* 55 (5), 1576–1586.
- Dyakowski, T., Jeanmeure, L. F., & Jaworski, A. J. 2000. Applications of electrical tomography for gas–solids and liquid–solids flows—a review. *Powder technology*, 112(3), 174-192.
- Fish, J., & Belytschko, T. 2007. *A First Course in Finite Elements*.
- Hartov, A., Soni, N., & Halter, R. 2005. Breast cancer screening with electrical impedance tomography. *Electrical Impedance Tomography: Methods, History and Applications*, 167-85.
- Holder, D. S. 2008. Electrical impedance tomography of brain function. In *Automation Congress, 2008. WAC 2008. World* (pp. 1-6). IEEE. , September 2008.
- Giguère, R. Fradette, L. Mignon, D. Tangy, P.A., 2008a. Characterization of slurry flow regime transitions by ERT. *Chemical Engineering Research and Design* 86, 989-996.
-

-
- Giguère, R. Fradette, L. Mignon, D. Tangy, P.A., 2008b. ERT algorithms for quantitative concentration measurement of multiphase flows. *Chemical Engineering Research and Design* 141, 305-317.
- Graham, B. M. 2007. Enhancements in Electrical Impedance Tomography (EIT) image reconstruction for three-dimensional lung imaging.
- Graham, B. M., & Adler, A. 2006. Objective selection of hyperparameter for EIT. *Physiological measurement*, 27(5), S65.
- Granot, Y., & Rubinsky, B. 2007. Frequency Marked Electrodes in Electrical Impedance Tomography. In *13th International Conference on Electrical Bioimpedance and the 8th Conference on Electrical Impedance Tomography* (pp. 380-383). Springer Berlin Heidelberg, January 2007.
- Grootveld, C. J., Segal, A., & Scarlett, B. 1998. Regularized modified Newton-Raphson technique applied to electrical impedance tomography. *International journal of imaging systems and technology*, 9(1), 60-65.
- Islam, M.R. and Kiber, M.A., 2014, May. Electrical Impedance Tomography imaging using Gauss-Newton algorithm. In *Informatics, Electronics & Vision (ICIEV), 2014 International Conference on* (pp. 1-4). IEEE.
- Jia, X. Q., Dong, F., Xu, Y. B., Tan, C., & Xue, Y. X. 2005. Structural optimization of dual-plane ERT electrode array. In *Machine Learning and Cybernetics, 2005. Proceedings of 2005 International Conference on* (Vol. 2, pp. 1031-1036). IEEE, August 2005.
- Karhunen, K. Seppänen, A. Lehtikoinen, A. Monteiro, P.J.M. Kaipio, J.P., 2010. Electrical Resistance Tomography imaging of concrete. *Cement and Concrete Research* 40, 137-145.
- Kim, K. Y., Kim, B. S., Kim, M. C., Lee, J. H., Park, J. W., Lee, Y. J., & Choi, Y. B. 2000. Regularized modified Newton Raphson algorithm for electrical impedance tomography based on the exponentially weighted least square criterion. In *TENCON 2000. Proceedings* (Vol. 1, pp. 64-68). IEEE.
- Lionheart, W., Polydorides, N., & Borsic, A. 2005. The reconstruction problem. *Electrical impedance tomography: methods, history and applications*, 750309520, 3-64.
- Mann, R., Dickin, F.J., Wang, M., Dyakowski, T., Williams, R.A., Edwards, R.B., Forrest, A.E., Holden, P.J., 1997. Application of electrical resistance tomography to interrogate mixing processes at plant scale. *Chemical Engineering Science* 52(13), 2087-2097.
-

-
- Oh, S., & Sadleir, R. 2005. Sensitivity distribution field of electrical impedance tomography. In *COMSOL Multiphysics User's Conference, Boston, USA*.
- Pakzad, L., Ein-Mozaffari, F., Chan, P., 2008. Measuring mixing time in the agitation of non-Newtonian fluids through electrical resistance tomography. *Chemical Engineering and Technology* 31 (12), 1838–1845.
- Pinheiro, P.A.T.; Loh, W.W.; Dickin, F.J. 1998. Three-dimensional reconstruction algorithm for electrical resistance tomography. *Science Measurement and Technology, IEE Proceedings - Volume: 145, Issue: 3, 85-93*.
- Polydorides, N., & Lionheart, W. R. 2002. A MATLAB toolkit for three-dimensional electrical impedance tomography: a contribution to the Electrical Impedance and Diffuse Optical Reconstruction Software project. *Measurement Science and Technology, 13(12), 1871*.
- Qi, G.H., Dong, F., Xu, V.B., Wu, M.M., Hu, J., 2005. Gas/liquid two-phase flow regime identification in horizontal pipe using support vector machines, Guangzhou.
- Queiroz, J. L. L. 2012. Influence of regularization in image reconstruction in electrical impedance tomography. In *Journal of Physics: Conference Series* (Vol. 407, No. 1, p. 012006). IOP Publishing, December 2012.
- Randall, E. W., Wilkinson, A. J., Long, T. M., & Collins, A. 2005. The design of a flexible multi-layer ERT system and an evaluation of its performance. In *4th World Congress on Industrial Process Tomography, Aizu, Japan*.
- Scott, D.M., McCann, H., 2005. *Process Imaging for Automatic Control*. CRC Press Taylor and Francis Group.
- Sharifi, M., & Young, B. 2013. Electrical resistance tomography (ERT) applications to chemical engineering. *Chemical Engineering Research and Design, 91(9), 1625-1645*.
- Somersalo, E., Cheney, M., & Isaacson, D. 1992. Existence and uniqueness for electrode models for electric current computed tomography. *SIAM Journal on Applied Mathematics, 52(4), 1023-1040*.
- Soulsby, C., Yazaki, E., & Evans, D. F. 2004. Applications of electrical impedance tomography in the gastrointestinal Tract. *Electrical Impedance Tomography: Methods, History and Applications*, 186.
- Stanley, S. J., & Bolton, G. T. 2008. A review of recent electrical resistance tomography (ERT) applications for wet particulate processing. *Particle & Particle Systems Characterization, 25(3), 207-215*.
-

-
- Stephenson, D.R. Mann, R. York, T.A., 2008. The sensitivity of reconstructed images and process engineering metrics to key choices in practical electrical impedance tomography. *Measurement Science and Technology* 19, 094013.
- Sutherland, A. P. N., Slatter, P. T., Wilkinson, A. J., Randall, E. W., & Long, T. 2005. A pipe test facility to examine laminar shear settling using electrical resistance tomography (ERT). In *4th World Congress on Industrial Process Tomography, Virtual Centre for Industrial and Process Tomography (VCIPT), Glossop, UK* (pp. 267-272), September 2005.
- Tamburrino, A., & Rubinacci, G. 2002. A new non-iterative inversion method for electrical resistance tomography. *Inverse Problems*, 18(6), 1809.
- Tapp, H. S., Peyton, A. J., Kemsley, E. K., & Wilson, R. H. 2003. Chemical engineering applications of electrical process tomography. *Sensors and Actuators B: Chemical*, 92(1), 17-24.
- Vauhkonen, P. J., Vauhkonen, M., Savolainen, T., & Kaipio, J. P. 1999. Three-dimensional electrical impedance tomography based on the complete electrode model. *Biomedical Engineering, IEEE Transactions on*, 46(9), 1150-1160.
- Wajman, R., Banasiak, R., Mazurkiewicz, L., Dyakowski, T. and Sankowski, D., 2006. Spatial imaging with 3D capacitance measurements. *Measurement Science and Technology*, 17(8), p.2113.
- Wang, H., Tang, L., & Cao, Z. 2007. An image reconstruction algorithm based on total variation with adaptive mesh refinement for ECT. *Flow Measurement and Instrumentation*, 18(5), 262-267.
- Wang, M., Dickin, F. J., & Mann, R. 1999. Electrical resistance tomographic sensing systems for industrial applications. *Chemical Engineering Communications*, 175(1), 49-70.
- Wang, M., Dorward, A., Vlaev, D., & Mann, R. 2000. Measurements of gas-liquid mixing in a stirred vessel using electrical resistance tomography (ERT). *Chemical Engineering Journal*, 77(1), 93-98.
- Wells, R. G., de Kemp, R. A., & Beanlands, R. S. B. 2009. Positron emission tomography instrumentation. *Nuclear cardiology: Technical applications*. New York: McGraw-Hill Companies. Inc, 27.
- Wilkinson, A. J., Randall, E. W., Long, T. M., & Collins, A. 2006. The design of an ERT system for 3D data acquisition and a quantitative evaluation of its performance. *Measurement Science and Technology*, 17(8), 2088-2096.
- Ying, W., Jinchuang, Z., Shi, W., Xinjie, W., 2001. Research of the Image Reconstruction Algorithm for Electrical Resistance Tomography Based on Neural Network. *School of*
-

Information Science and Engineering. April 2001 Northeastern University, Shenyang. Chinese Journal of Scientific Instrument.

York, T. A. 2004. Electrical tomography for industrial applications. *Electrical impedance tomography: methods, history and applications*, 295-347.

Yunus, F. M., Rahim, R. A., Aw, S. R., Ayob, N. N., Jayasuman, M. P., & Jumaah, M. F. 2014. Front-End Circuit in Electrical Resistance Tomography (ERT) for Two-Phase Liquid and Gas Imaging. *Jurnal Teknologi*, 70(3).

Zhang, L. Wang, H. Xu, Y. Wang, D. 2011. A Fast Iterative Shrinkage-Thresholding Algorithm for Electrical Resistance Tomography. *WSEAS Transactions on Circuit and Systems* 11, vol10.

APPENDICES

Appendix A. Calibration Procedure

Running the program for the first time

Before running the program for the first time, ensure:

1. The tomography instrument is switched on.
2. The tomo USB cable is plugged into a USB port on the PC.
3. The USB serial adapter is plugged into the tomography instrument “comms port” and a PC USB port.

Locate and run the executable program file called UCT_Tomography.exe. The user should be faced with a screen similar to that shown in Figure 1.

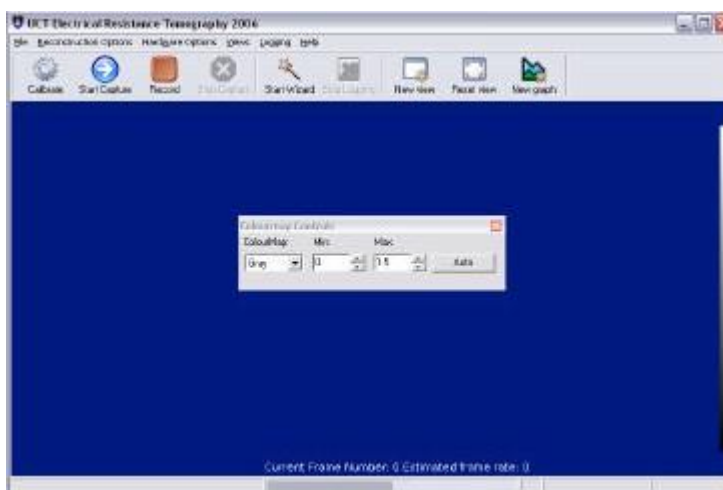


Figure A.1 *The initial start screen*

Follow these steps to generate tomography images.

Step 1: Selecting a mesh and precomputed file

The first step is to choose a mesh and an associated precomputed file to be used for the image reconstruction algorithm. The precomputed file contains the results of an off-line calculation and is used to speed up the reconstruction algorithm. It is important to make sure that the precomputed file corresponds to the mesh that was used to calculate it.

1. Select **Reconstruction Options >> Change Mesh**.
2. Choose 'Mesh files\836_elements.mes' when prompted to select a mesh.
3. Choose 'Precomputed files\836_elements_0-001.pcmp' when prompted to select a precomputed file.
4. To display the reconstruction mesh, select **View Options >> Add view** or click

the 'add view' button. To automatically resize the mesh to fit the window, select **View Options >> Reset view** or click the 'reset view' button.

The number at the end of the precomputed filename is the smoothing factor (related to the regularization parameter) used by the reconstruction algorithm. A larger number indicates more smoothing.

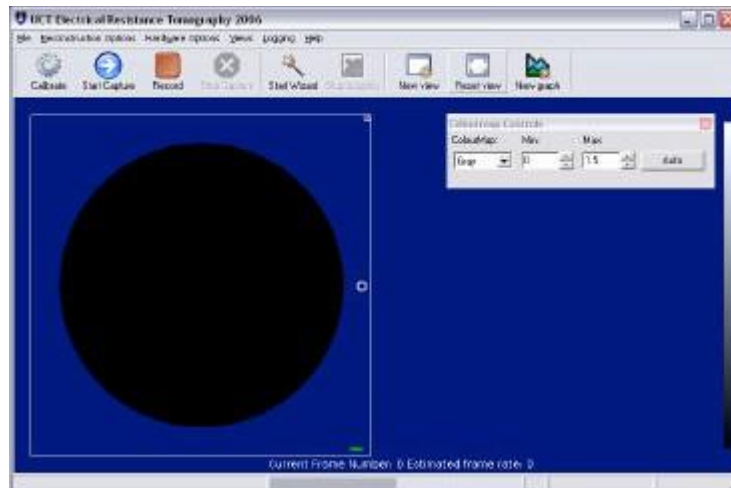


Figure A.2 The mesh and precomputed file loaded correctly

Step 2: Setting up the Measurement Sequence and testing Serial Comms

The next step is to setup the communication between the software and the tomography instrument.

To do this, select **Hardware Options >> Select Hardware** and choose the appropriate instrument connected to the computer. The user will then be prompted to select two files. The first, the download file, is a binary file that runs on the tomography hardware; choose 'Download Files\download_file.bin'. The second is the measurement sequence file; choose 'Sequence Files - independent \seq_table_1L_indep.txt'.

If the instrument is connected properly, a progress bar will appear indicating that these files are being downloaded to the instrument correctly.

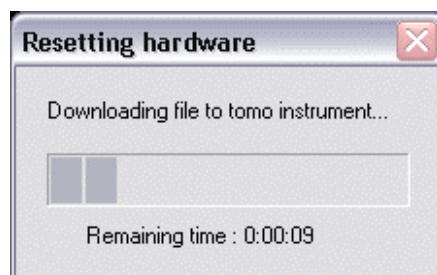


Figure A.3: Downloading measurement sequence

If the download was unsuccessful, it may be that the program is using the wrong comm port and an error message will be shown¹.

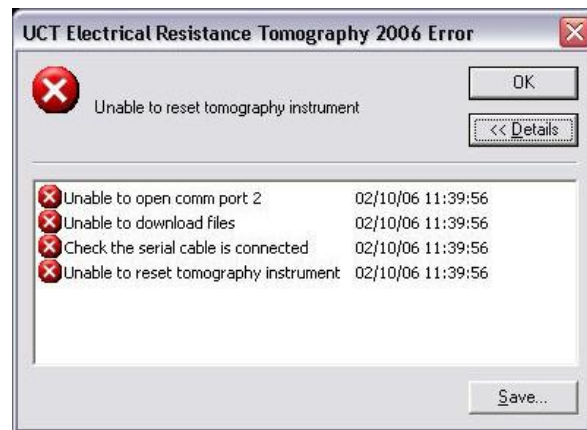


Figure A.4 An expanded error message box

To specify the correct com port, select **Hardware Options >> Change Com Port**, and repeat step 2. If you are unsure which com port the tomography instrument is connected to, see the 'COM & LPT' section of Window's Device Manager. (To start the device manager, right click on the My Computer icon, choose 'Properties,' select the 'Hardware' tab and click the 'Device Manager' button.

To confirm that everything is working properly at this stage, start the instrument in data capture mode. This is done by pressing the Start Capture button; see Figure 5. The 'running with current' LED (the bottom one) should be lit if all is well. Press the 'Stop Capture' button when this has been confirmed.



Figure A.5 The 'Start Capture' button

Step 3: Setting the current level

The instrument needs to supply current of appropriate strength to the tank used and this must be setup manually. When the program is first run, the current level is set at zero. The easiest

way to get it to an appropriate level is to look at the raw voltage measurements in a graph window and adjust the current until the voltages are at the right level while the instrument is running. To do this:

1. Open a graph. Select **View Options >> Add new graph** or click the 'add new graph' button.
2. Start the instrument. Select **Hardware Options >> Start capture** or click the 'Start capture' button. The graph should display a plot similar to Figure 6.
3. Adjust the current. Select **Hardware Options >> Adjust current**. Move the slider to the right to increase the current level.
4. The peaks should be at about 0.9V. The current level switch on the back of the tomography instrument may need to be toggled to get the correct values.

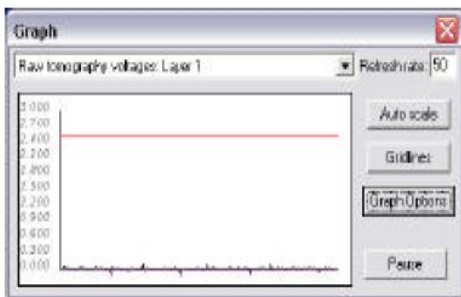


Figure A.6: Data capture with no current applied

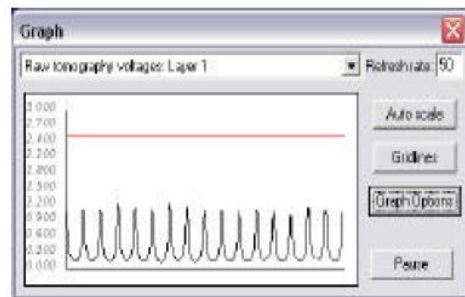


Figure A.7: Data capture with current applied

If the graph doesn't show the regular horseshoe loops in Figure 7, check all electrode connections.

Note that the values shown on the 'adjust current' slider are based on how far along the slider the indicator is. They do not represent the current exactly (although there is an approximately linear relationship between this value and the current level).

Step 4: Calibration

The penultimate step is to run the calibration routine. This is done by selecting **Hardware Options >> Calibrate** or clicking the 'calibrate' button, see Figure 8. This routine captures a dataset which is used to calculate calibration factors. The procedure allows the user to specify both how long the instrument must run for before capturing data used in the calibration calculations, and how many frames of data should be averaged to generate the dataset.



Figure A.8: The 'Calibrate' button

It may be useful to save this calibration set (which will mean it will be loaded automatically the next time the program is run). To save a calibration file, select **File >> Save calibration file**. Before the file is saved, the user will be prompted to supply some information regarding the conditions under which the calibration was done. This information will be included in the calibration file.

Step 5: On-line reconstruction

The final step is to start the instrument. To do this, select **Hardware Options >> Start capture** or click the 'start capture' button. The colour map and its limits can be changed from the drop down menu shown in Figure 9 if desired.

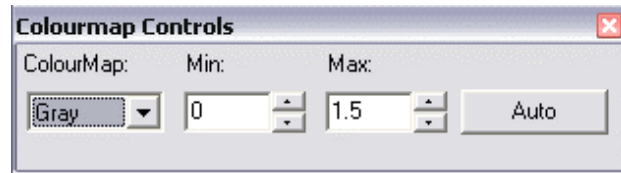


Figure A.9: The colour map drop down menu

The 'Auto' button shown above automatically adjusts the min and max values to 10% beyond the minimum and maximum conductivities of the current frame.

Figure 10 shows the tomography software and hardware running normally. The background colours have been changed for printing purposes.

To save the measured voltages and reconstructed conductivities, see the *Saving data* section of this document.

When the instrument is stopped and the program exited, the above settings will be saved to the registry and reloaded the next time the program is started. This means that, when the program is restarted, there is no need to adjust the current levels or run the calibration routine.

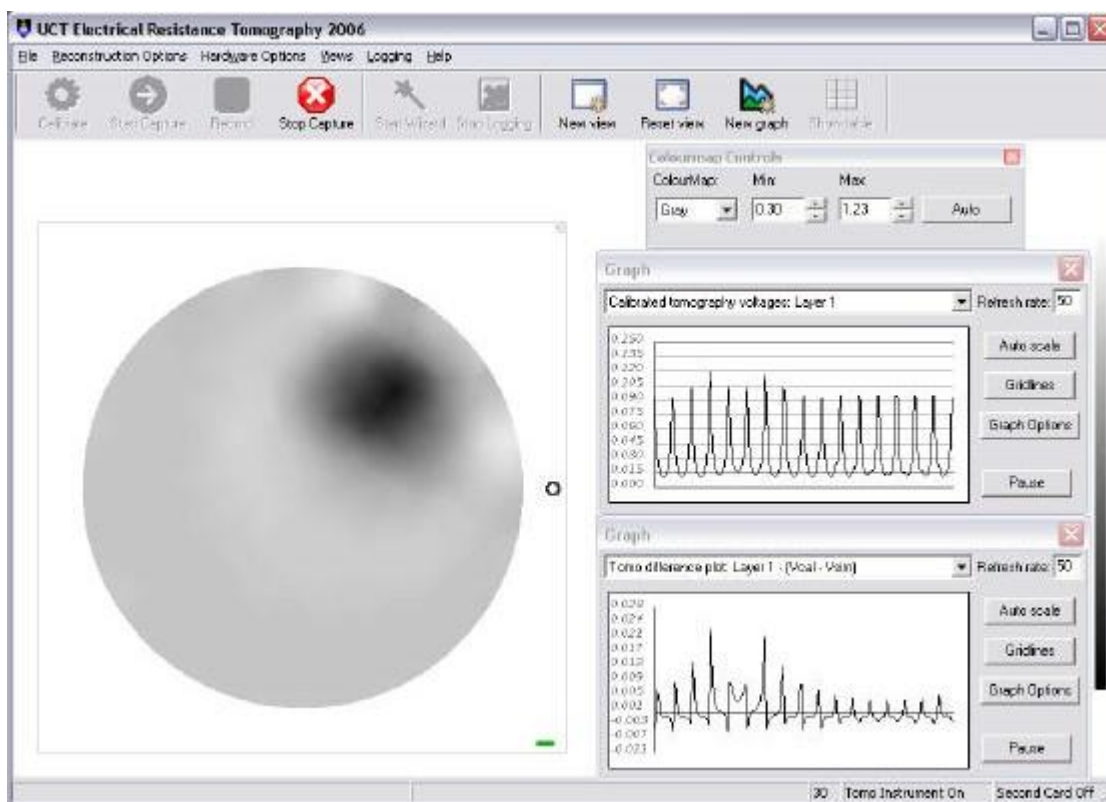


Figure A.10: The tomography program reconstructing conductivity images

Saving data

This section contains information about saving the raw voltage measurements taken by the tomography instrument as well as the reconstructed conductivity values.

There are two ways to save the voltage measurements:

1. Doing a quick record.
2. Using the data logging wizard.

Saving voltage data via quick record

Simply pressing the record button will start saving voltage measurements to disk. When the run is stopped, the user will be prompted to specify a file to save this data as.



Figure A.11: *The record button*

Saving voltage data via wizard

The wizard creates a data logging project. Starting a project creates a directory in which the files associated with the project are saved. These files are:

- A project log file.
- A tomography calibration file.
- A data file for each data capture run.

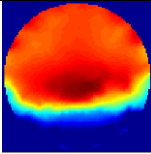
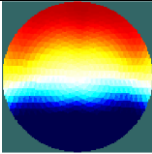
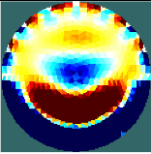

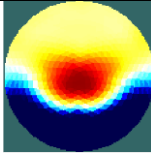
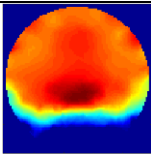
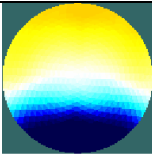


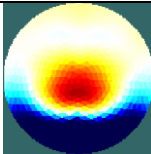
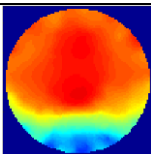



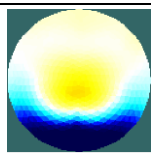


Figure A.12: *The 'Start Wizard' button*

The logging wizard consists of a two pages which help the user set up a data capture project. These are:

- The project details page
- The tomography details page

Appendix B. Summary of results obtained from the second dynamic flow loop experiments.

Configurations	One-step algorithm	Laplace Prior	AHPS	Total Variation	Conjugate Gradient
A Flow rate: 0.67l/s					
B Flow rate: 1.68l/s					
C Flow rate: 2.84l/s					
D Flow rate: 4.76l/s	